A Bayesian approach to analyzing tectonic subsidence applied to the Ediacaran Nafun Group, Oman

William Wong

Department of Earth and Planetary Sciences

McGill University, Montreal

Supervisor: Dr. Galen P. Halverson

April 2022

A thesis submitted to McGill University in partial fulfillment of the requirements of the degree of Master of Science

TABLE OF CONTENTS

Chapter 2:

FIGURES LIST

TABLES LIST

ABSTRACT

The Ediacaran Period (ca. 635-539 Ma) represents one of the most important and dynamic intervals in Earth's evolution. This period saw the rise of complex multicellular life, the amalgamation of the Supercontinent Gondwana, the oxygenation of surface environments, and the Shuram Negative Carbon Isotope Excursion (SE), which represents the largest known perturbation to the carbon cycle discovered thus far. While significant attention has focused on each of these events individually, their association with one another is a controversial topic. In addition, it is still widely debated whether the SE represents a primary marker of changing global conditions, or whether it represents a marker of local geochemical processes.

The Nafun Group in Oman is one of the best studied and most complete Ediacaran sections globally and the type area for the SE. Here, we assemble the latest radiometric age constraints spanning the Ediacaran Period and correlate them into the MIQRAT-1 well, which is widely used as a reference section for the Nafun Group and captures the SE in detail. Using Bayesian statistics, we construct an age-depth model based on the MIQRAT-1 well to constrain the ages of important litho- and chemo-stratigraphic boundaries in the Nafun Group and to account for uncertainties associated with both the ages themselves and their correlated stratigraphic position in the drill core. The resulting age model serves as the basis for a subsidence analysis on the Oman basin, where lithostratigraphic corrections are made to account for compaction and sediment loading effects. The results provide insight on the tectonic history of Oman during the Ediacaran Period.

Based on our modelling results, the SE spanned the interval between 571.45 +2.47/-2.98 Ma and 564.25 +2.84/-3.07 Ma, corresponding to a duration of 7.20 +0.37/-0.09 Myrs. This

duration for the SE is compatible with independent estimates based on astrochronology, both in Oman and in other basins, suggesting that the SE represents a global signal of environmental change. Our results also suggest that subsidence in the Oman basin during the early Ediacaran was predominantly thermal in origin following limited extension in the late Cryogenian, but that flexural subsidence initiated between ca. 606.49 Ma and 584.10 Ma. We interpret the onset of flexural subsidence to record the collision of Oman and the Arabian Shield during the latest stages of the East African Orogeny (EAO). The close temporal proximity between supermountain chain development and other geobiological events in the Ediacaran may thus highlight the EAO as a major factor in shaping the Earth's surface environment during this important period.

Résumé

L’Édiacarien (environ 635-539 Ma) représente l'un des intervalles les plus importants et les plus dynamiques de l'évolution de la Terre. Cette période a vu l'essor de la vie multicellulaire complexe, l’assemblage du supercontinent Gondwana, l'oxygénation de la surface terrestre ainsi que l'excursion isotopique négative du carbone de Shuram (SE), qui représente la plus grande perturbation connue du cycle du carbone découverte à ce jour. Bien qu'une attention particulière se soit portée sur chacun de ces événements individuellement, leur association les uns avec les autres est un sujet controversé. En outre, il est encore largement débattu de savoir si le SE représente un marqueur principal de l'évolution des conditions planétaires, ou s'il représente un marqueur de procédés géochimiques locaux.

Le groupe Nafun à Oman est l'une des coupes de l’Édiacarien les mieux étudiées et les plus complètes au monde. Il représente également la zone caractéristique de SE. Ici, nous assemblons les dernières limites d'âge radiométriques couvrant la période de l’Édiacarien et les associons dans le puit MIQRAT-1, largement utilisé comme coupe de référence pour le groupe Nafun et capturant le SE en détail. À l'aide de statistiques bayésiennes, nous construisons un modèle âge-profondeur basé sur le puits MIQRAT-1 pour contraindre les âges limites des importantes limites litho- et chimio-stratigraphiques dans le groupe de Nafun et pour tenir compte des incertitudes associées aux âges eux-mêmes ainsi qu’à leur position stratigraphique corrélée dans la carotte de forage. Le modèle d'âge résultant sert de base pour une analyse de la subsidence du bassin d'Oman, où des corrections litho-stratigraphiques sont apportées pour tenir compte des effets de compactage et de chargement de sédiments. Les résultats donnent un aperçu de l'histoire tectonique d'Oman pendant la période de l’Édiacarien.

Sur la base de nos résultats de modélisation, le SE a couvert l'intervalle entre 571,45 +2,47/-2,98 Ma et 564,25 +2,84/-3,07 Ma, correspondant à une durée de 7,20 +0,37/-0,09 Ma. Cette durée pour le SE est compatible avec des estimations indépendantes basées sur l'astrochronologie, à la fois à Oman et dans d'autres bassins, suggérant que le SE représente un signal global de changement environnemental. Nos résultats suggèrent également que l'affaissement dans le bassin d'Oman au début de l'Édiacarien était principalement d'origine thermique après une extension limitée à la fin du Cryogénien, mais que l'affaissement par flexure lithosphérique a commencé entre approximativement 606,49 Ma et 584,10 Ma. Le début de la subsidence par flexure est interprété comme le commencement de la collision d'Oman et du Bouclier arabe au cours des dernières étapes de l'orogenèse est-africaine (EAO). La proximité temporelle étroite entre le développement de la chaîne de supermontagnes et d'autres événements géobiologiques dans l'Édiacarien peut donc mettre en évidence l'EAO comme un facteur majeur dans la formation de l'environnement de surface de la Terre au cours de cette période importante.

ACKNOWLEDGEMENTS

First and foremost, I would like to thank my supervisor, Dr. Galen P. Halverson, for his guidance, patience, and thoughtful insights towards the completion of this thesis. If not for his guidance and excellent teachings, the completion of this project would have been impossible and I am greatly appreciative for all the help I have received. I also owe a dept of gratitude to fellow members of our research group, Lei Wu, Chen Shen, and Maggie Whelan, whose continued support and useful discussions helped and motivated me to understand Bayesian statistics and programming in R. I would also like to thank my supervisor and NSERC for funding this project, for which I am very grateful.

I would also like to extend my gratitude to friends and family. Their continued support during the past two years were truly critical to keeping me mentally strong during the pandemic and getting me past the finish line with this thesis. For that, I cannot thank them enough and I am more grateful to them then they will ever know.

CONTRIBUTION OF AUTHORS

This thesis was written by William Wong and edited by Dr. Galen P. Halverson. All programming code used for age and subsidence modelling, with the exception of the open-sourced *Modified BChron* R package of Trayler et al. (2019), were written by William Wong. This code was adapted, however, to run in conjunction with the Bayesian updating and subsidence components of this project. Chemostratigraphic correlations were also conducted by William Wong, but with the assistance of Dr. Galen P. Halverson.

CHAPTER 1

1.1 Introduction

The Ediacaran Period (ca. 635-539 Ma) represents one of the most important and dynamic intervals in the geological record, coinciding with the proliferation of morphologically complex animals (McFadden et al., 2008; Xiao and Laflamme, 2009), the onset of large-scale atmospheric and oceanic oxygenation (Campbell and Squire, 2010; Fike et al., 2006; Lyons et al., 2014), an increased frequency in the reversals of the Earth's magnetic field (Meert et al., 2016), and a tectonic reorganization of the continents (Hoffman, 1999). It also hosts a series of carbon isotope anomalies (Corsetti and Kaufman, 2003; Halverson et al., 2005). Among these anomalies is the so-called Shuram Excursion (SE), which is the most negative carbon isotope anomaly discovered in the sedimentary record (Burns and Matter, 1993; Grotzinger et al., 2011). Furthermore, the SE coincides with other major geobiological events, such as the appearance of the Ediacaran biota, which has led to speculation regarding whether a causal relationship exists between these phenomena (Fike et al., 2006; McFadden et al., 2008; Rooney et al., 2020).

While many different mechanisms have been proposed to explain the origin of the SE, it is still highly debated whether this carbon isotope excursion (CIE) represents a primary marker of global change, or whether it is merely a local geochemical overprint resulting from post-depositional processes (Grotzinger et al., 2011; Husson et al., 2015). Indeed, this CIE does feature some uncommon characteristics, such as having a prolonged stratigraphic expression (Grotzinger et al., 2011), decoupled carbon isotopic signatures between marine carbonates and bulk organic matter (Fike et al., 2006; Lee et al., 2013), and a shift in biological source input during the SE interval (Lee et al., 2013). Moreover, testing of potential causative mechanisms has been complicated by poor radiometric age control on the SE, leading to inconsistent age, duration, and biogeochemical implications (Gong and Li., 2020; Le Guerroué et al., 2006b; Witkosky and Wernicke, 2018).

Recent developments in radioisotopic dating methods and improvements to chronostratigraphic techniques have led to progress in calibrating the Ediacaran time scale (Gong and Li, 2020; Rooney et al., 2020). However, many age-depth models developed for this time interval are spread across several paleobasins and are still restricted by limited radiometric ages within individual successions. Moreover, techniques used in classical statistics that interpolate ages between dated horizons are considered overly optimistic given that stratigraphic and temporal uncertainties are not adequately considered (De Vleeschouwer and Parnell, 2014).

This thesis aims to alleviate some of these limitations through the development of a new chronostratigraphic framework for the Ediacaran Period under a Bayesian paradigm. An advantage to using Bayesian statistical modelling to generate age-depth estimates is that both analytical uncertainty and geological information can be directly incorporated into the model itself, resulting in uncertainties that increase away from dated tie points (Parnell et al., 2011) and model ages that consider the law of superposition. This new framework will be applied to the Nafun Group of Oman, which is one of the most complete and thoroughly studied Ediacaran successions globally and the stratotype for the SE. This effort is focused on the stratigraphy of the MIQRAT-1 well of Oman, which represents one of the most complete Nafun Group sections and captures the entirety of the SE in detail (Bowring et al., 2007; Forbes et al., 2010).

This thesis also analyzes the geological history of Oman through the development of a subsidence model. There is currently no consensus regarding the tectonic setting in which the Nafun Group was deposited, with thermal subsidence in a passive margin setting (Allen, 2007;

Le Guerroué et al., 2006b), subsidence caused by oceanic plate subduction on an Andean-type margin (Grotzinger et al., 2002), and subsidence caused by tectonic loading in a foreland basin (Bowring et al., 2007) suggested as possible mechanisms. Indeed, this thesis will conceptualize the final stages for the amalgamation of the supercontinent Gondwana and contribute to a better understanding of the timing of the SE and its potential association with coeval tectonic, climatic, and biological evolution.

1.2 The Ediacaran Period

1.2.1 The Cryogenian-Ediacaran Transition

The formalized GSSP (Global Boundary Stratotype Section and Point) for the lower boundary of the Ediacaran Period is placed at the base of the Nuccaleena Fm in the Flinders Ranges in South Australia (Knoll et al., 2004; 2006). The Nuccaleena Formation is a distinctive, thin dolostone (<1–33 m; Rose and Maloof, 2010) that sharply but conformably overlies Marinoan-aged glacial and pre-glacial strata of the late Cryogenian Elatina Formation. It is similar to other cap dolostones globally that overly Marinoan-aged glacial deposits, which are characterized by their buff to pink microcrystalline texture, commonly feature meter-scale tepee-like structures and horizontal sheet cracks and comprise part of the post-glacial transgressive systems tract deposited during recovery from global glaciation (Hoffman et al., 2007; Xiao and Narbonne, 2020). These cap dolostones also display distinct trends in their carbon isotope values ($\delta^{13}C$), which typically decline up section to values ranging between -2‰ and -3.5‰ at their top (Knoll et al., 2006). Due to their unique character and geochemistry, these post-Marinoan cap dolostones can be readily identified globally, making them excellent stratigraphic markers for the base of the Ediacaran Period (Crockford et al., 2021; Knoll et al., 2006).

While the Nuccaleena Fm has not been dated radiometrically in South Australia, an age of ca. 635 Ma for the Cryogenian-Ediacaran boundary is generally agreed upon based on age constraints obtained from Tasmania (636.41 ± 0.45; Calver et al., 2013), Namibia (635.21 ± 0.59 Ma; Prave et al., 2016), northwestern Canada (632.3 ± 5.9 Ma; Rooney et al., 2015), and southwest China (635.23 ± 0.57 Ma; Condon et al., 2005). Moreover, a recent U-Pb zircon age of 634.57 ± 0.88 Ma obtained from the uppermost Marinoan Nantuo Fm in southwest China (Zhou et al., 2019) brackets the age of the Ediacaran transition to within analytical uncertainty, strengthening the initial age estimate of 635 Ma.

1.2.2 The Ediacaran Biota

The Ediacaran Period marks one of the most biologically significant intervals in Earth history with the first appearance and proliferation of architecturally complex organisms (Narbonne, 2005; Xiao and Laflamme, 2009). These macrofossils, commonly referred to as the Ediacaran biota, represent soft-bodied organisms that flourished on Earth just prior to the Cambrian explosion. Importantly, they may have included early stem and crown group animals with radial symmetry (e.g., Cnidaria), as well as stem group bilaterian animals (Narbonne, 2005). Their impressions are generally preserved as casts and molds under event beds in both shallow and deep-water siliciclastics (Narbonne et al., 2014), but have also been preserved, albeit rarely, in certain carbonate facies (Bykova et al., 2017; Chen et al., 2014). Except for Antarctica, the Ediacaran biota have been discovered on all the modern continents (Laflamme et al., 2013). Yet despite their large global distribution, they are temporally restricted to the latter half of the Ediacaran Period, in assemblages that post-date the Gaskiers Glaciation ca. 579 Ma (Pu et al., 2016; Xiao and Narbonne, 2020). The driving mechanisms behind their appearance at this time, in particular their link to oxygenation of the oceans, remains widely debated.

The Ediacaran biota are generally split into three successive groups (*Figure 1.1*): the Avalon (~571-560 Ma), White Sea (~560-550 Ma), and Nama assemblages (~550-538 Ma; Waggoner, 2003). These successive assemblages highlight evolutionary shifts to the biosphere during the Ediacaran, with each assemblage exhibiting major innovations to biological traits and ecological niches (Droser et al., 2017). For example, the Avalon assemblage primarily consists of fractal branching rangeomorphs with large surface area to volume ratios, a morphology that is preferential for sessile and osmotrophic ecologies (Hoyal Cuthill and Conway Morris, 2014). In contrast, both the White Sea and Nama assemblages feature a larger variety of taxa, a greater diversity of body plans, and morphological innovations that suggest significantly enhanced motility (Droser et al., 2017; Grazhdankin, 2014).

The determination of where the Ediacaran biota fit in the tree of life is still contentious, however. A traditional view was that at least some of these organisms acted as an evolutionary precursor to Cambrian organisms. For example, superficial similarities have been described between the Ediacaran assemblage *Parvancarina* and the mid-Cambrian arthropod *Skania* (Glaessner, 1980; Lin et al., 2006), and the Ediacaran fossil *Arkarua adami* has been described as “closely related” to echinoderm fossils expressed in Cambrian assemblages (Gehling, 1991). In contrast, it has also been suggested that some members of the Ediacaran biota may not have shared any affinity to Phanerozoic animals (Dececchi et al., 2018). It has even been argued that these organisms may have belonged to an extinct subkingdom, phylogenetically distinct from all Cambrian animals, which Seilacher (1992) referred to as the Vendobionta. Nevertheless, some Ediacaran fossils do preserve evidence of mobility and feeding patterns reminiscent of

Phanerozoic biota (Gehling et al., 2014; Ivantsov, 2013), suggesting that at least some members of the Ediacaran biota represent at least stem group bilaterians. This view is supported by lipid biomarker data that link the production of cholesterol to the bilaterally symmetric and segmented fossil *Dickinsonia*, indicating at least some Ediacaran biota represent early macroscopic animals (Bobrovskiy et al., 2018). Some of these early animals may have even exhibited complex behaviours, given that trace fossils consisting of under-mat burrows, surface trails, and vertical traces have been reported. These properties are characteristic of a moderately evolved behavioural ecology with regards to environmental exploitation and biogeochemical cycling, highlighting that bilaterian animals were most likely present by the late Ediacaran (Chen et al., 2013).

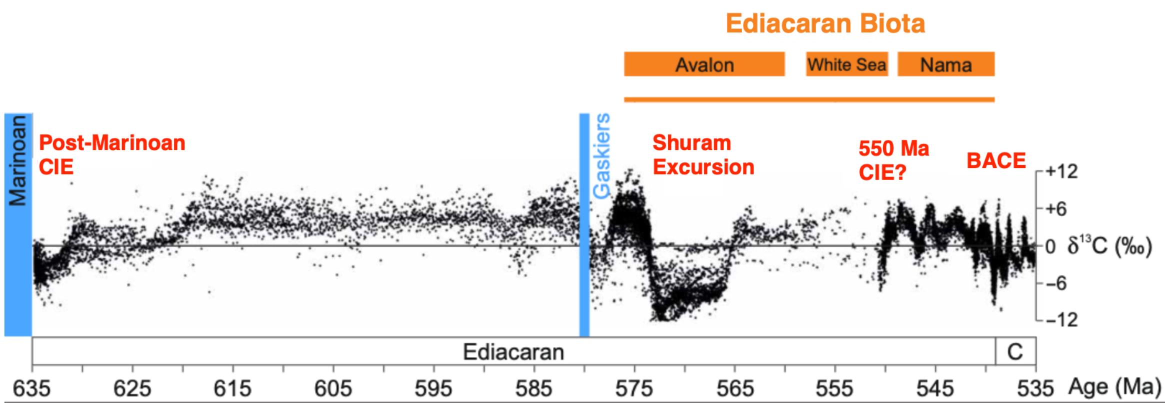

Figure 1.1 | The Ediacaran Carbon Cycle: The $\delta^{13}C_{carb}$ profile of the Ediacaran Period and its potential association with other geobiological events. Carbon isotope excursions (CIEs) are listed in red, glaciations in blue, and Ediacaran biota fossil assemblages in orange. *Modified from Yang et al. (2021)*

1.2.3 The Gaskiers Glaciation

One of the most prominent features during the Neoproterozoic era is the occurrence of extreme and widespread glaciations that may have extended as far as the low latitudes. The global distribution of these glacial deposits, in conjunction with the unique geochemistry of cap carbonates that bracket these glacial deposits, led to the development of the "Snowball Earth" hypothesis (Hoffman et al., 1998; Kirschvink, 1992) for a pair of long-lived, Cryogenian-aged glaciations (Sturtian and Marinoan), which likely represent the most severe icehouse episodes in Earth history. Both glaciations are believed to be globally synchronous, with the Sturtian glaciation lasting from ca. 717-660 Ma (Rooney et al., 2015), and the Marinoan glaciation initiating at least by ca. 639 Ma and terminating at ca. 635 Ma (Prave et al., 2016; Rooney et al., 2015).

While not widespread like their Cryogenian counterparts, glacial deposits of middle Ediacaran age are known from numerous stratigraphic successions globally. The most thoroughly studied of these Ediacaran glacial deposits are from the Gaskiers Fm. on the Avalon Peninsula of southeastern Newfoundland, Canada. The Gaskiers Formation is a ~300 m-thick succession of resedimented glaciomarine rocks (Eyles and Eyles, 1989, Myrow and Kaufman, 1999). U-Pb zircon ages obtained from tuffs that bracket this formation constrain the Gaskiers glaciation to between ca. 580.90 ± 0.40 Ma and 579.88 ± 0.44 Ma (Pu et al., 2016). Similar glaciomarine diamictites have also been identified from the Rocky Harbour Fm on the Bonavista Peninsula in northeastern Newfoundland (Normore, 2011), where U-Pb zircon ages constrain the glacial deposition to between ca. 579.63 ± 0.15 Ma and 579.24 ± 0.17 Ma (Pu et al., 2016). At present, Ediacaran-aged glacial deposits have been identified on 8 paleocontinents, but a lack of age constraints have prevented a direct correlation with the Gaskiers glaciation (Hoffman and Li., 2009). However, given the short duration estimated from Newfoundland (≤340 kyrs; Pu et al., 2016), the Gaskiers glaciation was far less severe than its Cryogenian counterparts and could not have been a snowball glaciation. Pu et al. (2016) suggested that the Gaskiers glaciation may not have acted as a critical barrier to animal evolution given the earliest Ediacaran biota appear in overlying strata in Newfoundland dated at ca. 574.17 ± 0.66 Ma (Matthews et al., 2021).

1.2.4 The Ediacaran Carbon Cycle

One of the fundamental predictions of the Snowball Earth hypothesis is that global icehouse conditions would have restricted surface erosion and runoff, allowing for the build-up of a vast reservoir of atmospheric CO_2. Once carbon dioxide levels reached the critical level to initiate melting in the tropics, the supergreenhouse would have driven rapid deglaciation and extreme continental weathering, culminating in the precipitation of the geochemically distinct cap-carbonates (Hoffman et al., 1998). Variations in the magnitude of this CIE are reported (Hoffman et al., 2007; Lang et al., 2016; Sato et al., 2016). However, this variability can be attributed to a combination of facies-related regional differences and the fact that cap dolostones were deposited diachronously during the post-glacial rise in sea level, such that any given cap dolostone only represents a fraction of the transgression (Hoffman et al., 2007; Yang et al., 2017). Less common values that lie far outside the typical range likely represent either diagenetic alteration or local addition of other ^{13}C-depleted carbon sources, such as methane (Xiao and Narbonne, 2020). Isotope values eventually recover in overlying strata, eventually increasing to positive values ranging between +5‰ and +10‰ (Cui et al., 2018; Halverson et al., 2005; McFadden et al., 2008).

The mid-Ediacaran is punctuated by extremely negative $\delta^{13}C_{carb}$ values dropping to as low as -12‰ (Fike et al., 2006). This CIE is generally referred to as the Shuram Excursion, taking its name from the Shuram Fm. in Oman where it was first documented (Burns and Matter, 1993). Similar negative $\delta^{13}C_{carb}$ values have been reported from sedimentary sections from Namibia (Halverson et al., 2005), Australia (Calver, 2000; Husson et al., 2015), Norway (Melezhik et al., 2005), Atlantic Canada (Myrow and Kaufman, 1999), northwestern Canada

(Macdonald et al., 2013), western Brazil (Boggiani et al., 2010), southwestern China (Condon et al., 2005; Xiao et al., 2004; Wang et al., 2021), southeastern Siberia (Melezhik et al., 2009), and the United States (Corsetti and Kaufman, 2003; Kaufman et al., 2007; Witkosky and Wernicke, 2018), but scarce absolute age controls in most of these successions has impeded a full understanding of the origin and stratigraphic extent of the SE, as will be discussed in greater detail in the following section.

A view that has recently been gaining support is that a second pronounced $\delta^{13}C$ anomaly occurs towards the latter half of the Ediacaran Period at ca. 550 Ma (Yang et al. 2021). This CIE has been most widely studied in South China and has generally been interpreted as representing the termination of the SE (An et al., 2015; Zhou et al., 2017). However, given that both Brazil and Namibia feature CIEs that are constrained to that time interval, occur above where the SE should be, and occur below the Ediacaran-Cambrian transition, Yang et al. (2021) argue that two globally synchronous mid-Ediacaran CIEs better explains these properties than the classical view of a single prolonged CIE that terminates at ca. 550 Ma.

Finally, the Ediacaran Period terminates with another CIE known as the Basal Cambrian Carbon Isotope Excursion (BACE; Zhu et al., 2006). This excursion features an abrupt shift from positive $\delta^{13}C_{carb}$ values down to values of -6‰ and is associated with an extinction of the Ediacaran biota (Amthor et al., 2003; Zhu et al., 2006). Although attempts have been made to correlate this event with the Ediacaran-Cambrian boundary (Amthor et al., 2003; Bowring et al., 2007; Kaufman and Knoll, 1995), the exact relationship between the two remains uncertain (Xiao and Narbonne, 2020). At present, this transition is defined for the first appearance of the trace fossil *Treptichnus pedum* (Geyer and Landing, 2016), with 541 Ma being the most widely recognized age estimate for the Precambrian-Cambrian boundary (Bowring et al., 2007).

However, based on new ages from the southern Nama basin in Namibia and South Africa, Linnemann et al. (2019) proposed an age of ca. 539 Ma. Importantly, the BACE does not occur in both sections, with only the Ara Group from Oman, where the ash bed from the original age estimate was obtained, marking the decline in $\delta^{13}C_{carb}$

1.3 The Shuram Excursion

1.3.1 Preface

One of the fundamental challenges in the Earth sciences is determining the processes that led to the origin and diversification of complex multicellular organisms. In particular, the fossils of macroscopic soft-bodied organisms appear in the sedimentary record as early as ca. 574 Ma (Matthews et al., 2021), with a progressive rise in atmospheric and oceanic oxygen commonly suggested as a potential driver for biological evolution (Li et al., 2020; Lyons et al., 2014; McFadden et al., 2008). Occurring at approximately the same time interval are extremely depleted $\delta^{13}C_{carb}$ values which have been documented from multiple Ediacaran successions globally. This CIE, known as the Shuram Excursion, has a nadir as low as -12‰ and is currently the most negative carbon isotope anomaly known in Earth history (Grotzinger et al., 2011). The large magnitude and long duration of this excursion appears to correlate across multiple paleobasins from different continents (Gong and Li., 2020; Grotzinger et al., 2011; Halverson et al., 2005; 2010; Minguez and Kodama, 2015; Zhou et al., 2017), suggesting that these isotopic trends may represent a truly globally synchronous event (Rooney et al., 2020; Yang et al., 2021).

Even accepting that it is globally correlative, many controversies over the SE persist. For instance, the origin of the SE is still debated, with some researchers suggesting that it represents a primary perturbation to the global carbon cycle (Fike et al., 2006; Lee et al., 2015; McFadden et al., 2008; Rothman et al., 2003), while others interpret it as a reflection of diagenetic processes, such as authigenic carbonate precipitation (Cui et al., 2017; Jiang et al., 2019; Schrag et al., 2013), meteoric diagenesis (Knauth and Kennedy, 2009), or burial diagenesis (Derry, 2010). It has even been suggested that igneous processes may have contributed to the SE (Liu et al., 2021; Paulsen et al., 2017), although these mechanisms would still require some contribution from surface processes to explain the anomalously large magnitude of the excursion (Xu et al., 2021).

The age and duration of the SE is also a topic of contention. Although radiometric age constraints are improving, and it is now convincingly demonstrated that it post-dates the ca. 579 Ma Gaskiers glaciation (Pu et al., 2016), the exact timing of the SE is still not known, such that alternative approaches to estimate its duration have been employed. One method that has been applied is through geochemical and box modelling, but this has produced inconsistent results ranging from as short as 1 Myrs (Bjerrum and Canfield, 2011) to durations of 30 Myrs (Miyazaki et al., 2018). Subsidence modelling has also been applied, but this technique has also generated a large gap in duration estimates. For example, Witkosky and Wernicke (2018) conducted a thermal subsidence analysis of the Ediacaran Johnnie Formation from southern Nevada and estimated a duration of 4 to 7 Myrs for the SE. In contrast, Le Guerroué et al. (2006b) conducted a similar analysis on the Nafun Group stratigraphy from Oman, obtaining a ca. 50 Myr duration. This result is now inconsistent with available radiometric ages from Oman and elsewhere and merits re-evaluation on the basis that multiple subsidence mechanisms may have been responsible for deposition of the Nafun Group (Bowring et al., 2007). Finally, astrochronologic techniques have been applied to sections in South Australia, Oman, South China, and the southern United States, yielding estimates of durations between 7.7 Myrs to 9.1 Myrs (*Figure*

1.2; Gong and Li, 2020; Gong et al., 2017; Minguez and Kodama, 2017; Minguez et al., 2015). Despite these similar results between different basins, the astrochronological estimates obtained are still incompatible with those produced from other methods. As a result, further chronological constraints are required to confirm whether the SE is globally synchronous and to test further hypotheses on the cause of the SE.

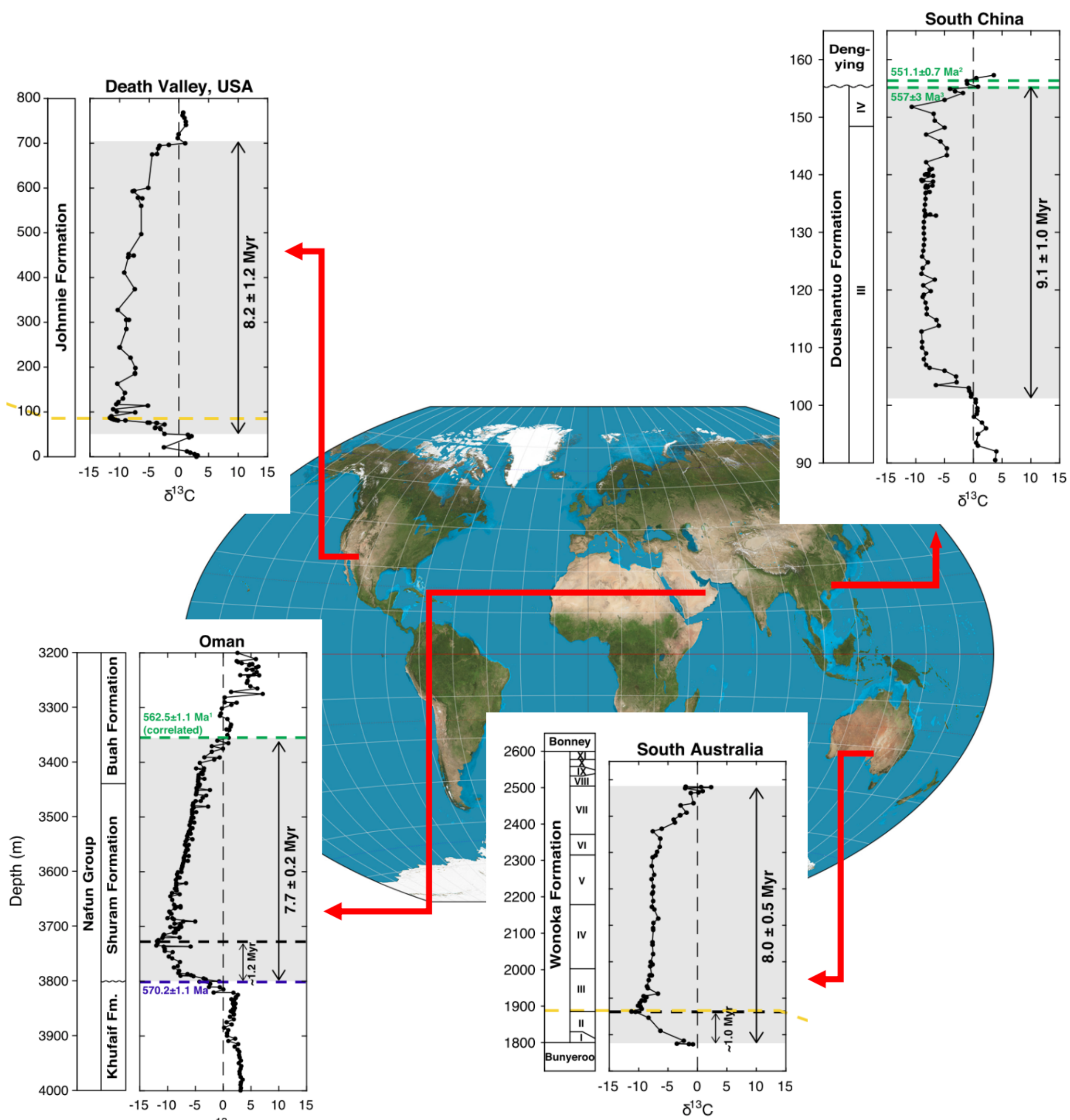

Figure 1.2 | The Global Extent of the Shuram Excursion: Duration estimates for the SE based on astrochronology studies conducted in South Australia, Oman, South China, and the southern United States. *Modified from Gong and Li (2020)*

1.3.2 Primary Signal of Global Change

Many researchers interpret the SE as a primary perturbation to the global carbon cycle. If true, the SE would have had profound effects on the course of Earth's history, in particular its potential link with the rise of animals (Rooney et al., 2020). Assuming the $\delta^{13}C_{carb}$ trend displayed by the SE is a primary seawater signature, it must be an expression of non-steady-state changes to the Earth systems because the extremely negative $\delta^{13}C_{carb}$ signature of the SE is below the conventional values of mantle-derived carbon sources (i.e., -5‰ to -6‰; Kump and Arthur, 1999; Melezhik et al., 2005). Consequently, traditional steady-state mass balance models cannot readily explain the SE (Kump and Arthur, 1999), and instead it must reflect input of a highly ^{13}C-depleted carbon source to the global dissolved inorganic carbon (DIC) pool. Some researchers argue that these extreme non-steady state conditions reflect a transition to more oxic conditions, which could have stimulated the evolution of macroscopic animals by allowing for more oxygen-consuming metabolisms (Fike et al., 2006; McFadden et al., 2008; Rothman et al., 2003). Under such a scenario, rising oxygen levels would culminate in the oxidation and remineralization of a pool of organic-derived carbon. Several possibilities have been proposed for the source of this carbon: 1) a large dissolved organic carbon (DOC) reservoir (Fike et al., 2006; McFadden et al., 2008; Rothman et al., 2003; Shi et al., 2017), 2) methane clathrates (Bjerrum and Canfield, 2011), 3) expelled hydrocarbons (Lee et al., 2015), and 4) terrestrial sedimentary input (Kaufman et al., 2007; Shi et al., 2018).

Out of these possibilities, the mechanism that has garnered the most attention is the DOC hypothesis (Fike et al., 2006; Rothman et al., 2003). This hypothesis posits that a large DOC reservoir (Rothman et al., 2003), at least 2-3 orders of magnitude greater than the modern reservoir of 662 Pg C (Hansell, 2013), resided in the deep ocean during the Ediacaran and that its oxidation added massive amounts of ^{13}C-depleted carbon to the DIC pool. Because the DOC reservoir was so massive and sustained heterotrophic food webs, carbon isotope ratios in sedimentary organic matter ($\delta^{13}C_{org}$) were buffered, resulting in a decoupling between the $\delta^{13}C_{carb}$ and $\delta^{13}C_{org}$ records (Fike et al., 2006). Indeed, this apparent decoupling between these two records is one of the more unusual characteristics of the SE (Swanson-Hysell et al., 2010), resulting in wide support for the DOC hypothesis. Nevertheless, it remains controversial, in particular given the implications for sources of oxidants required to drive the anomaly if it was as long-lived as believed. Bristow and Kennedy (2008) estimated that even with optimistic levels of oxidant availability, a CIE below mantle values can only be maintained for several hundreds of thousands of years, which is well below most estimates for the SE duration. On the other hand, Shields et al. (2019) suggested that increased weathering of evaporite sulphate minerals during the Ediacaran may have produced a surplus of oxidants capable of sustaining an excursion between -10‰ and -15‰.

An alternative mechanism to the DOC hypothesis has been proposed based on organic carbon and lipid biomarker data obtained from a marine organic-rich deepwater equivalent of the Shuram Formation from the South Oman Salt Basin (Lee et al., 2013; 2015). Here, biomarker signatures recorded through the SE interval imply contributions from multiple sources, while similarities in the magnitude and stratigraphic variation of $\delta^{13}C_{org}$ values between kerogen and bitumen reflect a non-migrated syngenetic source (Lee et al., 2013). This implies that the bulk $\delta^{13}C_{org}$ values through the SE interval likely did not represent a single homogeneous carbon source, such as a large DOC reservoir. Lee et al. (2015) proposed that the SE can be explained via enhanced mass transfer of hydrocarbon fluids between the Earth's geosphere and hydrosphere. Under this scenario, expelled petroleum derived from ^{13}C-enriched source rocks deposited earlier in the Neoproterozoic was variably remineralized, driving an extreme negative $\delta^{13}C$ anomaly in the DIC reservoir, and heterotrophically incorporated into organic matter that mixed with inputs from primary producers utilizing the DIC pool. This scenario would require a large enough hydrocarbon flux to fully account for the SE's duration, which is currently the strongest challenge against this hypothesis (Shi et al., 2017).

1.3.3 Diagenetic Origin

In contrast to models that interpret the SE as a primary perturbation to the global carbon cycle, several models invoke a diagenetic origin. Under this scenario, the $\delta^{13}C_{carb}$ values recorded in Ediacaran marine carbonates are not representative of the global DIC reservoir, but rather reflect secondary processes that have altered the rock's original isotopic composition. In these models, the bulk $\delta^{13}C_{carb}$ values in the SE reflect mixing between primary and secondary phases of carbonate and therefore do not record seawater compositions.

The basis for most of these models stems from the covariation between $\delta^{13}C$ and $\delta^{18}O$ values observed in SE carbonates (Derry, 2010; Grotzinger et al., 2011; Knauth and Kennedy, 2009). For example, both Knauth and Kennedy (2009) and Derry (2010) associate this correlation with fluid-rock interactions that alter the bulk $\delta^{13}C_{carb}$ signature of the carbonates post-depositionally. The key difference in these interpretations is the source of the ^{13}C-depleted fluid. Whereas Knauth and Kennedy (2009) proposed a meteoric source based on similarities between carbon and oxygen isotope systematics of SE carbonates and Phanerozoic examples altered by groundwater, Derry (2010) proposed a deep-burial setting based on modelling results that associate $\delta^{13}C$ and $\delta^{18}O$ values with high pCO_2 and depleted $\delta^{13}C$ fluids.

Despite these arguments, however, field observations in combination with isotopic datasets obtained from the Wonoka Formation in South Australia suggest a purely diagenetic origin for the SE is unlikely. Husson et al. (2012) conducted an "isotope conglomerate" test in which the isotopic compositions of redeposited carbonate breccia clasts in deeply incised paleocanyons of the Wonoka Formation were compared with their intact canyon shoulder equivalents, where the clasts were sourced. This study showed that the $\delta^{13}C$ values of the two were identical, indicating that any alteration that may have taken place would have had to occur prior to deep burial in the canyon fill. Similarly, Husson et al. (2015b) highlight the exceptional preservation of sedimentary structures observed in many Wonoka carbonates, which would not be expected of surfaces strongly altered by meteoric diagenesis. Moreover, where exposure surfaces are present, $\delta^{13}C_{carb}$ profiles indicate a general pattern of positive $\delta^{13}C_{carb}$ values close to the exposure horizon (Husson et al., 2015b), the opposite behaviour of what is expected from profiles of meteorically altered successions (Allan and Matthews, 1982).

An alternative interpretation of the SE, which allows for an early syn-deposition origin is that it resulted from the precipitation of authigenic carbonates. Early authigenic carbonates consists of $CaCO_3$ minerals and cements that grow *in-situ* either at or below the sediment-water interface (Schrag et al., 2013). This authigenic carbonate precipitation is believed to be driven by anaerobic microbial processes which can alter pore-water chemistry, leading to carbonate dissolution, cementation, and/or reprecipitation of $CaCO_3$ with a geochemical composition imparted in part by sedimentary organic carbon (Lein, 2004). Although authigenic carbonates are typically not considered in models of the global carbon cycle, recent modelling results suggests that they may account for at least 10% of the modern global carbonate budget (Sun and Turchyn, 2014). Given that authigenic carbonate precipitation is inhibited by O_2 in seawater (i.e., the acidity generated by the oxidation of reduced carbon compounds decreases the saturation state of $CaCO_3$), Schrag et al. (2013) suggested that the low-O_2 atmospheric and oceanic conditions during the Proterozoic (Lyons et al., 2014; Planavsky et al., 2014; Sperling et al., 2015) would have favoured a higher proportion of carbon being buried as authigenic carbonates. Consequently, the $\delta^{13}C_{carb}$ trends observed during the Proterozoic may have been influenced by the waxing and waning of a large ^{13}C-depleted sink of carbon in authigenic carbonates (Macdonald et al., 2013; Schrag et al., 2013).

One challenge to this hypothesis is that the Precambrian $\delta^{13}C_{carb}$ record is biased towards shallow-water carbonate platform deposits, an environment not ideally suited for authigenic carbonate production (Schrag et al., 2013). Consequently, most documented examples of highly ^{13}C-depleted authigenic carbonates are from the Phanerozoic (Jiang et al., 2019), and little empirical evidence linking this mechanism to the SE. Cui et al. (2016, 2017) report negative $\delta^{13}C_{carb}$ values in authigenic calcite cements and nodules in the upper Doushantuo Formation in the Zhongling section of Southern China, while Macdonald et al. (2013) report negative $\delta^{13}C_{carb}$ values in carbonate cements and nodules from the shale-dominated Blueflower Formation in Northwestern Canada. While the Blueflower example does occur slightly above the expected SE equivalent in Northwestern Canada, both examples from China are believed to be contemporaneous with the SE. Interestingly, $\delta^{13}C_{carb}$ values in each of these instances reach values below -34‰, suggesting that the SE may reflect an enhanced period of authigenic carbonate production within pore-waters in the sulphate-methane transition zone (SMTZ). Indeed, while the depth of SMTZ in modern sediments is highly variable, Cui et al. (2017) suggest that the anoxic nature of the early oceans coupled with lower seawater sulphate concentrations may have placed the SMTZ at much shallower depths close to the sediment-water interface. Moreover, increased Neoproterozoic oxidation of surface environments would likely have driven the SMTZ to greater depths, while concurrently promoting anerobic oxidation of methane by sulphate-reducing microbial communities. This scenario can also act as a good explanation for the widespread deposition of phosphorites during the Ediacaran (Papineau, 2010), while highlighting its association (particularly in South China) with the SE (Cui et al., 2016).

While authigenic diagenesis can account for some features of the SE, its occurrence as a truly global geobiological response is still challenged by other data. For example, a recent *in situ* carbon isotope study conducted on the Wonoka Formation in South Australia detected authigenic dolomite grains that were isotopically enriched in $\delta^{13}C_{carb}$, while co-occurring detrital calcite grains were isotopically depleted (Husson et al., 2020). In addition, similar analyses have also been done on ooids and calcite cements from the Shuram Formation in Oman (Bergmann, 2013) and dolostone samples from the Doushantuo Formation from the Jiulongwan section in South China (Cui et al., 2021), with both suggesting either a rock-buffered system during early diagenesis, or a geochemical composition indistinguishable from background DIC. The results of these studies support the view that, although an early diagenetic component can be detected and quantified in SE examples across several Ediacaran basins, the isotopic composition of the SE expressed in bulk carbonate measurements are still more likely to reflect a primary seawater composition. Importantly, however, highly negative $\delta^{13}C_{carb}$ values detected in authigenic calcite nodules in the Zhongling section in China (Cui et al., 2017; 2019) may yet suggest an association between early diagenetic processes and the SE, albeit in a more restricted or localized manner.

1.4 Bayesian Statistics

1.4.1 Preface

Geochronology and the development of accurate age-models represents one of the most important, yet challenging undertakings in documenting and understanding Earth history. Precise ages and depositional rates are required to infer environmental, biological, and geological events through time and to contextualize their importance with regards to Earth evolution (Halverson et al., 2018). Indirectly, accurate age-models are also important given their application as chronological tools for correlating these events across multiple paleobasins and for calibrating the geological record (Halverson et al., 2005; Rooney et al., 2020). However, even with many recent advances in the field of geochronology, many gaps remain in the stratigraphic record. These gaps are due in part to many stratigraphic sections lacking suitable lithologies (such as felsic volcanic flows and air fall tuffs) required for precise dating. This problem is particularly evident in Precambrian strata, where biostratigraphy cannot be viably utilised for correlation and indirect dating, and where astrochronology carries a greater degree of uncertainty (Hinnov, 2013).

A common strategy for inferring ages in stratigraphic gaps is through classical statistical techniques that interpolate ages between dated horizons, such as linear or polynomial regression, and spline fitting (Blaauw and Heegaard, 2012). These techniques generally attempt to fit a smooth curve through a set of data to relate stratigraphic position and age. While the approach is straightforward, it has several limitations. Firstly, the fit curves do not necessarily pass through each of the data points and generally require a least squares approach to generating a best fit. Consequently, stratigraphic relationships are not adequately considered which can result in age estimations that violate the law of superposition (Blaauw and Heegaard, 2012). Secondly, these classical modelling techniques tend to assume constant sediment accumulation rates without considering the tectonic context in which accommodation space is being produced. This can lead to inaccurate chronologies, such as where the controlling factor for sedimentation is accommodation space generation (i.e., any environment where sediment supply outpaces or keeps pace with accommodation space generation; Allen and Allen, 2013) rather than discrete sedimentation events (Haslett and Parnell, 2008). And thirdly, both stratigraphic and temporal uncertainties are generally underestimated, resulting in uncertainties that unrealistically increase away from the dated horizon (De Vleeschouwer and Parnell, 2014).

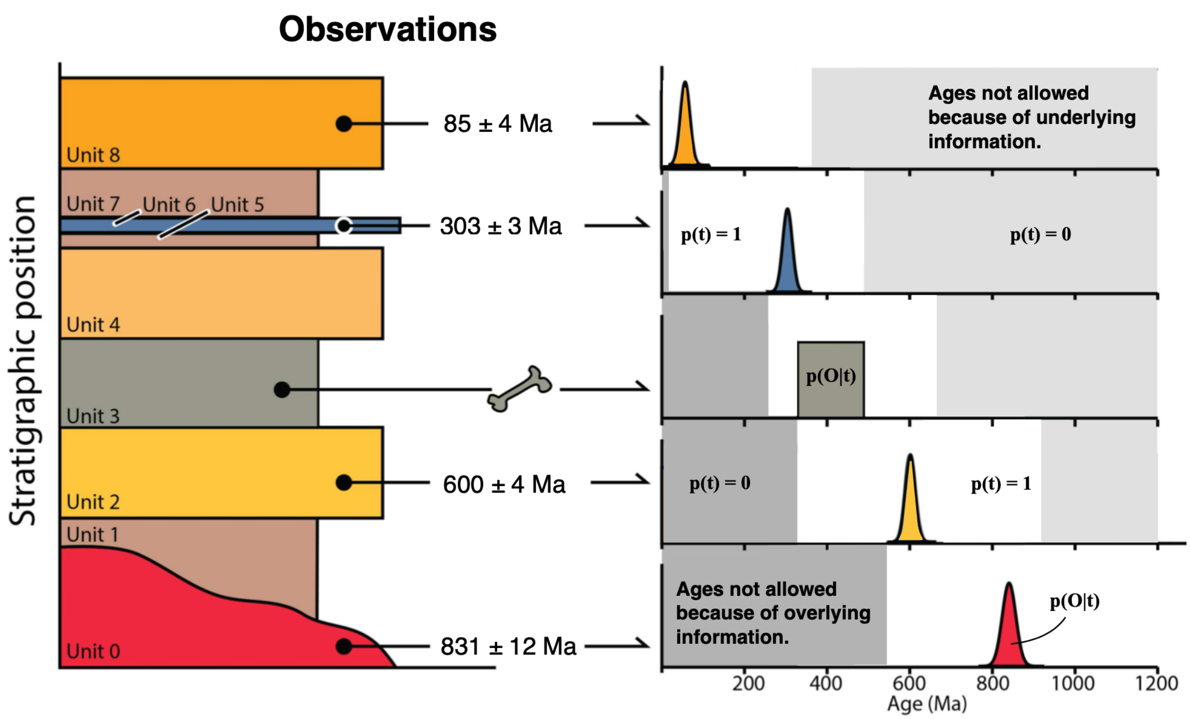

Figure 1.3 | Bayesian Age-Depth Modelling: A cartoon illustrating the use of Bayesian statistics to enforce the law of superposition. Age ranges that violate this law are shaded in gray and are assigned a *prior probability*, *p(t)*, of zero. The *likelihood distribution*, *p(O|t)*, is determined by the geochronological method used to obtain the age (i.e. a normal distribution for radiometric ages, and uniform distribution for ages based on biostratigraphy). *Modified from Johnstone et al. (2019)*

A more recent approach to dealing with these problems is through the development of age-depth models using Bayesian statistics. Bayesian age-depth modelling is advantageous over classical approaches in that it combines collected data with prior geological knowledge to generate more robust age estimates and more realistic uncertainties (De Vleeschouwer and Parnell, 2014). That is, model ages are estimated based on a prior term, which can include geological information such as the law of superposition and conditioned by a likelihood term represented by observed data. Taken together, the relationship between actual age determinations and stratigraphic position determines the posterior conditional probability distribution of the model age. Although this approach was originally developed for calibrating recent chronologies dated via radiocarbon (Bronk Ramsey, 2008; Haslett and Parnell, 2008), recent adaptations have seen Bayesian age-depth modelling being applied to a wider range of geochronological data (De Vleeschouwer and Parnell, 2014; Halverson et al., 2022; Johnstone et al., 2019; Schoene et al., 2019; Trayler et al., 2019).

1.4.2 Age-Depth Modelling

Where direct measurements are unavailable, Bayesian age-depth modelling is an effective approach for generating probable ages that consider the inherent uncertainty associated with radiometric dating, correlated stratigraphic positions, and geochronological techniques. This approach is particularly effective given that the probability of the age estimate is constantly updated based on the confidence of how the deposit age was originally obtained, and what is already known about the stratigraphic unit in question. Formally speaking, this relationship can be described by Bayes' Theorem,

$$p(t|O) = \frac{p(t)\,p(O|t)}{p(O)} \tag{1}$$

where $p(t|O)$ is the probability of the model age given the observation (i.e., the posterior distribution), $p(t)$ is the probability of the deposit age before acquiring the data (i.e., the prior distribution), *p(O|t)* is the likelihood of observing the data given the model age (i.e., the likelihood distribution), and *p(O)* is the evidence for the model age, which generally refers to the average of the likelihood taken across all values of the model age and weighted by the prior distribution (Kruschke, 2015). In many cases, this final term is hard to quantify, making it extremely difficult to solve Bayes' Theorem analytically. However, a common solution to this problem is the use of Markov Chain Monte Carlo (MCMC) techniques to approximate the posterior distribution, which is proportional to the product of the prior distribution and likelihood distribution (Johnstone et al., 2019). In addition, given a large enough sample size such that the parameter space of the unknown variable can be fully explored, this approximation should begin to approach the true posterior distribution of the model term in question (Kruschke, 2015).

With regards to quantifying the likelihood and prior terms, this determination is ultimately situational and dependent on the available data. For example, consider a stratigraphic section whereby age estimates and their stratigraphic position are obtained through a variety of methods (i.e., a combination of radiometric dates and correlated dates based on biostratigraphy) and have overlapping uncertainties both temporally and spatially. Here, the likelihood distribution type can be chosen based on the strength of the geochronological method (i.e., a normal distribution for radiometric dates and a uniform distribution for ages based on biostratigraphy; Johnstone et al., 2019), while the prior term can be set up such that ages going up-section must progressively get younger (*Figure 1.3*; Bronk Ramsey, 2009; Johnstone et al., 2019):

$$p(t) = \begin{cases} 1, & if\ t_0 > t_1 \ldots > t_n \\ 0, & if\ otherwise \end{cases} \tag{2}$$

Under this scenario, random age-depth combinations can be sampled through a MCMC algorithm, with the posterior distribution being updated based on these geological and technical constraints. The result here is that age-depth combinations that violate the law of superposition should be rejected, causing overlapping temporal and stratigraphic uncertainties to decrease.

1.5 The Huqf Supergroup, Oman

1.5.1 Preface

The Huqf Supergroup in Oman is one of the most complete and representative records of Ediacaran strata. It is well exposed in outcrops located on topographic highs, such as the Jabal Akhdar region of the Oman mountains and the Mirbat and Huqf areas. It also occurs extensively in the subsurface where it is penetrated by numerous oil wells due to its hydrocarbon productivity (Bowring et al., 2007; Forbes et al., 2010). The lower Huqf Supergroup comprises mixed diamictite-siliciclastics of the Abu Mahara Group (Allen, 2007), which sits unconformably atop a ca. 800 Ma crystalline basement. This group represents an early stage in the basin's formation and preserves glaciogenic components thought to be related to ca. 635 Ma Marinoan glaciation (Allen et al., 2004; 2011).

The Abu Mahara Group is overlain by the Ediacaran Nafun Group, which is characterized by extensive sheets of carbonate and siliciclastic sedimentary rocks. The Nafun Group is subdivided into the Hadash, Masirah Bay, Khufai, Shuram, and Buah formations, and is thought to have been deposited in a thermally subsiding basin following extensional rifting during the deposition of the Abu Mahara Group (Le Guerroué et al., 2006; Allen, 2007). The Hadash Formation is the basal Ediacaran cap dolostone, deposited during the post-Marinoan glaciation. The pronounced negative $\delta^{13}C_{carb}$ values of the SE were also first discovered in Nafun Group stratigraphy (Burns and Matter, 1993), with the initial excursion occurring at the Khufai-

Shuram boundary, reaching its nadir of approximately -12 ‰ in the mid-Shuram formation, and recovering to its initial values in the mid-Buah formation (Bowring et al., 2007).

The final subgroup of the Huqf Supergroup is the Ara Group. It sits unconformably above the Nafun Group and extends through the Ediacaran-Cambrian boundary into younger stratigraphy. This group comprises carbonate to evaporite sequences of varying thicknesses (Amthor et al., 2003) and is believed to mark a tectonic transition in basin evolution (Allen, 2007). There is evidence of renewed volcanism, uplift of basement blocks, and an overall segmentation of the basin characterized by structural crests and troughs (Allen, 2007; Bowring et al., 2007). U-Pb zircon ages obtained from volcanic ash beds also constrain the lowermost segment of the Ara group to ca. 547 Ma (Bowring et al., 2007).

1.5.2 The Abu Mahara Group

The Abu Mahara Group primarily outcrops in the Jabal Akhdar area in northern Oman, although partially time-equivalent sections are also well-exposed in the Mirbat area in southern Oman. In the Jabal Akhdar, the Abu Mahara Group is comprised of the Ghubrah, Saqlah, and Fiq formations, with the Ghubrah Fm. believed to correspond to units from the Mirbat Group (Rieu et al., 2006; 2007). Here, the stratigraphy of the Ghubrah Fm., and all stratigraphy occurring below the Saqlah Fm., is not well understood given its poor exposure and due to it having undergone extensive deformation. However, coeval diamictites and alternating fluvial/deltaic deposits occurring in paleovalleys in the Mirbat area suggests that deposition prior to the Fiq Fm. was part of an overall lowstand systems tract (LST) where ice sheets advanced and receded upon a terrestrial to marginal marine setting (Rieu et al., 2006).

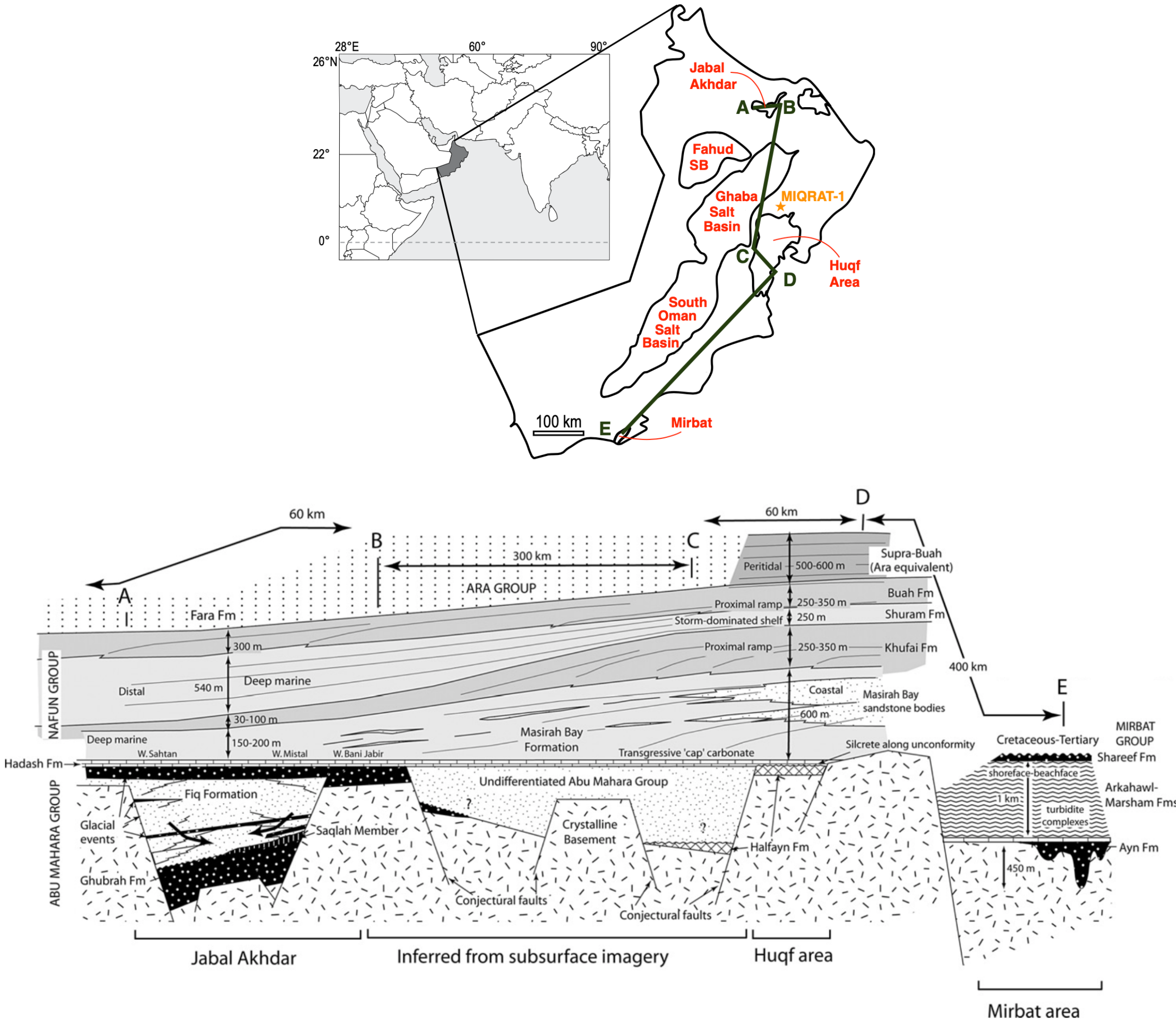

Figure 1.4 | Stratigraphy of the Huqf Supergroup, Oman: A map showing the distribution of Neoproterozoic rocks in Oman. The location of the MIQRAT-1 well is indicated by the orange star. The stratigraphy of the Abu Mahara, Nafun, and Ara Groups are also shown along a cross-section in the Jabal Akhdar (A-B), Huqf (C-D), and Mirbat (E) areas in Oman. *Modified from Allen (2007) and Lee et al. (2015)*

The Fiq Fm. sits at the top of the Abu Mahara Group and comprises of a mixture of glaciogenic and non-glacial shallow marine sediments (Allen et al., 2004; 2011; Leather, 2001). In particular, the glacial units correspond to both proximal and distal facies associations, suggesting that these units were generated over variable water depths controlled by changing terrestrial ice volumes. Interglacial units are mainly comprised of gravity flow deposits and rippled sandstones, also indicative of deposition in an open water environment. Sediments were sourced from the sub-basin margins, before being overstepped by the deep-water dolomites of the Hadash Fm. The overall stratigraphy of the Fiq Fm. suggests dynamic glacial conditions, with its contact with the Hadash Formation marking the onset of the post-glacial transgression (Allen et al., 2004).

The Saqlah Member directly underlies the Fiq Fm. and primarily comprises basaltic flows indicative of rift-related volcanism (Allen, 2007). Along with the overlying Fiq Fm., the sedimentology of the Saqlah Member indicates that the Abu Mahara Group was deposited during a stage of continental rifting. Indeed, seismic reflection profiles and data obtained from partially penetrating borehole wells (Gorin et al., 1982) suggest that the Abu Mahara Group is confined to a NE-SW trending rift basin that extends across eastern Oman (Allen, 2007; Loosveld et al., 1996). Moreover, sub-basin margins of crystalline basement rock are stratigraphically level with the overlying Hadash Fm. of the Nafun Group, marking a transition from the confined (graben) deposition of the Abu Mahara Group to the widespread sedimentation of the Nafun Group (Allen et al., 2004). This stratigraphic transition is characteristic of a basin evolving from fault-controlled subsidence to longer wavelength subsidence generated from the thermal relaxation of stretched continental lithosphere (Allen and Allen, 2013).

1.5.3 The Nafun Group

The Ediacaran Nafun Group consists of over 1 km of strata, commencing with the transgressive cap-dolostones of the Hadash Fm. This formation crops out in the Jabal Akhdar and Huqf areas of Oman, with potential correlative units in the southern Mirbat region. In the Jabal Akhdar, The Hadash Formation occur over a wide lateral extent (>70 km; Leather, 2001) and primarily comprises of dolomitic microspar intercalated with very fine-grained siliciclastics

(Allen et al., 2004; Leather, 2001). These sedimentary units do not feature any wave structures, evaporites, or any evidence of sub-aerial exposure, suggesting deposition in a deepwater environment. In contrast, in the Huqf area, dolostones of the Hadash Formation are coarser grained, thinly laminated, and feature mm-scale scour structures indicative of deposition in a shallower, higher energy environment (Leather, 2001). Moreover, the negative $\delta^{13}C$ excursion observed in Marinoan cap-dolostones is only recorded in the lower sections of the Hadash Fm. in the Jabal Akhdar region, while being absent from their equivalents in the Huqf area. However, given the wide basinal extent of these carbonates, Leather (2001) suggests that both units are likely to be associated with Marinoan deglaciation, with their differences in $\delta^{13}C$ either due to earlier carbonate deposition in the Jabal Akhdar area or due to local factors. This interpretation is supported by $\delta^{13}C$ values in the Jabal Akhdar region recovering to more positive values further up-section and is consistent with trends observed in post-Marinoan cap dolostones seen globally (Hoffman et al., 2007).

The Hadash Fm. is overlain by two siliciclastic-to-carbonate transgressive-regressive sequences comprising of the Masirah Bay, Khufai, Shuram and Buah formations. (Le Guerroué et al., 2006a). The Masirah Bay Fm. generally consists of marine sandstones, shales, siltstones, and interbedded limestones, with deeper water facies found in the Jabal Akhdar region in the north and shallower, higher energy facies in the Huqf region to the south (Allen and Leather, 2006; Le Guerroué et al., 2006a). The Masirah Bay Formation represents the continuation of the post-Marinoan transgression recorded by the Hadash Fm. and the onset of the succeeding regression, as it passes upwards gradationally into the carbonate ramp deposits of the Khufai Fm. The Khufai Fm. was deposited during a highstand systems tract (HST; Osburn et al., 2014) and varies laterally between the Jabal Akhdar and Huqf regions as a gently sloping, prograding carbonate ramp (Le Guerroué et al., 2006a; Osburn et al., 2014). The Khufai Fm. is followed by the Shuram Fm., which records a significant deepening event, as evidenced by a return to deeper water facies. The Shuram Fm. primarily comprises shales, siltstones, and calcareous interbeds, and represents the start of the second "grand cycle" or transgressive-regressive sequence of the Nafun Group (Le Guerroué et al., 2006a). This formation passes gradationally upwards into the carbonates of the Buah Fm., which was also deposited as part of a HST on a storm-dominated, distally steepened carbonate ramp (Cozzi and Al-Siyabi, 2004; Cozzi et al., 2004b).

At present, radiometric age dates that directly constrain depositional ages within the Nafun Group are limited (Rooney et al., 2020). As a result, age modelling efforts have historically been based on two tie points located at the base and top of the Nafun Group that bound this interval between ca. 635 Ma and ca. 547 Ma respectively (Al-Husseini, 2014; Forbes et al., 2010). The basal age constraint is based on the assumption that the base of the Hadash Fm. records the termination of the Marinoan Snowball Earth event dated elsewhere at ca. 635 Ma (Condon et al., 2005, Zhou et al., 2019). An upper age constraint at the Buah-Ara boundary is based on a chemostratigraphic correlation between the top of the Buah Fm. (Cozzi et al., 2004a) and a dated ash bed from the Nama Group in Namibia (ca. 547 Ma; Bowring et al., 2007; Grotzinger et al., 1995). These constraints, however, have resulted in inconsistent age models for the Nafun Group. For example, Le Guerroué et al. (2006b) interpolated the ages of formation boundaries by fitting a thermal subsidence curve between these tie points and assuming no stratigraphic gaps within the Nafun Group successions. Under these assumptions, an age of ca. 601 ± 8 Ma was estimated for the base of the Shuram Fm. In contrast, Bowring et al. (2007) used a series of geochronological constraints between Oman, China, and Namibia to calculate a range of sediment accumulation rates for the Buah Fm. By extrapolating these rates to the Shuram Fm., they estimated a Khufai-Shuram boundary age of ca. 558 ± 4 Ma. More recently, Gong and Li (2020) estimated sedimentation rates based on astronomically-forced cyclicities recorded in Nafun Group stratigraphy to extrapolate an age of ca. 570 ± 1 Ma for the base of the Shuram Fm. Recently published Re-Os ages now constrain the Khufai-Shuram boundary between ca. 562.7 ± 3.8 Ma and ca. 578.2 ± 5.9 Ma (Rooney et al., 2020), consistent with the estimate of Gong and Li (2020) but invalidating the earlier two age models. Therefore, despite the evidence for a rift-drift transition at the base of the Nafun Group (Le Guerroué et al.; 2006b), it seems unlikely that the entirety of the Nafun Group was deposited in a thermally-subsiding basin (Bowring et al., 2007). Rather, these new age constraints suggest that rates of accommodation space generation actually increased with time, suggesting a possible transition to the development of a foreland basin.

1.5.4 The Ara Group

The Ara Group represents a shift in basin mechanics, transitioning from the widespread subsidence-controlled deposition of the underlying Nafun Group into a tectonic style characterized by the segmentation of the Oman basin, with three smaller-scale sub-basins developed within the interior of Oman (Allen, 2007). The South Oman Salt Basin (SOSB), the Ghaba Salt Basin, and the Fahud Salt Basin, were each further segmented by localized basement fault blocking (Grotzinger and Al-Rawahi, 2014). Seismic reflection profiles and borehole penetrations show that the sub-basin compartmentalization is marked by major facies changes, with uplifted sections representing sites of carbonate production, while deeper troughs are characterized by the deposition of black shales, silicilyte, and salts (Amthor et al., 2005; Schröder et al., 2003). Moreover, both basinal and platform deposits are blanketed by evaporites, suggesting that evaporative depositional phases were controlled by tectonically induced subsidence and restriction (Schröder et al., 2003). Importantly, these evaporative phases are not representative of the classical sequence stratigraphic model of evaporite deposition in which lowstand basin-filling wedges onlap onto marginal highstand deposits. Rather, Ara Group evaporites overlap highstand carbonates, creating a carbonate-evaporite seal geometry ideal for hydrocarbon trapping and preservation (Al-Siyabi, 2005; Grotzinger and Al-Rawahi, 2014). The Ara Group is therefore one of the most important hydrocarbon systems in Oman, believed to potentially source younger overlying hydrocarbon systems (Terken et al., 2001). While Ara source rocks have yet to be formally identified, there is evidence suggesting that the deeper parts of these salt basins were at least periodically anoxic and ideal settings for the preservation of organic matter (Forbes et al., 2010; Schröder and Grotzinger, 2007).

Conclusion:

The Shuram Excursion has been the topic of many studies based on a diversity of approaches, yet a definitive model for its origin and even consensus on whether it truly represents a globally synchronous event remain elusive. One of the main obstacles to this problem is that many age-depth models developed for this time interval are spread across multiple paleobasins and are limited by radiometric ages within individual successions. Moreover, the testing of causative mechanisms for the SE has been hindered by inconsistent estimates of its age and duration, which has also led to inconsistent interpretations regarding its potential association with broadly contemporaneous geobiological events.

In the next chapter, I will apply chemostratigraphy and Bayesian statistical techniques to develop an updated age-depth model based on the Nafun Group stratigraphy in the MIQRAT-1 well of Oman. The results of this model will then be used to constrain the precise timing of the

SE and analyze it with respect to other mid-late Ediacaran geobiological events. The subsidence history of the Oman basin will also be reconstructed and used to re-evaluate incompatible age and duration estimates for the SE based on the same study region.

CHAPTER 2

Introduction:

Accurate and precise geological time scales are essential for analyzing and understanding Earth's history. The focus of this study is the ca. 635–539 Ma Ediacaran Period, for which the time scale remains poorly resolved despite the importance of the evolutionary events that occurred during this interval, such as the recovery from the Marinoan snowball glaciation, the origin of animals, and the Shuram negative carbon isotope excursion (SE). Recent advances in radioisotopic dating techniques, such as the increasingly applied Re-Os dating of organic-rich shales (e.g. Rooney et al., 2015; 2020), and a wider application of astrochronological (e.g. Gong and Li, 2020) and Bayesian age-depth modelling methods (Halverson et al., 2022; Matthews et al., 2021) have improved calibration of the late-Neoproterozoic record. However, despite these advances, the timing of the SE and its chronological position relative to other geobiological events in the Ediacaran is still poorly established. This ambiguity is primarily due to a paucity of available ages for the interval spanning the SE, but also because those that are available are spread across different paleobasins (Rooney et al., 2020; Yang et al., 2021).

In this chapter, we assemble the latest radiometric age constraints spanning the Ediacaran and correlate them into the Nafun Group stratigraphy of the MIQRAT-1 well, one of the most complete and representative Ediacaran successions globally. We then construct a Bayesian age-depth model based on this reference drill core and constrain the ages of important litho- and chemo-stratigraphic horizons. This age model is then used as 1) a basis for comparing the age and duration of the SE relative to those estimated from other sections globally, 2) a basis for comparing the timing of the SE relative to other geobiological events in the Ediacaran, and 3) a basis for modelling the subsidence history of Oman during Nafun times. Importantly, Oman is believed to potentially record the final stages of amalgamation of the supercontinent Gondwana in the East African Orogeny (EAO; Cox et al., 2012). Our subsidence model is used to test whether this final collisional event was temporally associated with other important evolutionary events during the Ediacaran, as has been suggested previously (Squire et al., 2006; Zhu et al., 2022).

2.2 Methods and Data

2.2.1 Correlated Ages

One of the primary goals of this thesis is to refine the chronostratigraphic framework of the Ediacaran Nafun Group of Oman. For this purpose, the MIQRAT-1 well was selected as a reference section for this age model due to its overall stratigraphic completeness and detailed carbon isotope record. The $\delta^{13}C$ record is particularly important given that there are currently no direct radiometric ages on this drill core, such that ages need to be correlated from other sections in Oman and other successions elsewhere. While this method is prone to a higher degree of stratigraphic uncertainty than direct dating, the unique magnitude of the SE, in addition to the stratigraphic position of distinct geological markers (e.g. the Marinoan cap-dolostones), allows for a relatively confident placement of chemostratigraphic tie-points to assist in the correlation. Moreover, given that both age and depth can be accounted for using Bayesian inference, this method allows us to maximize the amount of ages being applied to the model itself.

As shown in *Figure 2.1*, a total of 10 radiometric dates was used in this correlation. In addition to a measured age and its associated analytical uncertainty, a depth uncertainty was also assigned to each data point based on our confidence of the stratigraphic placement. While this

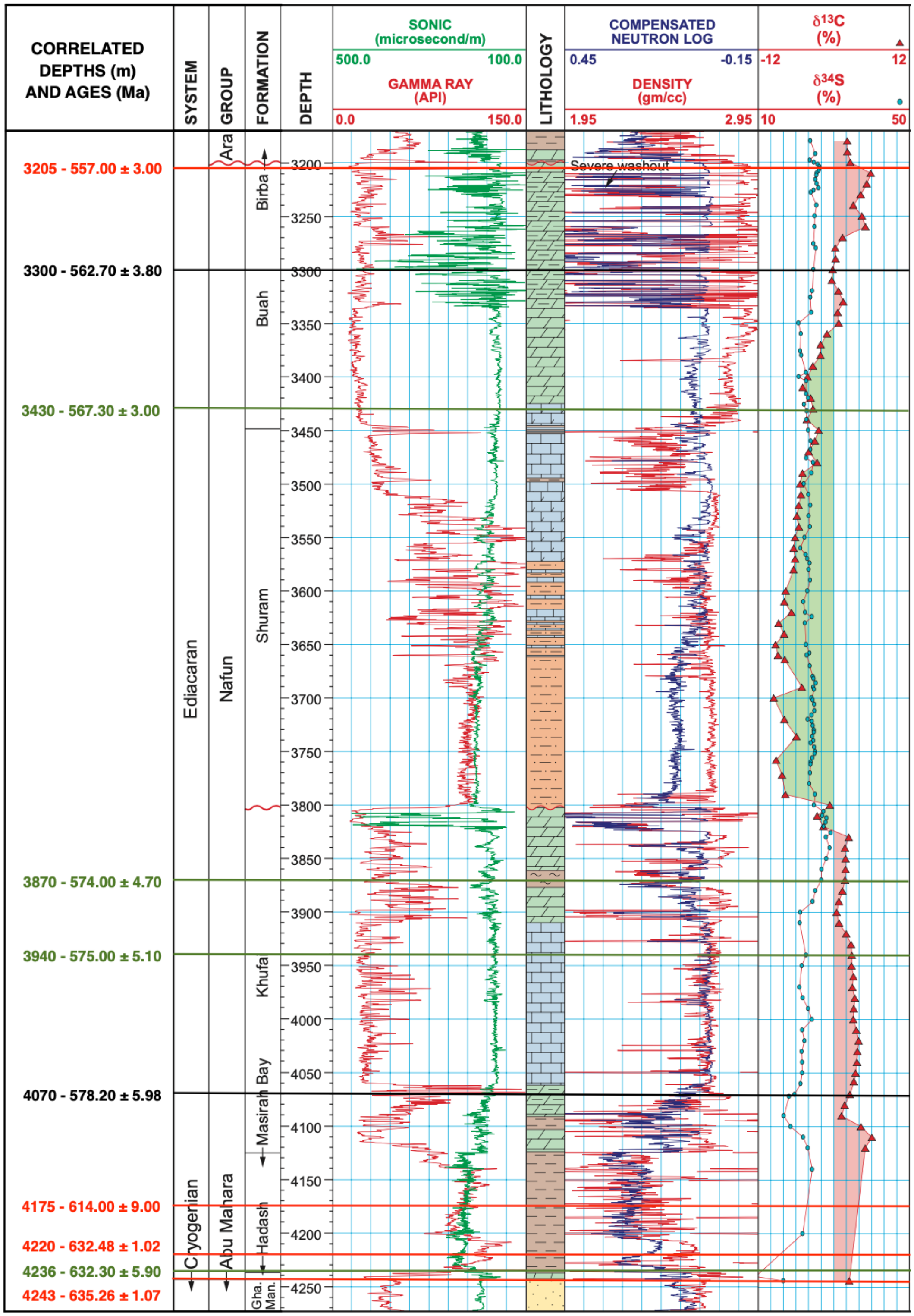

Figure 2.1 | Chemostratigraphy and Lithostratigraphy of the MIQRAT-1 Well: Drill core data showing the stratigraphic units of the Nafun Group and their corresponding $\delta^{13}C$ values. Correlated ages from South China (red), Oman (black), and northwestern Canada (green) are also shown. (*Modified from Forbes et al., 2010)*

approach can be subjective, we lean towards larger uncertainties to reflect our level of confidence in the correlations. The Bayesian component of the modelling updates the age-depth estimates based on geological information, namely the law of superposition. The radiometric ages used in this correlation were obtained from Oman, South China, and northwestern Canada, and are labeled here as samples MQ-1 to MQ-10 in chronological order. The age correlations are summarized in *Table 2.1*, and the reasoning behind their stratigraphic placements are described below.

Starting at the base of the Nafun Group, we assign a depth of 4243 ± 5 m to sample MQ-1, which corresponds to a weighted mean $^{206}Pb/^{238}U$ age of 635.26 ± 1.07 Ma obtained from three concordant zircon grains from an ash bed sample 2.3 m above the base of the Doushantuo Fm. in South China (Condon et al., 2005). This correlation is based on the stratigraphic position of the Marinoan cap-carbonates in Oman and China, which we use as chemostratigraphic tie-points for correlating between the two. In the case of Oman, this point corresponds to the basal Hadash Fm., while in South China, this point corresponds to the Lower Dolomite Member of the Doushantuo Fm., which is the cap carbonate to the Nantuo glacial deposits. Given that the basal Doushantuo Fm. is included in the Lower Dolomite Member and the Hadash Fm. has a very small stratigraphic thickness, we assign a relatively low depth uncertainty for this sample.

Sample MQ-2 corresponds to a Re-Os isochron date of 632.3 ± 5.9 Ma obtained from the Mackenzie Mountains in northwestern Canada (Rooney et al., 2015). This age was obtained from the basal Sheepbed Fm. 0.9 m above the Hayhook Fm., which is believed to be temporally equivalent to the Marinoan cap-carbonate. Here, we assign this sample a depth of 4236 ± 20 m. in our reference drill core based on its stratigraphic proximity to the Hadash Fm. Similarly, sample MQ-3, which has a weighted mean $^{206}Pb/^{238}U$ age of 632.48 Ma (Condon et al., 2005), is assigned a stratigraphic depth of 4220 ± 30 m. This sample was obtained from 3 concordant zircon grains from an ashbed 5 m above the Lower Dolomite Member in South China and is also correlated into the MIQRAT-1 well based on its position relative to the Marinoan glacial deposit/cap-carbonate couplet.

ID:	Sample Location:	Depth (m):	Depth Uncertainty (1σ):	Age (Ma):	Age Uncertainty (2σ):	Reference:
MQ-10 ∝	South China	3205	30	557.0	3.0	Zhou et al. (2018)
MQ-9 +	Oman	3300	60	562.7	3.8	Rooney et al. (2020)
MQ-8 +	NW Canada	3430	70	567.3	3.0	Rooney et al. (2020)
MQ-7 +	NW Canada	3870	30	574.0	4.7	Rooney et al. (2020)
MQ-6 +	NW Canada	3940	40	575.0	5.1	Rooney et al. (2020)
MQ-5 +	Oman	4070	35	578.2	5.9	Rooney et al. (2020)
MQ-4 ∝	South China	4175	50	614.0	9.0	Liu et al. (2009)
MQ-3 *	South China	4220	30	632.48	1.02	Condon et al. (2005)
MQ-2 +	NW Canada	4236	20	632.3	5.9	Rooney et al. (2015)
MQ-1 *	South China	4243	5	635.26	1.07	Condon et al. (2005)

Table 2.1 | Correlated Ages of the MIQRAT-1 Well: The inferred stratigraphic positions of various radiometric dates obtained from sections in south China, Oman, and northwestern Canada within the MIQRAT-1 well of Oman. * U-Pb TIMS zircon ages, + Re-Os isochron ages, ∝ U-Pb SHRIMP ages.

Sample MQ-4 has a U-Pb SHRIMP zircon age of 614.0 ± 9.0 Ma obtained from 18 zircon grains from a volcanic ash in the Zhangcunping area of South China (Liu et al., 2009). This ash is located between a black phosphorite and thick dolostone bed below an unconformity in the middle Doushantuo Fm. We correlate this age into the MIQRAT-1 well with a depth of 4175 ± 50 m based on chemostratigraphic trends from South China and chronostratigraphic constraints from Oman. Namely, this sample occurs at the crossover of a negative $\delta^{13}C$ trend following positive $\delta^{13}C$ values of the post-Marinoan carbon isotope excursion recovery and its correlation is constrained within the Masirah Bay Fm. at a greater depth to sample MQ-5.

Sample MQ-5 is a Re-Os isochron age obtained from organic-rich shales from the basal Khufai Fm. collected from Well L of Oman. This well was drilled in the South Oman Salt Basin and records some of the deepest water environments from this sub-basin. This sample yielded an age of 578.2 ± 5.9 Ma and records $\delta^{13}C$ values at ~3‰ prior to the onset of the SE (Rooney et al., 2020). Here, we assign this sample to a depth of 4070 ± 35 m based on its carbon isotope profile and its stratigraphic position relative to the SE chemostratigraphic tie-point.

Samples MQ-6, MQ-7, and MQ-8 were obtained from black calcareous mudstones in the Rackla Group of northwestern Canada. The first two samples were collected from the upper Nadaleen Fm. in the Wernecke Mountains and yielded Re-Os isochron ages of 575.0 ± 5.1 and 574.0 ± 4.7 Ma respectively (Rooney et al., 2020). These samples occur just below the Gametrail Fm. with enriched $\delta^{13}C$ values that plateau at ~9‰ (Macdonald et al., 2013; Rooney et al., 2020). As a result, we interpret these samples as closely preceding the onset of the SE and assign depths of 3940 ± 40 m and 3850 ± 30 m in the MIQRAT-1 well for samples MQ-6 and MQ-7 respectively. Sample MQ-8 was collected from map unit PH4 in the Ogilvie Mountains, which is loosely correlated to the Blueflower Fm. in the Wernecke and Mackenzie Mountains (Macdonald et al., 2013; Rooney et al., 2020). This sample yields a Re-Os depositional age of 567.3 ± 3 Ma (Rooney et al., 2020) and occurs after the termination of the SE in northwestern Canada. In the MIQRAT-1 well, however, the SE recovery is stratigraphically protracted relative to many global successions (Forbes et al., 2010). For this reason, we correlate sample MQ-8 with a depth of 3430 ± 70 m corresponding to the later stages of the SE recovery with $\delta^{13}C$ values at about -3‰ at the base of the Buah Fm.

Sample MQ-9 is a Re-Os isochron age measured from organic-rich shales from the Buah Fm. of Well M of the South Oman Salt Basin. This measurement yields a depositional age of 562.7 ± 3.8 Ma (Rooney et al., 2020) and occurs after the post-SE recovery to positive $\delta^{13}C$ values. Using the crossover point as a chemostratigraphic anchor, we assign this sample a depth of 3300 ± 60 m in the MIQRAT-1 well. Similarly, sample MQ-10 is correlated into our reference drill core using the terminal SE crossover as a chemostratigraphic tie-point. This sample is a U-Pb SHRIMP zircon date obtained from a K-bentonite from the lower Dengying Fm. in South China with a weighted-mean $^{206}Pb/^{238}U$ age of 557 ± 3 Ma (Zhou et al., 2018). This sample occurs after the termination of the Doushantuo negative carbon isotope excursion (DOUNCE) in South China, which we interpret as equivalent to the SE. As a result, we assign this sample with depth of 3205 ± 30 m in the MIQRAT-1 well.

2.2.2 Updating of Age-Depth Combinations

The first process used in developing an age model for the Nafun Group of Oman uses a Bayesian approach to update correlated data points that have overlapping age and/or depth uncertainties. This problem can arise due to correlated dates being closely spaced together or due to the data having large uncertainties. Here, the data, θ, consists of ages and stratigraphic depths whose probability distributions are treated as Gaussian. The central statistical descriptor for these distributions (i.e. the mean/median), μ, is thus treated as the unknown parameter, whose posterior distribution, $P(\mu_{age}, \mu_{depth} | \theta)$, is subsequently updated by approximating Bayes' theorem:

$$P(\mu_{age}, \mu_{depth} | \theta) \sim P(\theta | \mu_{age}, \mu_{depth}) * P(\mu) \quad (3)$$

Here, $P(\theta | \mu_{age}, \mu_{depth})$ is the likelihood of observing our data and is treated as the product of two Gaussian probability density functions centered about our proposed age and depth parameters with standard deviations defined by the uncertainty of our age-depth data:

$$P(\theta | \mu_{age}, \mu_{depth}) = N(\mu_{age}, sd_{age}) * N(\mu_{depth}, sd_{depth}) \quad (4)$$

and $P(\mu)$ is the probability of our parameters based on a prior belief. This prior constraint comes in the form of the law of superposition, which posits that an age obtained from a greater stratigraphic depth must be older than an age obtained from a shallower depth. Any randomly sampled age-depth combination that violates this condition would be assigned a probability of zero (Johnstone et al., 2019):

$$P(\mu) = \begin{cases} 1 & if\ t_0 > t_1 > \cdots t_n\ and\ d_0 > d_1 > \cdots d_n \\ 0 & if\ otherwise \end{cases} \quad (5)$$

Taken as a whole, the posterior distribution of our parameters will be conditioned by this geological constraint to exclude age-depth combinations that are out of stratigraphic order. As a result, the means (or medians) of overlapping ages and depths will begin to diverge, while their uncertainties begin to decrease. We use the Metropolis-Hastings Markov chain Monte Carlo (MCMC) to sample the posterior distribution of the updated ages and stratigraphic depths (with their uncertainties) (*Figure 2.2*) and assume the evidence term, $P(\theta)$, as a common factor.

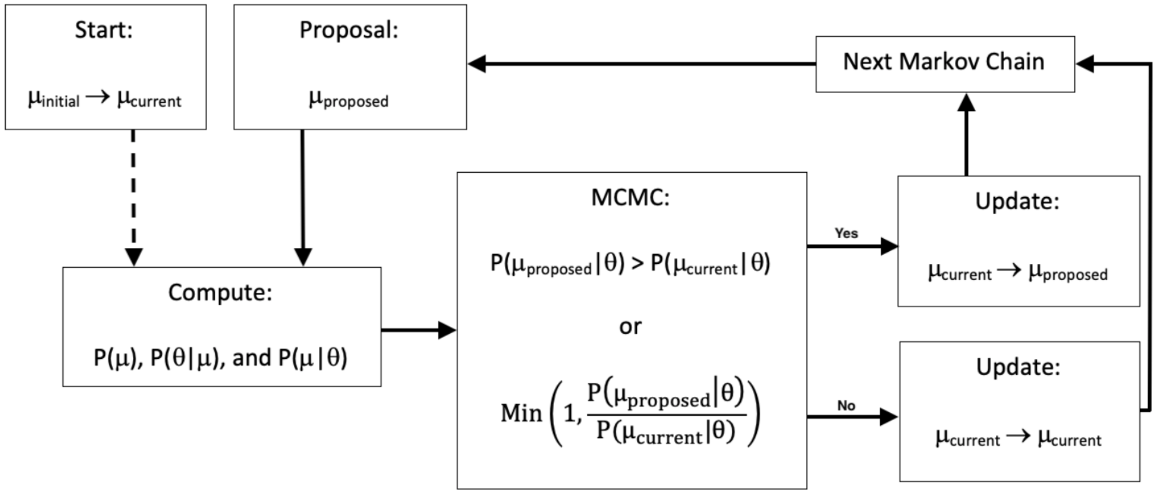

Figure 2.2 | Markov Chain Monte Carlo Flowchart: A simplified illustration of the Metropolis-Hastings algorithm. Here, a proposed parameter value is randomly sampled for every iteration of each Markov chain and compared with the current parameter value. The proposed parameter is either accepted or rejected probabilistically, before advancing to the next step in the Markov chain. In taking a sufficient amount of "random walks" through the parameter space, this algorithm will approximate the true posterior distribution of the parameter in question.

2.2.3 Bayesian Age-Depth Modelling

While the above Bayesian approach allows for specific age-depth combinations to be updated while considering realistic geological constraints, it is limited in that it does not estimate age-depth combinations at intervals between dated (or correlated) horizons. While classical statistical techniques, such as linear or polynomial regression, can be used to make such inferences, they too are limited in that they tend to underestimate uncertainties leading to unrealistic chronologies (De Vleeschouwer and Parnell, 2014). Other Bayesian methods are also available for this purpose (Halverson et al., 2022; Haslett and Parnell, 2008; Johnstone et al., 2019; Parnell et al., 2008; Trayler et al., 2019), but some methods are fine-tuned to specific geological or sedimentological scenarios not applicable to the MIQRAT-1 well. For example, Halverson et al. (2022) developed a method that generates chronologies based on the long-term subsidence caused by the cooling and densification of mantle material following instantaneous lithospheric stretching. While this method may be suitable for the early stages of Nafun Group deposition, the growing evidence that an additional mechanism was involved in generating accommodation space in Oman (Bowring et al., 2007) indicates that this method alone would not be capable of generating our age model. As an alternative, we considered using Bayesian regression to describe two curves to best fit our updated age-depth data: 1) a generalized thermal subsidence curve (i.e. where sediment accumulation is slow), and 2) a linear fit (i.e. where sedimentation rates increase). Drawbacks of this approach are that the generalized thermal subsidence curve enforces a specific shape to fit the data without considering the effects of sediment compaction, and the linear fit produces unrealistic uncertainties given its dependence on slope and intercept values. Moreover, given that we intend to perform a subsidence analysis on the MIQRAT-1 well in a subsequent procedure, basing our age model on a specific subsidence mechanism may lead to paradoxical or biased results.

To avoid this circular reasoning, we applied the open-sourced R-based *Modified BChron* package of Trayler et al. (2019) to generate our age model and to interpolate the ages at all depths between dated horizons. This method is an adaptation of the *BChron* method (Haslett and Parnell, 2008), another R-based package, which was originally developed for age-depth modelling of lake sediment archives dated via radiocarbon. This model treats deposition as a series of discrete sedimentation events, where the number of events is sampled from a Poisson distribution and the age gaps between each event are drawn from a Gamma distribution (Haslett and Parnell, 2008). Taken together, the parameters for this compound Poisson-Gamma distribution describes the prior probability of the sedimentation event occurring, which is then updated based on age-depth data through a MCMC sampler. The end result here is a piecewise linear posterior chronology that imposes monotonicity (Parnell et al., 2011), such that ages going up-section can only become younger. Another advantage of *BChron* is that it allows for a wide range of possible accumulation paths, removing any associated bias that may arise from assumptions regarding distribution shapes and resulting in more realistic uncertainty estimations (Trayler et al., 2019).

The reason we have chosen to use *Modified BChron,* as opposed to the original *BChron*, is that it is more adapted for deep-time applications. For example, while both of these methods use the Metropolis-Hastings algorithm to solve Bayes' theorem, *BChron* uses a scaling factor for their proposal distribution that is more amenable to chronologies dated by radiocarbon techniques (i.e. shorter timescales). Because this algorithm's efficiency to properly explore parameter space is dependent on this selection, *Modified BChron's* adaptive proposal algorithm is more flexible for working with older or longer-scaled chronologies. Moreover, *Modified BChron* also allows for multiple individual ages of the same sample to be grouped together, such that multiple U-Pb or $^{40}Ar/^{39}Ar$ ages can be inputted together to form a probability distribution, rather than needing these individual analyses to be convolved into a single age and uncertainty input (Trayler et al., 2019).

Modified BChron takes as input a dataset consisting of sample names, ages, age uncertainties (1σ), stratigraphic positions (i.e. the heights starting at the base of the section), stratigraphic half-thicknesses of the measured material, and probability distribution types (i.e. either Gaussian or Uniform). Since our input data consists of correlated age-depths, we treat the half-thicknesses as 1σ uncertainties to our stratigraphic placements and assume all probability distributions as Gaussian. In addition, stratigraphic positions are input as negative values because our drill-core data is reported as depths. All of these inputs are automatically adjusted following the Bayesian "fine-tuning" of our age-depths described above and fed into the *Modified BChron* algorithm. Here, the posterior distribution of the model parameters are generated over 20000 MCMC iterations with the first 2000 "burn in" values being discarded. The burn-in time is the time it takes for the algorithm to reach an equilibrium distribution, such that starting terms that may be far from its equilibrium value (i.e. lower probability terms) will not be over-sampled and contribute significantly to the posterior distribution. Each posterior sample is evaluated using Bayes' theorem with each iteration of each Markov chain proposing a new parameter from a Gaussian distribution and centered on the current parameter value. The probabilities of the proposed and current parameters are then compared probabilistically to decide whether to reject or accept the proposed parameter (Brooks et al., 2011; Kruschke, 2015; Trayler et al., 2019). As noted earlier, *Modified BChron* uses an adaptive algorithm to re-scale the input data such that the proposal algorithm generates a parameter value adequately spaced from its current value to properly and fully explore the parameter space. Upon completion, the median and 95% highest probability density interval (HPDI) is compiled from the posterior distribution for the entire sedimentary sequence, such that the model median ages (and uncertainties) of the stratigraphic horizons of interest can be extracted from the age model.

While *Modified BChron* offers an effective means of generating age estimates for undated stratigraphic horizons, one drawback needs to be considered for its use in this study. Specifically, the sedimentation scheme that this model is based on (i.e. discrete sediment accumulation events; Haslett and Parnell, 2008) does not adequately describe the mechanisms controlling sediment accumulation in the Huqf region of Oman. This is particularly evident for the early stages of Nafun Group deposition, where slow and long-term thermal subsidence appears to be the driving force for accommodation space production (Allen, 2007; Le Guerroué et al., 2006b). Nevertheless, *Modified BChron* offers an objective way of interpolating ages between dated horizons, especially considering that these ages will be used to make stratigraphic corrections in the subsequent procedure. Moreover, given that *Modified BChron* will adjust and approximate age estimates more accurately as sample sizes increase, this model can easily be updated in the future when more age constraints (or geological information regarding Oman) become available.

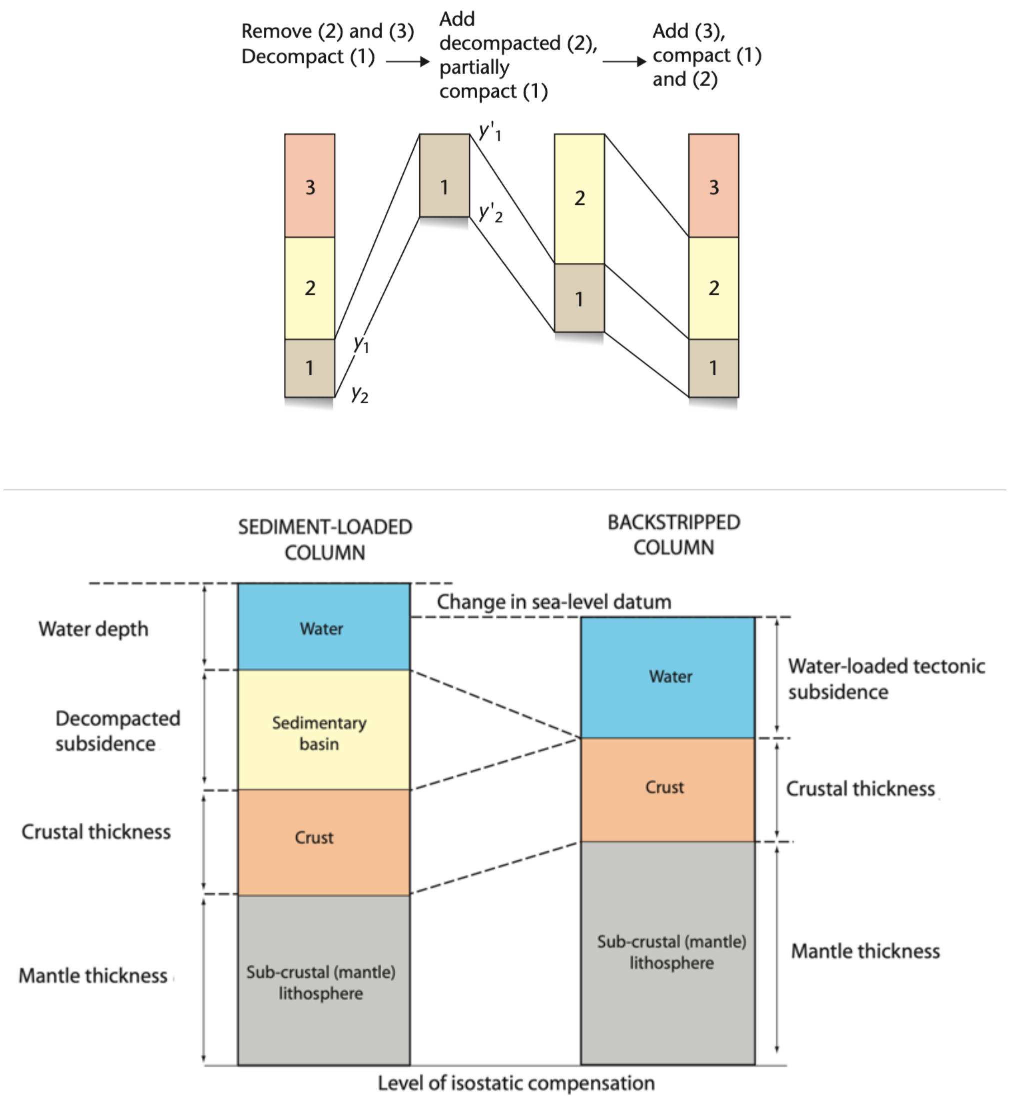

Figure 2.3 | Decompaction and Backstripping of a Sedimentary Section: The upper row illustrates the concept of removing layers of sedimentary strata to account for the loss of pore-space during sediment burial and compaction, while the lower row illustrates the isostatic balance used to remove these sediment-loading effects to obtain the tectonic subsidence. *(Modified from Allen and Allen, 2013)*

2.2.4 Decompaction

Once the ages of all the lithological boundaries in the MIQRAT-1 well are estimated, we can make corrections to account for any volume loss after sediment burial. Here, we follow the decompaction method proposed by Sclater and Christie (1980), which involves the removal of effects associated with the loss of pore space during sediment burial. We consider each sedimentary layer (separated by lithological boundaries) as having a volume of water-filled pore space, V_w, decaying exponentially with depth:

$$V_w = \int_{y1}^{y2} \emptyset_0 \, e^{-cy} \, dy \tag{6}$$

where ϕ_0 is the surface porosity, c is the porosity decay constant, and y_1 *and* y_2 are the corresponding depths at the top and base of the sedimentary unit respectively. Simplifying to a cross-sectional perspective, V_w can be expressed instead in terms of its unit length, such that V_w is equivalent to the thickness contribution of water-filled pore space, y_w, to the total thickness of the sedimentary layer, y_t. The thickness contribution of the sediment, y_s, can thus be expressed as follows upon integration of V_w:

$$y_s = y_2 - y_1 - \frac{\emptyset_0}{c}(e^{-cy_1} - e^{-cy_2}) \tag{7}$$

After decompaction of the layer, y_s can be assumed as being unchanged, while the new thickness contribution of water-filled pore space, y'_w, can be expressed in terms of the constraints set by the new decompacted thickness of the unit:

$$y'_w = \frac{\emptyset_0}{c}(e^{-cy'_1} - e^{-cy'_2}) \tag{8}$$

Finally, the new decompacted thickness of the sedimentary layer can be determined iteratively by setting this new thickness equal to the sum of the sediment and pore space contributions:

$$y_2' - y_1' = y_s + \frac{\emptyset_0}{c}\left(e^{-cy_1'} - e^{-cy_2'}\right) \tag{9}$$

As shown in *Fig. 2.3*, this process can be applied to the entire sedimentary section by removing overlying sedimentary layers, decompacting the basal formation, and then progressively reintroducing the overlying decompacted layers to the new partially compacted underlying units. In doing so, we allow for present-day thicknesses to be restored to their corresponding thicknesses at different times during their burial history, such that the stratigraphic horizons of different sedimentary formations are tracked as a function of time.

2.2.5 Backstripping

The backstripping method, also introduced by Sclater and Christie (1980), involves the removal of sediment loading effects in a corresponding basin such that the subsidence history of that basin can be analyzed in terms of its water-loaded tectonic subsidence. This technique is accomplished via two procedures: 1) the estimation of a bulk density as the sediment column evolves over time, and 2) the removal of the sediment-loading effects through the assumption of Airy isostasy.

Following the decompaction method above, the average porosity of a stratigraphic unit at any given depth is estimated by:

$$\emptyset_i = \frac{\emptyset_0}{c}\left(\frac{e^{-cy_1'} - e^{-cy_2'}}{y_2' - y_1'}\right) \tag{10}$$

Given the assumption that sediment pore spaces are filled with water, the bulk density of the sedimentary section with i layers, ρ_b, is calculated by:

$$\rho_b = \sum_i \left(\frac{\emptyset_i \rho_w + (1 - \emptyset_i)\rho_s}{S}\right) y_i' \tag{11}$$

where ρ_w and ρ_s are the densities of water and the sediment grain respectively, S is the total decompacted thickness of the sediment column, and y'_i is the decompacted thickness of the ith sediment layer. Finally, the water-loaded tectonic subsidence of the stratigraphic section, Y_w, is estimated through an isostatic balance:

$$Y_w = S\left(\frac{\rho_m - \rho_b}{\rho_m - \rho_w}\right) \tag{12}$$

where ρ_m, is the density of the mantle. Taking into consideration paleobathymetry and eustatic sea-level change, corrections can be made to the water-loaded subsidence by considering the change in sea-level relative to modern values, Δ_{SL}, and the paleo-water depth, W_d:

$$Y_w = S\left(\frac{\rho_m - \rho_b}{\rho_m - \rho_w}\right) - \Delta_{SL}\left(\frac{\rho_w}{\rho_m - \rho_w}\right) + (W_d - \Delta_{SL}) \tag{13}$$

However, given that there is currently no available global eustatic curve for the Ediacaran Period to make these corrections, we assume global fluctuations in sea-level to have a negligible (or small) effect on the overall tectonic subsidence. With regards to paleobathymetric corrections, we follow the approach of Le Guerroué et al. (2006b) and base these estimations on sedimentary facies. A summary of these estimates and their reasonings are listed in *Table 2.2*.

2.2.6 Bayesian Thermal Subsidence Modelling

After performing the decompaction and backstripping procedures to the MIQRAT-1 well, a subsidence profile is generated with a new set of age-depth combinations corresponding to the lithological boundaries corrected for volume change, water-depth, and sediment loading. While this profile alone can be used to make an analysis on the subsidence history of the basin, subsidence curves can also be fitted through this data to further constrain specific parameters, such as the stretching factor, β, which describes the ratio of the thickness of the lithosphere prior

Lithological Boundary:	Stratigraphic Depth (m):	Paleowater Depth (m):	Interpretation:
Buah Limestone-Dolostone Boundary	3427	5	Inner ramp setting. Above FWWB.
Shuram-Buah Boundary	3450	10	HST deposition on a storm-dominated carbonate ramp.
Shuram Limestone	3508	15	Shallowing upwards towards Buah boundary.
Shuram Shale-Limestone Boundary	3570	15	Shallowing upwards towards Buah boundary.
Shuram Shale Interbeds	3660	20	Shallowing upwards towards Buah boundary.
Khufai-Shuram Boundary	3800	30	Unconformity. Start of transgressive cycle.
Khufai Shale-Dolostone Boundary	3861	5	Just below maximum regressive surface.
Khufai Dolostone-Shale Boundary	3878	10	LST deposition.
Khufai Limestone-Dolostone Boundary	3910	15	LST deposition.
Khufai Dolostone-Limestone Boundary	4060	20	Hummocky cross-stratification and indications of sediment reworking. Storm-dominated mid-ramp setting.
Khufai Shale-Dolostone Boundary	4091	30	HST deposition.
Khufai Dolostone-Shale Boundary	4105	40	Outer ramp setting. Absence of Hummocky and Swaley cross-stratification (present in the Huqf region).
Masirah Bay-Khufai Boundary	4128	40	Maximum flooding surface. Outer ramp setting.
Hadash-Masirah Bay Boundary	4238	40	Scour structures in lower Hadash Fm. no longer present. Below SWWB.
Basal Hadash Fm.	4243	20	Scour structures. Above SWWB.

Table 2.2 | Paleowater Depths at Lithological Boundaries: Estimations of the paleowater depth at each lithological transition within the MIQRAT-1 well. These estimates are based on sedimentary structures described in successions within the Huqf region and sequence stratigraphic interpretations.

to and after being stretched. Here, we use Bayesian regression to generate our thermal subsidence curve while basing our predictor model to best fit the decompacted and backstripped subsidence profile.

This curve is modelled after the post-rift component of the 1D uniform stretching model (McKenzie, 1978) and describes the accommodation space produced via thermal subsidence:

$$S(t) \ = \left(\frac{4y_L\rho_m^*\alpha_v T_m}{\pi^2(\rho_m^* - \rho_w)}\right)\left(\frac{\beta}{\pi}\right)\sin\left(\frac{\pi}{\beta}\right)\left(1 - e^{\frac{-t}{\tau}}\right) \tag{14}$$

where *S(t)* is the water-loaded thermal subsidence as a function of time, α_v is the volumetric coefficient of thermal expansion, y_L is the initial lithospheric thickness, T_m is the asthenospheric temperature, ρ^*_m is the density of the mantle at 0°C, and τ is the thermal time constant for the lithosphere which can be defined as:

$$\tau = \frac{y_L^2}{\pi^2\kappa} \tag{15}$$

where κ is the thermal diffusivity. The typical values of these terms are listed in *Table 2.3* and their descriptions are explained in detail in Allen and Allen (2013). Importantly, the uncertainties associated with these terms are assumed to be negligible in the context of our model curve given the lack of evidence for magmatic activity, abnormal asthenospheric behavior, and stages of protracted rifting in Nafun Group deposits throughout Oman. As a result, we assume that thermal subsidence is dependent on the stretching factor alone and fix the values of all other parameters with their typical values. The exception here is β, which acts as the unknown parameter for which the posterior distribution is sampled. In addition, the rift-drift transition (*rdt*), which represents the starting age of the model curve, and a natural random deviation parameter, *sd*, are also sampled from the posterior distribution. Thus, the likelihood term for this Bayesian inference is:

$$P(Y_w|\beta, rdt, sd) \sim N(\mu = S(t), sd) \tag{16}$$

while our priors are based on previous studies. Namely, Armitage and Allen (2010) estimated extremely low subsidence and sediment accumulation rates across several cratonic basins, suggesting stretching factors as low as 1.12. This β factor was taken as our minimum possible value, while the maximum value was obtained from Le Guerroué et al. (2006b) who estimated a stretching factor of 1.41 for the MIQRAT-1 well. Importantly, this second value is treated as an overestimation given the previous assumption that the entirety of Nafun Group deposition was driven by thermal subsidence. Additionally, a "best guess" value for the stretching factor, β_0, can also be obtained by using the thermal subsidence data inversion method of Allen and Allen (2013), which allows us to set up the prior for β as a normal probability density function:

$$P(\beta) = \begin{cases} N(\mu = \beta_0, 0.02), & if\ 1.12 \leq \beta \leq 1.41 \\ 0, & if\ otherwise \end{cases} \tag{17}$$

Likewise, the prior for the rift-drift transition is also treated as a normal probability density function centered at the extracted model age for the base of the Hadash Fm, t_0:

$$P(rdt) = N(\mu = t_0, 0.5) \tag{18}$$

Since we do not have any meaningful prior notion regarding the amount of random deviation from our estimated curve values, we estimate the starting term visually and treat this prior constraint as an uninformative uniform distribution (i.e. a flat prior):

$$P(sd) = U(\min = 0, \max = 150) \tag{19}$$

Here, the minimum and maximum values are selected under the assumption that the natural deviation from our curve fit should not be negative or exceed 150 m. We tried varying these values and found that our results pertaining to β and *rdt* were largely unaffected.

Finally, we use the Metropolis-Hastings algorithm to approximate Bayes' theorem and generate a posterior distribution for β, *rdt* and *sd*. Importantly, the *sd* term here does not represent the uncertainty of our thermal subsidence model, but rather the natural scatter in the data. In this case, scatter is likely related to uncertainties regarding the values used during the decompaction and backstripping procedures. The actual uncertainty for this model, however, would then relate to the rift-drift transition age (i.e. the start age) and the possible values of β, which ultimately determines the amount of subsidence generated by this mechanism. Thus, the 95% HPDI is compiled from the posterior distributions of the model parameters and treated as the uncertainty interval for this model.

Parameter:	Value:	Description:
α_v	$3.28*10^{-5}$ (1/K)	Volumetric coefficient of thermal expansion.
y_L	125000 (m)	Lithospheric thickness before stretching.
T_m	1333 (°C)	Asthenospheric temperature.
ρ^*_m	3330 (kg/m^3)	Density of the mantle at 0°C.
ρ_w	1030 (kg/m^3)	Density of seawater.
κ	$1*10^{-6}$ (m^2/s)	Thermal diffusivity.

Table 2.3 | Parameter Values of the Thermal Subsidence Equation.

2.3 Results

2.3.1 An Updated Age Model for the MIQRAT-1 Well of Oman

The first component in developing our Bayesian age model for the MIQRAT-1 well of Oman consisted of "fine-tuning" the correlated ages based on the law of superposition. The results of this age-depth updating is shown in *Figure 2.4* and a summary of the posterior distributions of the updated ages and depths (along with their associated Markov chains) is shown in *Figure 2.5*. Here, the original age-depth correlations are shown in blue and have considerable overlap between some age and depth uncertainties. The updated data in red show the result of incorporating geological constraints to these correlations, such that uncertainties decrease and overlapping age-depth estimates diverge from one another. While the overall changes to the ages and depths are not significant, the reduction in their uncertainties help in further refining the age model generated by *Modified BChron*.

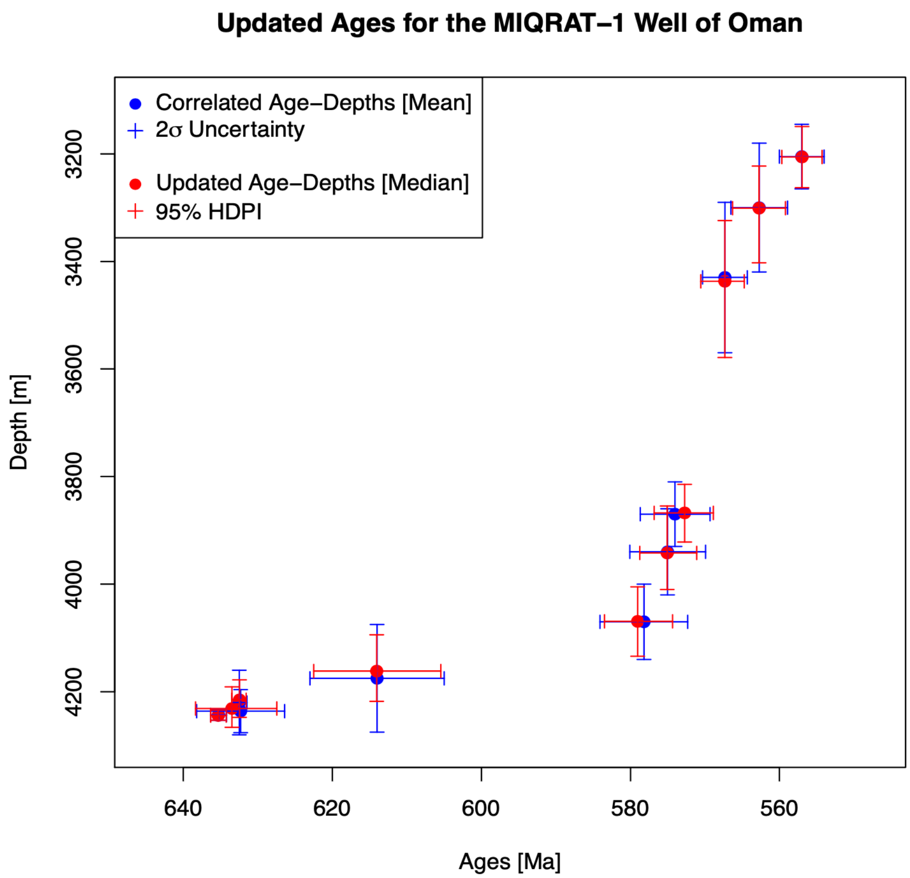

Figure 2.4 | Updated Ages for the MIQRAT-1 Well of Oman: A preliminary fine-tuning of age correlations into the MIQRAT-1 well. Bayesian inference was used to incorporate the law of superposition as a prior constraint, which reduced the amount of overlap between data points.

Importantly, the use of this "updating" procedure has a strong dependence on the relative accuracy of the initial age correlation. That is, updating by superposition assumes that the correlated ages are ordered correctly. In the case of our reference drill core, all age correlations are based on prominent chemostratigraphic and lithostratigraphic tie-points such as the distinctive $\delta^{13}C$ profile of the SE and the globally recognized Marinoan cap-carbonates. Given that these tie-points act as a strong foundation for basing our original stratigraphic placements, we are relatively confident that our correlations fall within the estimated uncertainty ranges. Furthermore, given that the majority of overlap within our samples is due to age-depth combinations being closely spaced together (rather than having wide uncertainty ranges), all adjustments made using our probabilistic approach are subtle and guided by the law of superposition. That is, age-depth adjustments only act to refine our input dataset, rather than to make drastic changes to our original interpretation of the age correlation. Importantly, this method consistently yielded stable Markov chains (*Figure 2.5C, D*) and similar posterior age-depth combinations between model runs, suggesting that the ordering of the correlated ages should be broadly accurate.

The Bayesian age model for the MIQRAT-1 well generated using *Modified BChron* is shown in *Figure 2.6*. This chronology comprises two main components, represented by a solid black line and a field of gray shading. The solid black line represents the median of the posterior model age, while the gray shading represents the 95% credibility interval. Importantly, this shading takes on a realistic shape, such that uncertainty increases away from dated horizons. Using this model fit, it was possible to estimate an age and the 95% HPDI for any stratigraphic depth within our reference drill core. We extracted a model age for each of the lithological boundaries listed in *Table 2.2*, as well as important depths of interest, such as the onset, nadir, and termination of the SE. The extrapolated ages of lithological boundaries are provided in *Table 2.4*, and the extrapolated ages associated with the SE are illustrated in *Figure 2.6*. Here, we follow the convention of Forbes et al. (2010) and define the SE interval as initiating at the crossover point to negative $\delta^{13}C$ values and terminating at the crossover point back to positive $\delta^{13}C$ values. That is, the onset age of the SE at is estimated at 571.45 +2.47/-2.98 Ma, the nadir of the SE at 570.44 +2.51/-2.91 Ma, and the termination age of the SE at 564.25 +2.84/-3.07 Ma.

These model ages correspond to stratigraphic depths of 3823 m, 3730 m, and 3353 m in the MIQRAT-1 well respectively.

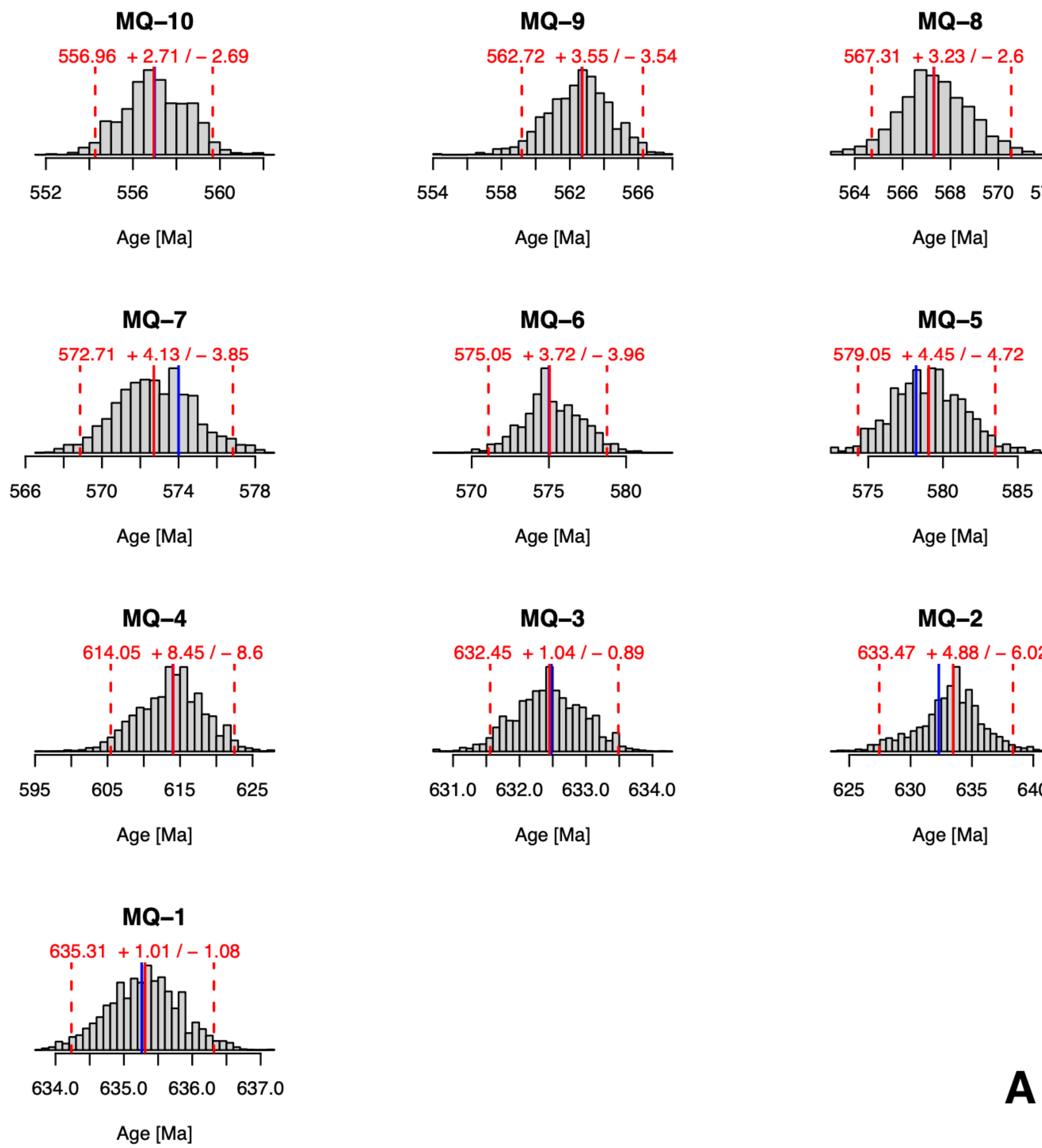

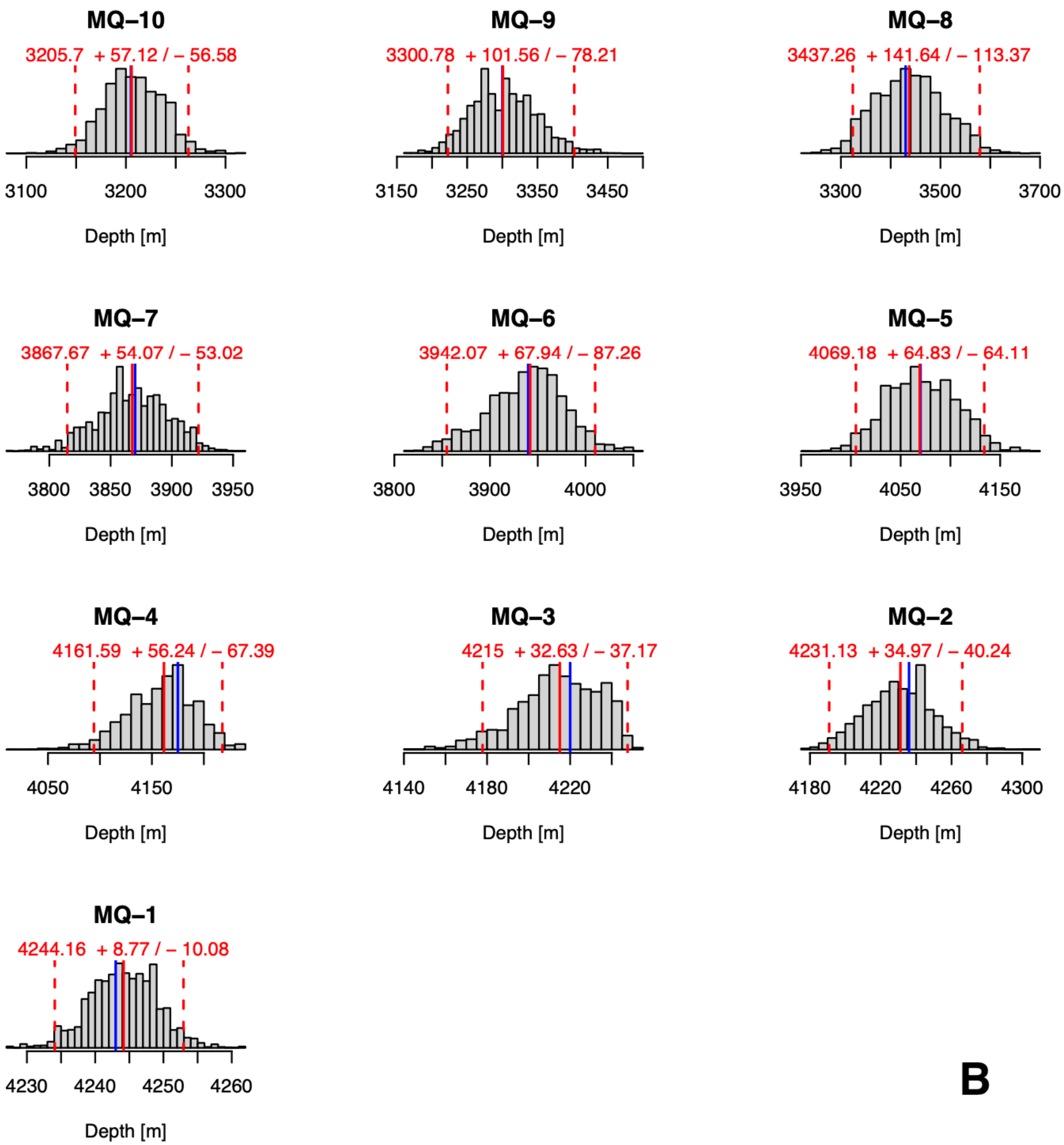
MQ–10
3205.7 + 57.12 / – 56.58
3100 3200 3300
Depth [m]
MQ–9
3300.78 + 101.56 / – 78.21
3150 3250 3350 3450
Depth [m]
MQ–8
3437.26 + 141.64 / – 113.37
3300 3500 3700
Depth [m]
MQ–7
3867.67 + 54.07 / – 53.02
3800 3850 3900 3950
Depth [m]
MQ–6
3942.07 + 67.94 / – 87.26
3800 3900 4000
Depth [m]
MQ–5
4069.18 + 64.83 / – 64.11
3950 4050 4150
Depth [m]
MQ–4
4161.59 + 56.24 / – 67.39
4050 4150
Depth [m]
MQ–3
4215 + 32.63 / – 37.17
4140 4180 4220
Depth [m]
MQ–2
4231.13 + 34.97 / – 40.24
4180 4220 4260 4300
Depth [m]
MQ–1
4244.16 + 8.77 / – 10.08
4230 4240 4250 4260
Depth [m]
B

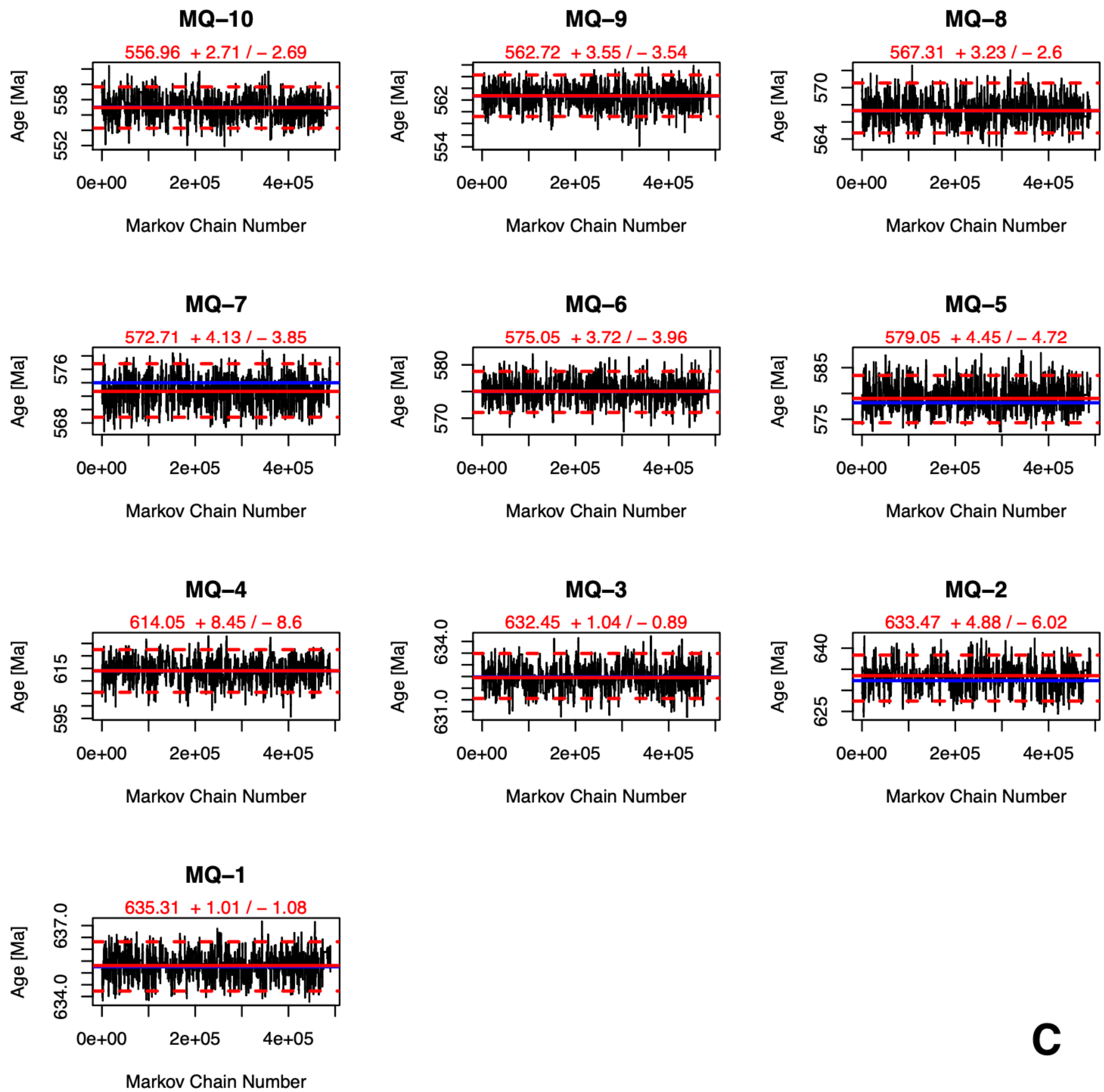
MQ–10
556.96 + 2.71 / – 2.69
MQ–9
562.72 + 3.55 / – 3.54
MQ–8
567.31 + 3.23 / – 2.6
MQ–7
572.71 + 4.13 / – 3.85
MQ–6
575.05 + 3.72 / – 3.96
MQ–5
579.05 + 4.45 / – 4.72
MQ–4
614.05 + 8.45 / – 8.6
MQ–3
632.45 + 1.04 / – 0.89
MQ–2
633.47 + 4.88 / – 6.02
MQ–1
635.31 + 1.01 / – 1.08
Age [Ma]
Markov Chain Number
0e+00
2e+05
4e+05
C

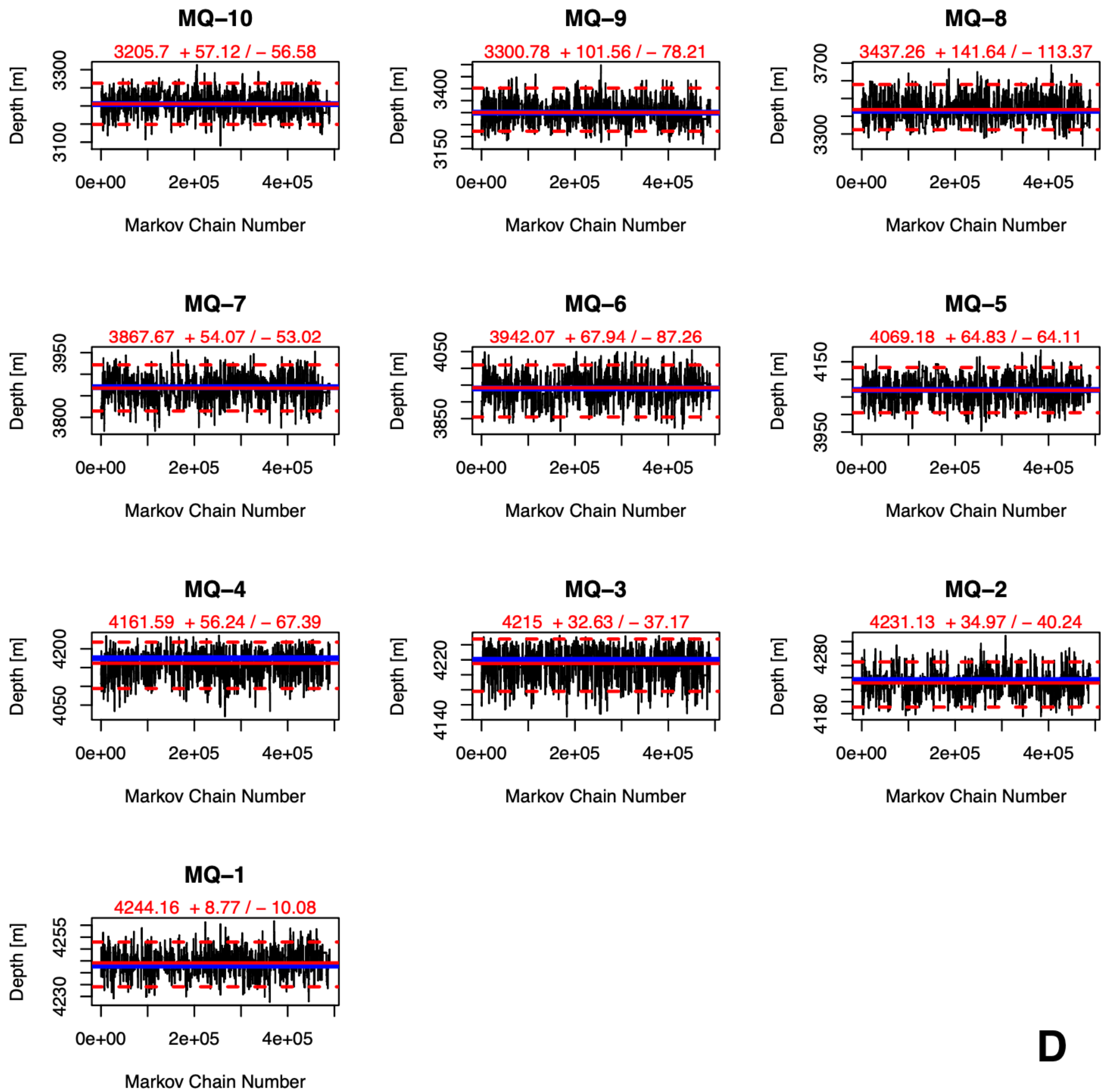

Figure 2.5 | Histograms and Chain Plots of Updated Age-Depths: Histograms and chain plots of the posterior distributions of our correlated age-depths after being updated under geological constraints. The solid red line indicates the median value of the updated parameter, while the dashed lines bracket the 95% credibility interval. The solid blue line indicates the mean of the original correlation to highlight any updated changes. The updated ages and depths are also listed along with their 95% HPDI uncertainties at the top of each subplot. A: Histograms of updated ages. B: Histograms of updated stratigraphic depths. C: Chain plots of updated ages. D: Chain plots of updated stratigraphic depths.

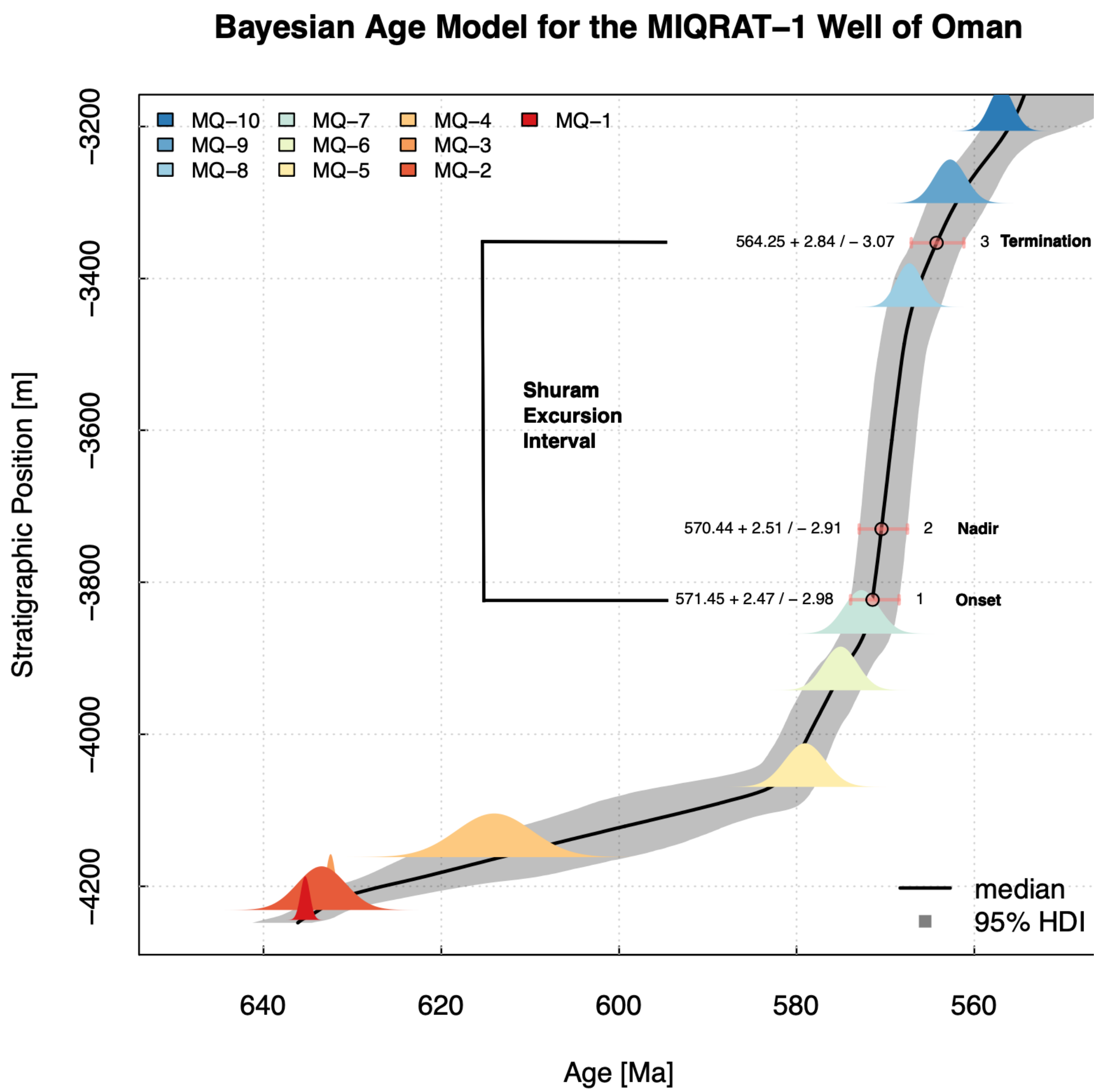

Figure 2.6 | Bayesian Age Model for the MIQRAT-1 Well of Oman: An age model of the Nafun Group based on the MIQRAT-1 Well of Oman. This model was generated using *Modified BChron* and allows for model age extractions for all depths between dated horizons. Stratigraphic positions are listed here as negative values as they correspond to the stratigraphic height starting at the base of the reference section. The coloured probability distributions correspond to the likelihood distributions of each specified age, with its height being scaled down to half its original value. The black line indicates the median value of the posterior model age and the gray shading represents the 95% credibility interval. The three listed data points and associated model ages correspond to the onset, nadir, and termination of the Shuram Excursion.

2.3.2 Bayesian Subsidence Model

Using the extracted model ages of the lithological boundaries of the Nafun Group stratigraphy within the MIQRAT-1 well, we corrected our reference section by accounting for porosity loss during sediment burial and compaction. We also applied the backstripping procedure of Sclater and Christie (1980) to remove the effects of sediment loading and paleobathymetry. The results of this subsidence analysis are shown in *Figure 2.7*, with the red data points corresponding to the total accommodation space generated by sediment-loaded subsidence (taking into account the effects of sediment compaction) and the blue data points representing the backstripped tectonic subsidence, the primary source of accommodation space production within the basin. As shown in this figure, the early stages of Nafun Group deposition consisted of a logarithmically decreasing rate of subsidence (concave-up curve) lasting between ca. 635-580 Ma. This segment is interpreted to have been caused by thermal subsidence following lithospheric stretching that resulted in the deposition of the Abu Mahara Group. This is followed by a significant increase in subsidence rates (represented by the convex-up shape of the curve), which we interpret as the basin's transition into a foreland basin where lithospheric flexure takes over as the dominant mechanism of subsidence.

In order to extract more insight on the parameters controlling subsidence within this basin, we also fit a thermal subsidence curve through our subsidence profile using Bayesian regression. One of the main challenges to applying this approach is that our profile consists of multiple subsidence mechanisms, such that data points corresponding to the thermal subsidence phase needs to be isolated from the other data points to produce the most representative model fit. In the case of our profile, the exact transition point into flexural subsidence is not perfectly clear, which is why we produced multiple thermal subsidence curves corresponding to a different

Lithological Boundary:	Stratigraphic Depth (m):	Model Age (Ma):
Buah-Ara Boundary	3200	556.03 +2.92/-7.35
Buah Limestone-Dolostone Boundary	3427	566.71 +2.91/-3.19
Shuram-Buah Boundary	3450	567.25 +2.79/-3.03
Shuram Limestone	3508	568.17 +2.74/-2.59
Shuram Shale-Limestone Boundary	3570	568.83 +2.73/-2.60
Shuram Shale Interbeds	3660	569.74 +2.61/-2.75
Khufai-Shuram Boundary	3800	571.18 +2.46/-2.98
Khufai Shale-Dolostone Boundary	3861	572.15 +2.63/-3.02
Khufai Dolostone-Shale Boundary	3878	572.77 +2.76/-3.11
Khufai Limestone-Dolostone Boundary	3910	574.46 +3.12/-2.99
Khufai Dolostone-Limestone Boundary	4060	581.77 +9.25/-4.21
Khufai Shale-Dolostone Boundary	4091	588.75 +14.42/-9.31
Khufai Dolostone-Shale Boundary	4105	593.60 +13.17/-10.66
Masirah Bay-Khufai Boundary	4128	601.77 +12.43/-12.48
Hadash-Masirah Bay Boundary	4238	634.75 +3.45/-3.26
Abu-Mahara-Hadash Boundary	4243	635.55 +4.21/-3.13

Table 2.4 | Model Ages of Lithological Boundaries within the MIQRAT-1 Well: The extracted model ages of the lithological boundaries of the Nafun Group stratigraphy within the MIQRAT-1 well. The model ages are listed as a median value along with their 95% HPDI uncertainty.

number of data points used in our model fit for comparison. *Figure 2.8* summarizes these results, while the reasoning for data point selections are described below.

We generated four thermal subsidence curves using *n* number of data points to fit our model. Here, each data point index refers to the age-depth combination from our subsidence profile starting at a depth of zero. For example, *n=3* indicates a subsidence curve fit based on the 3 data points starting at *age = ca. 635 Ma* and ending at *age = ca. 602 Ma*. The four model curves were generated using *n=3, 4, 5, and 6*, with these data points interpreted as the possible temporal range for thermal subsidence within the basin. This cut off is inferred from the sharp increase in accommodation space production that occurs directly after the 6th data point, suggesting a transition in subsidence mechanics. In addition, under the scenario of flexural subsidence, it is common for subsidence rates to decrease significantly (possibly even to negative values) just prior to sharp increase in subsidence rates due to uplift caused by the arrival of the flexural forebulge (Allen and Allen, 2013). Here, the flattening of the subsidence curve between *n=3* and *n=6* suggests that the transition point occurred within this interval.

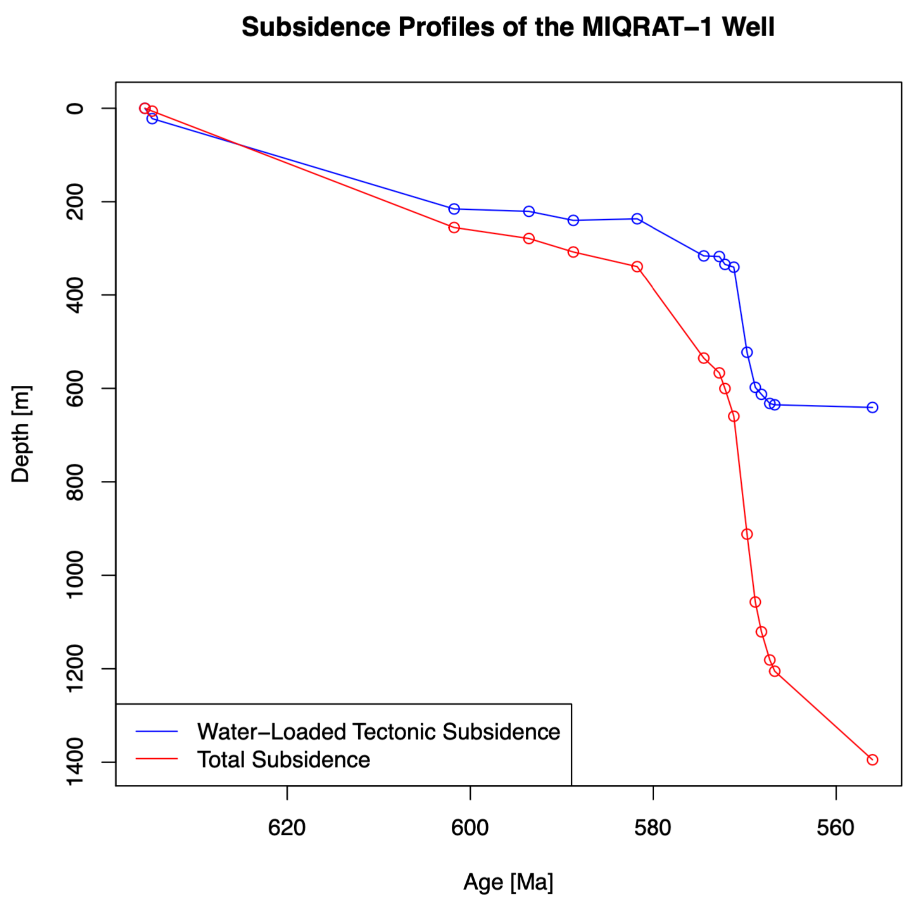

Figure 2.7 | Subsidence Profiles of the MIQRAT-1 Well: Subsidence curves for the Nafun Group in the MIQRAT-1 well. The total subsidence (red curve) refers to the decompacted depth to basement, while the water-loaded subsidence (blue curve) assumes 1D airy isostasy and accounts for paleowater depth.

As shown from the thermal subsidence curves from *Figure 2.8*, the uncertainty range decreases with increasing n and the median of the curve tends towards values of lower lithospheric stretching (i.e. a lower β value). Given that the $n=5$ and $n=6$ curves approach our minimum β constraint (1.12; Armitage and Allen, 2010) and have 95% credibility intervals that do not encompass the uncertainty range of the lithological boundary ages, we consider these model configurations as less representative of our subsidence profile. In contrast, the model configurations with $n=3$ and $n=4$ have wider credibility intervals that better encapsulate the total uncertainty of our model fit (i.e. boundary ages, water depth corrections, natural spread of the data, etc.). Because the exact timing of the onset of flexural subsidence between the $n=3$ and $n=4$ configurations is ambiguous, we based subsequent inferences on a composite of the two configurations. Importantly, this approach defines a more representative range for this tectonic transition, where the initial inflection to slower subsidence rates (i.e. at $n=3$) is treated as the earliest possible onset age, while the inflection to negative subsidence rates (i.e. at $n=5$) is treated as the latest point for this transition. We do not base the youngest onset age on the inflection to higher subsidence rates (i.e. at $n=6$) because this point lies outside the credibility interval of all of our model configurations. Instead, we interpret this outlier from the thermal subsidence trajectory to reflect uplift caused by the arrival of the migrating flexural forebulge, indicating the basin's full transition into a foreland basin.

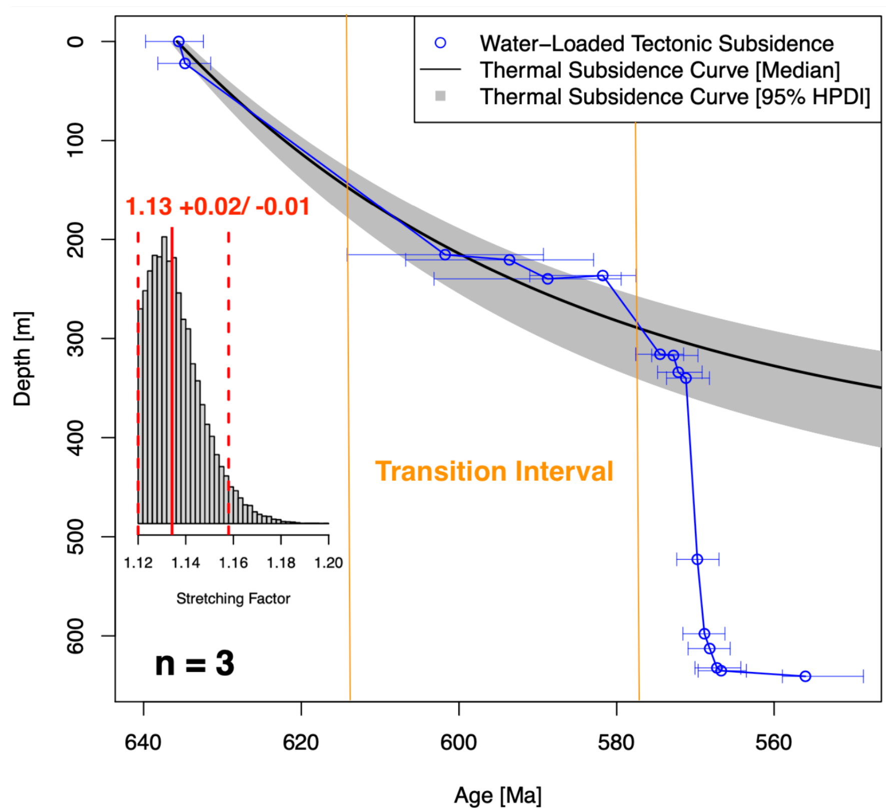
Water–Loaded Tectonic Subsidence
Thermal Subsidence Curve [Median]
Thermal Subsidence Curve [95% HPDI]
1.13 +0.02/ -0.01
Stretching Factor
Transition Interval
n = 3
Depth [m]
Age [Ma]

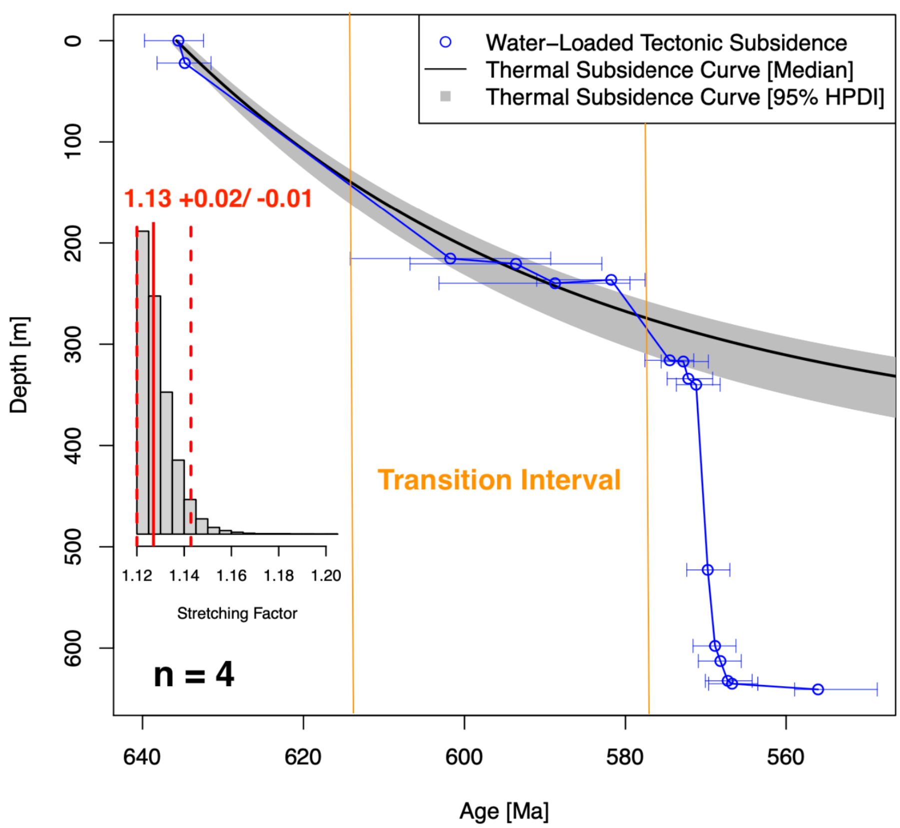
Water–Loaded Tectonic Subsidence
Thermal Subsidence Curve [Median]
Thermal Subsidence Curve [95% HPDI]
1.13 +0.02/ -0.01
Stretching Factor
Transition Interval
n = 4
Depth [m]
Age [Ma]

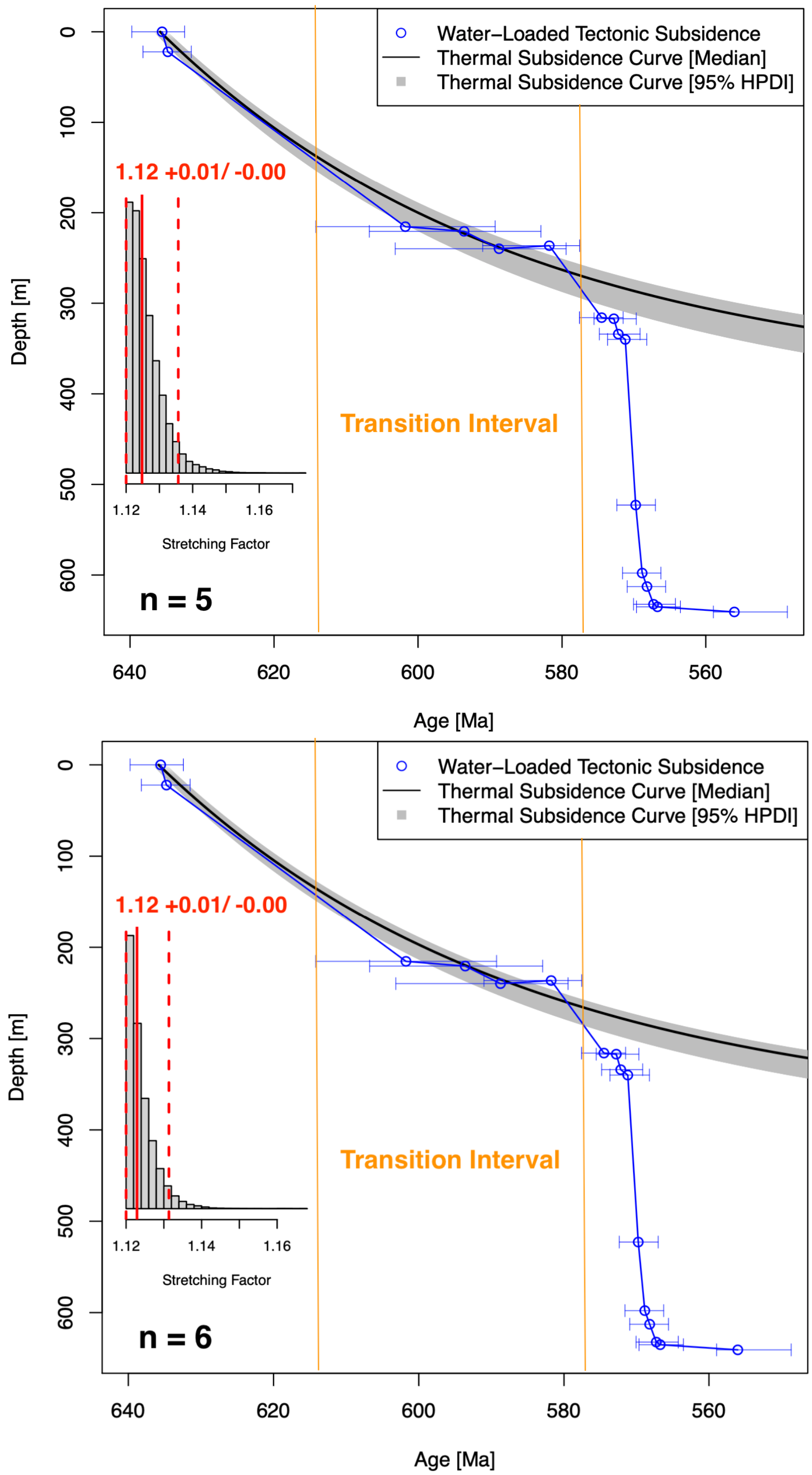

Figure 2.8 | Thermal Subsidence Curves for the MIQRAT-1 Well of Oman: Thermal subsidence curves fitted to the backstripped subsidence profile of the MIQRAT-1 well using a varying amount of data points for the model fit. The error bars shown here correspond to the age uncertainty of the lithological boundaries. The corresponding β values for each curve are shown in red along with their posterior distributions.

Our estimate of the subsidence transition range for the MIQRAT-1 well is based on the intercepts between our composite thermal subsidence curve and the inflection points described above. The first intercept, corresponding to the oldest onset age, yields a result of 598.14 +8.35/-5.85 Ma, while the second intercept, corresponding to the youngest onset age, yields an age of 591.35 +10.21/-7.25 Ma. Taken together, these results indicate the subsidence transition occurred between ca. 606.49 Ma and 584.10 Ma (*Figure 2.10*). The posterior distribution and chain plots of the model parameters used in generating this composite curve are shown in *Figure 2.9*, while their values and descriptions are summarized in *Table 2.5*.

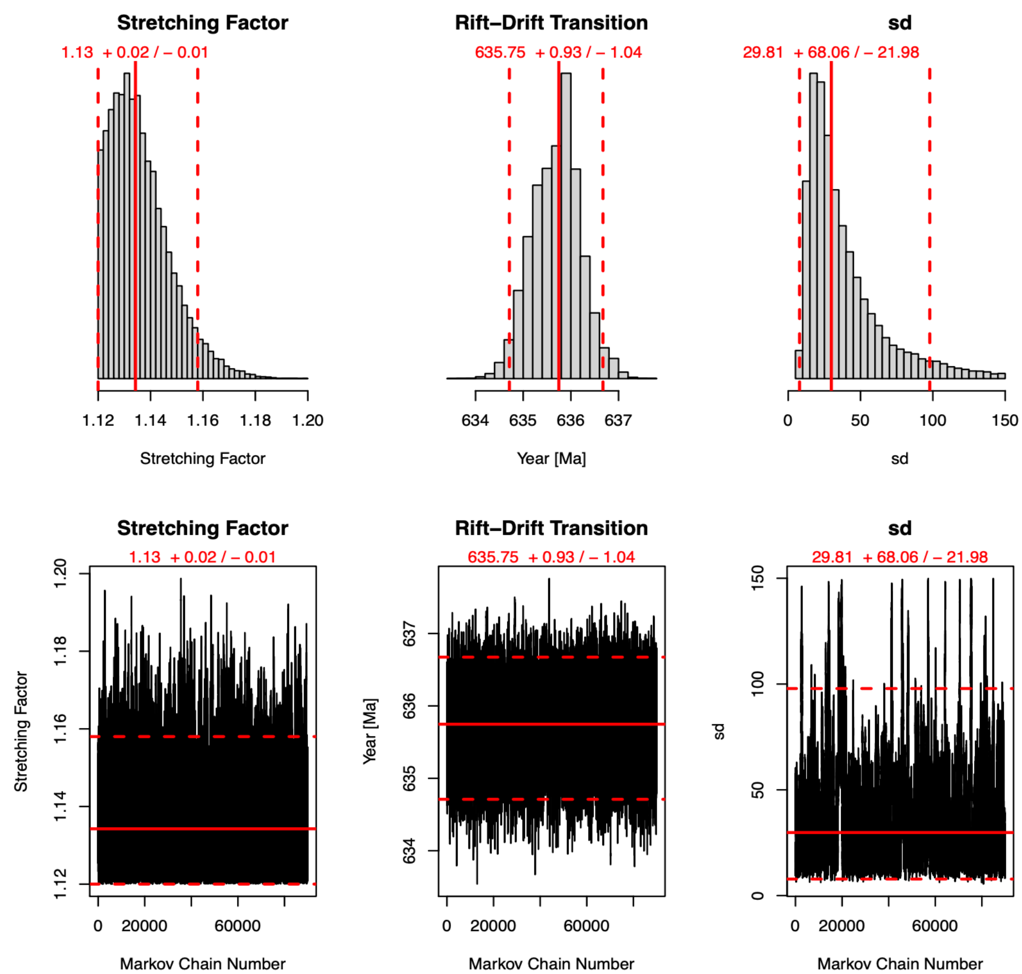

Figure 2.9 | Posterior Distribution of Thermal Subsidence Model Parameters: Histograms and Markov chain plots showing the posterior distribution of model parameters used in our thermal subsidence model. The solid red line indicates the median value and the dashed lines indicate the 95% HPDI interval.

2.4 Discussion

2.4.1 Model Parameters and their Implications

Previous studies focused on reconstructing the Ediacaran tectonic history of Oman have invoked thermal subsidence as the driving mechanism for accommodation space production for the Nafun Group (Allen, 2007, Le Guerroué et al., 2006b). This inference has generally been based on geological and seismic observations that indicate a transition from the confined horst-graben style deposition of the Cryogenian Abu Mahara Group followed by more widespread, sheet-like deposition of the Nafun Group (Allen, 2007). For this reason, the rift-drift transition has been placed at the base of the Hadash Fm. with an age assumed to be equivalent to the Marinoan cap-dolostones. This age was estimated as 635.26 ± 1.07 Ma based on a correlation with a U-Pb zircon age obtained from the base of the Doushantuo Fm. in South China (Condon et al., 2005). Here, we have included the age of the rift-drift transition as one of the model parameters used in our Bayesian-fitted thermal subsidence curve. While it is theoretically possible to include the stratigraphic depth of the rift-drift transition as a model parameter as well, we have decided to leave this term fixed at the base of the Hadash Fm because the Hadash Fm. in the MIQRAT-1 well is ~5 m. Consequently, uncertainty in the stratigraphic position of the rift-drift transition would be limited to below the uncertainty from the natural spread of data. Since this uncertainty is already incorporated into our model curve, and because the tight correlation between these terms tend to destabilize our model outputs, we chose to focus instead on constraining the exact timing of the rift-drift transition rather than its precise placement within the Hadash Fm. The result is a model age for the rift-drift transition of 635.75 +0.93/-1.04 Ma placed at the base of the Nafun Group. This estimate also applies to the age of the contact between Cryogenian and Ediacaran strata in Oman.

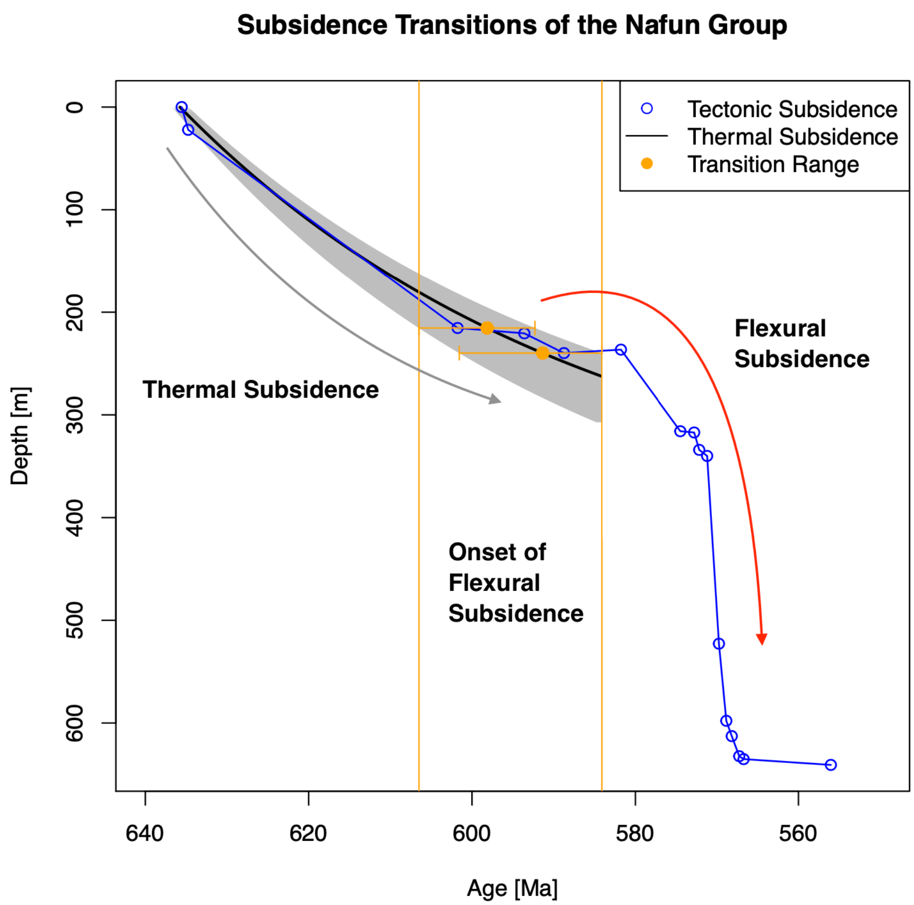

Figure 2.10 | Subsidence Transitions of the Nafun Group: A thermal subsidence curve fitted to a backstripped tectonic subsidence profile using a composite of *n=3* and *n=4* data points. The orange points correspond to the intercept between the thermal subsidence curve and inflection points interpreted as the minimum and maximum onset ages of the basin's transition into a foreland basin. The region between the vertical orange lines is interpreted as the transition range where flexural subsidence has initiated but is occurring under the backdrop of thermal subsidence, while the regions to either side of the orange lines correspond to time intervals dominated by a single subsidence mechanism. These mechanisms are indicated by a gray and red arrow, which correspond to the typical signature (i.e. curve shape) of thermal and flexural subsidence profiles respectively.

The stretching factor was also estimated from our subsidence analysis, which yielded a β value of 1.13 +0.02/-0.01 and indicates minimal extension and low subsequent rates of accommodation space production. Such low β values are generally associated with subsidence generated in cratonic and continental rim basins (Allen, 2007; Allen and Allen, 2013; Armitage and Allen, 2010), suggesting that the Oman basin was situated over modestly stretched continental lithosphere with its center at least several hundreds of kms inland from the continental margin (Allen and Allen, 2013). The post-extensional subsidence itself was likely generated from the thermal relaxation of upwelled mantle material that may have relayed laterally from an adjacent passive margin (Allen, 2007). Consequently, continental stretching during Abu Mahara times was limited, with the early stages of Nafun Group deposition possibly occurring contemporaneously with the drift phase of an adjacent passive margin. Importantly, only the early stages of Nafun Group deposition are consistent with this mechanism given that our subsidence modelling results suggest a drastic shift in tectonic environments by ca. 606.49 Ma (*Figure 2.10*). This result contrasts with the previous estimates of the stretching factor in Oman, which yield β values between 1.19 and 1.81 (Le Guerroué et al., 2006b).

Parameter:	**Value:**	**Description:**
Stretching Factor (β)	1.13 +0.02/-0.01	The ratio of the thickness of the lithosphere before being stretched to its thickness after being stretched.
Rift-Drift Transition	635.75 +0.93/-1.04 Ma	The age marking the transition from the structurally-confined rift-driven sedimentation of the Abu Mahara Group to the unconfined extensive sedimentation of the Nafun Group.
sd	29.81 +68.06/-21.98 m	The standard deviation of the model fit. This value describes the natural or random spread of data away from the model curve.

Table 2.5 | Model Parameters of the Thermal Subsidence Curve: The median and 95% credibility interval of the posterior model parameters used for generating the thermal subsidence curve.

As shown in *Figure 2.10*, our subsidence analysis of the MIQRAT-1 well suggests a major increase in net accumulation rates at ca. 591.35 +10.21/-7.25 Ma. Barring a major eustatic rise in sea level at this time, this increase in rate of base level rise can only be interpreted in terms of subsidence because depositional facies both above and below are relatively shallow water. In other words, an increase in sedimentation rates alone cannot account for the increase in accumulation rates. We interpret this inflection to be the transition from a thermal subsidence phase to a flexural phase in the basin driven by tectonic loading. Following from this interpretation, the initial flattening of the subsidence curve is interpreted as the earliest onset age of transition, where the Oman basin, which was evidently distant from the tectonic load, experienced modest initial uplift, counteracting thermal subsidence. The basin apparently transitioned into a foredeep by ca. 584.10 Ma, when sediment accumulation rates increase significantly.

2.4.2 Paleotectonic Implications of Foreland Basin Development in Oman

In addition to climatic and bio-evolutionary changes occurring during the Ediacaran Period, this interval also bore witness to large-scale paleogeographic changes related to the closure of ocean basins during the amalgamation of the supercontinent Gondwana (Collins et al., 2007; Collins and Pisarevsky, 2005; Johnson et al., 2011; Tohver et al., 2006). Among these tectonic events was the collision between Neoproterozoic India and the Congo-Tanzania-Bangweulu Block which culminated with the closure of the Mozambique Ocean (Collins et al., 2007; Cox et al., 2012) and the final suturing between East and West Gondwana (*Figure 2.11*). While it is generally accepted that the closure of the Mozambique Ocean occurred during the late-Ediacaran to early-Cambrian (Collins and Pisarevsky, 2005), the exact timing and geographic position of its suture and its relations to the assembly of the Arabian-Nubian Shield (ANS) remains a topic of debate. Allen (2007) argued that the ANS was fully assembled by ca. 650 Ma with Oman possibly accreted along the Ar-Rayn terrane to the eastern extent of the shield. Under this scenario, Oman would have occupied a passive continental margin during

Nafun times before transitioning into a retro-arc setting as oceanic crust subducted beneath the former passive margin during Ara times (Allen, 2007). The final closure of the Mozambique Ocean would then have occurred at ca. 540 Ma during the formation of the Malagasy Orogeny (Collins and Pisarevsky, 2005) with its suture lying within the exposed eastern periphery of the ANS (Allen, 2007; Stern, 1994). In contrast, Cox et al. (2012) argued, based on age constraints obtained from the Ad Dawadimi terrane of eastern Saudi Arabia, that Oman was not contiguous with the ANS in the early Ediacaran and that the eastern extent of the ANS remained an active margin until at least ca. 620 Ma. Indeed, geochronological evidence suggests ongoing tectonism and arc magmatism in this part of the ANS through at least ca. 590 Ma (Nettle et al., 2014; Robinson et al., 2017). Consequently, Oman and the ANS would have remained separated by the latest vestige of the Mozambique Ocean, with Oman situated on the leading margin of Neoproterozoic India. The suture marking the closure of the Mozambique Ocean would then lie west of the currently exposed ANS, below Phanerozoic cover in eastern Saudi Arabia (Cox et al., 2012). This suture, which has also been inferred from the presence a significant magnetic anomaly (Stern and Johnson, 2010), would mark the northernmost and final collisional event of the East African Orogeny (EAO; Stern, 1994; Nettle et al., 2014).

In addition to the age constraints that suggest a < 620 Ma assembly for the ANS, lithological differences between the Nafun Group of Oman and the Jibalah Group of Saudi Arabia hint at their separation during Nafun times. In particular, no magmatism occurs at this time in Oman, while volcanic strata within the Jibalah Group stratigraphy suggests extensive magmatism on the Arabian Shield (Kusky and Matsah, 2003; Johnson et al., 2013; Robinson et al., 2014; Shen et al., in press). Moreover, the Jibalah Group was likely deposited in a series of pull-apart basins (known collectively as the Jibalah basins; Johnson et al., 2013; Nettle et al., 2014), highlighting another difference between the extensive sheet-like stratigraphy of the Nafun Group and the restricted depositional-style of the Jibalah Group.

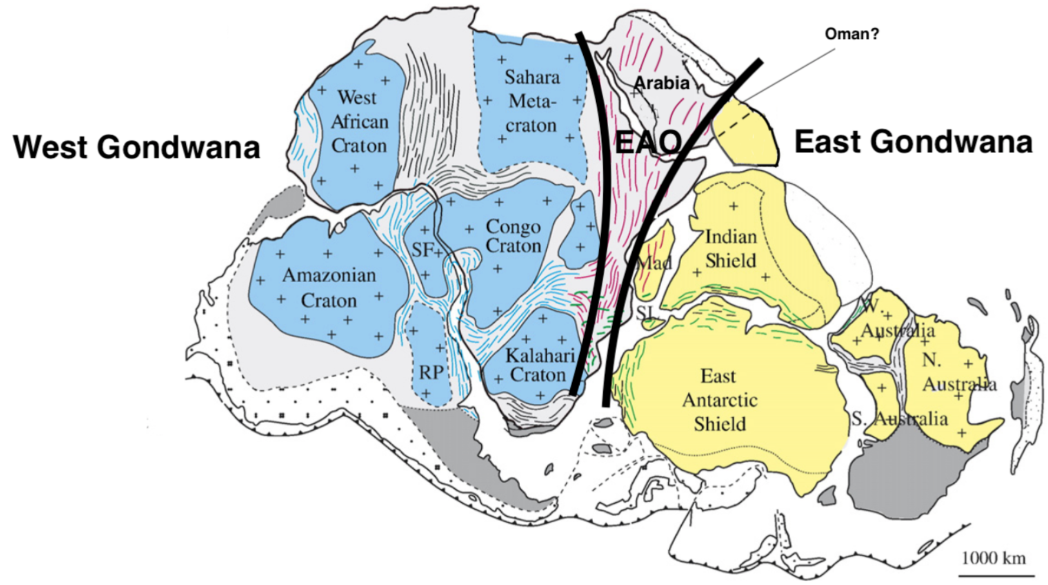

Figure 2.11 | Gondwana Assembly: A simplified cartoon illustrating the final collision between East and West Gondwana. West Gondwana is shaded in blue and East Gondwana is shaded in yellow. The East African Orogeny (EAO) extends northwards into the Arabian Shield and marks the final closure of the Mozambique Ocean. The hypothesized geographic position of Oman is also shown, potentially situated inboard from the leading margin of Neoproterozoic India in East Gondwana. *Modified from Meert and Lieberman (2008)*

The Jibalah basins occur along a series of northwest trending transpressional faults known as the Najd Fault System (NFS) and are believed to record tectonic escape during the final stages of the EAO (Johnson et al., 2013). Evidence for this tectonism is found in minor folding and seismic structures throughout the Jibalah Group and along its basin-bounding faults throughout the Arabian Shield (Al-Husseini, 2015; Johnson et al., 2013; Nettle et al., 2014). Given that suites of granitoid rocks indicative of post-accretionary processes are also present across multiple Jibalah basins, Robinson et al. (2014) associated the activation of the NFS and the subsequent formation of pull-apart basins with a series of accretionary events potentially corresponding to the subduction of the Mozambique Ocean and the amalgamation of Gondwana.

Indeed, the base of the Jibalah Group is constrained by an age of ca. 618 Ma (Nettle et al., 2014), implying that the ANS had yet to fully assemble by this time.

As indicated in *Figure 2.10*, our modelling results suggest that the Oman basin transitioned from a thermally subsiding basin into a flexural basin sometime between ca. 606.49 Ma and 584.10 Ma. This timeframe is consistent with the hypothesis that Oman was not sutured to the ANS until the terminal stages of the EAO after 620 Ma. Correspondingly, the rapid increase in sedimentation accumulation observed in the Nafun Group likely reflects this collisional event following the reactivation of the NFS, and possibly marking the closure of the Mozambique Ocean. This scenario also implies that Oman was part of the Indian continent (*Figure 2.11*; Cox et al., 2012), probably inboard from the leading margin to account for the low rates of thermal subsidence prior to collision. Consequently, its distance from the tectonic load was likely sufficient that the basin experienced uplift due to the arrival of the migrating flexural forebulge, which may be expressed by the unconformity at the Khufai-Shuram boundary. The subsequent termination of flexural subsidence and shift to extension-related magmatism during Ara times may then reflect a stage of post-orogenic collapse, as occurred on the ANS at this time (Robinson et al., 2017). This tectonic model predicts that the actual passive margin sequence on the leading margin of the Indian plate lies buried beneath the Rub Al-Khali desert of the eastern Arabian Shield.

2.4.3 Age and Duration of the Shuram Excursion and its Implications

Based on our "fine-tuning" of correlated age-depths and corresponding Bayesian age model for the MIQRAT-1 well of Oman, the onset, nadir and termination age of the Shuram Excursion (SE) are 571.45 +2.47/-2.98 Ma, 570.44 +2.51/-2.91 Ma, and 564.25 +2.84/-3.07 Ma, respectively, where the onset is defined as the point at which declining $\delta^{13}C$ values cross 0‰, and the end corresponding to where increasing values again cross 0‰. Applying the posterior output of our age model, the duration for the SE is 7.20 +0.37/-0.09 Myrs. The uncertainty on the duration is much narrower than for the individual ages because in the posterior distributions, the ages for the onset, nadir, and end of the SE are all linked. For example, when the onset of the SE is older than the median in a given posterior sample, the nadir and end of SE will generally be older as well (e.g. Halverson et al., 2022).

The estimate for the duration of the SE is dramatically shorter than the 50 Myr estimate of Le Guerroue et al. (2006b) based on subsidence analysis in the same region. The reason for this difference is that Le Guerroue et al. (2006b) assumed that thermal subsidence generated accommodation space for the entirety of the Nafun Group, which at the time was consistent with the limited available geochronological constraints. However, the application of a new age model for the Nafun Group to a subsidence analysis of the MIQRAT-1 well (*Figure 2.10*) clearly indicates the underlying assumptions of the original analysis were incorrect. Our analysis reveals an inflection in sediment accumulation that occurred just prior to the onset of the SE in Oman, which accounts for the much shorter duration estimate (*Figure 2.12*).

Our results for the duration of the SE are surprisingly similar to estimates generated by different approaches. For example, Gong and Li (2020) applied an astrochronological analysis to gamma ray data from the MIQRAT-1 well. Based on the identification of what they interpreted to be the 405 kyr long eccentricity cycle, they estimated a 7.7 ± 0.2 Myr duration for the SE, which overlaps our own estimate of 7.20 +0.37/-0.09 Myrs. Our result is also broadly consistent with duration estimates obtained from the Johnnie Fm. in southern Nevada (6 Myrs by Witkosky and Wernicke, 2018; 8.2 ± 1.2 Myrs by Minguez et al., 2015), the Wonoka Fm. in South

Australia (8.0 ± 0.5 Myrs; Minguez and Kodama, 2017), and the Doushantuo Fm. in South China (9.1 ± 1.0 Myrs; Gong et al., 2017). Furthermore, our age model suggests that the nadir of the SE was reached within 1.01 +0.04/-0.07 Myrs of the start of the excursion, similar to the 1.2 Myr estimate of Gong and Li (2020) and the 1.0 Myr estimate of Minguez and Kodama (2017). Given the consistency of duration estimates stemming from a wide variety of modelling approaches across a wide range of sedimentary settings globally, it is evident that that the SE records a global and synchronous event rather than being purely an expression of local diagenetic processes.

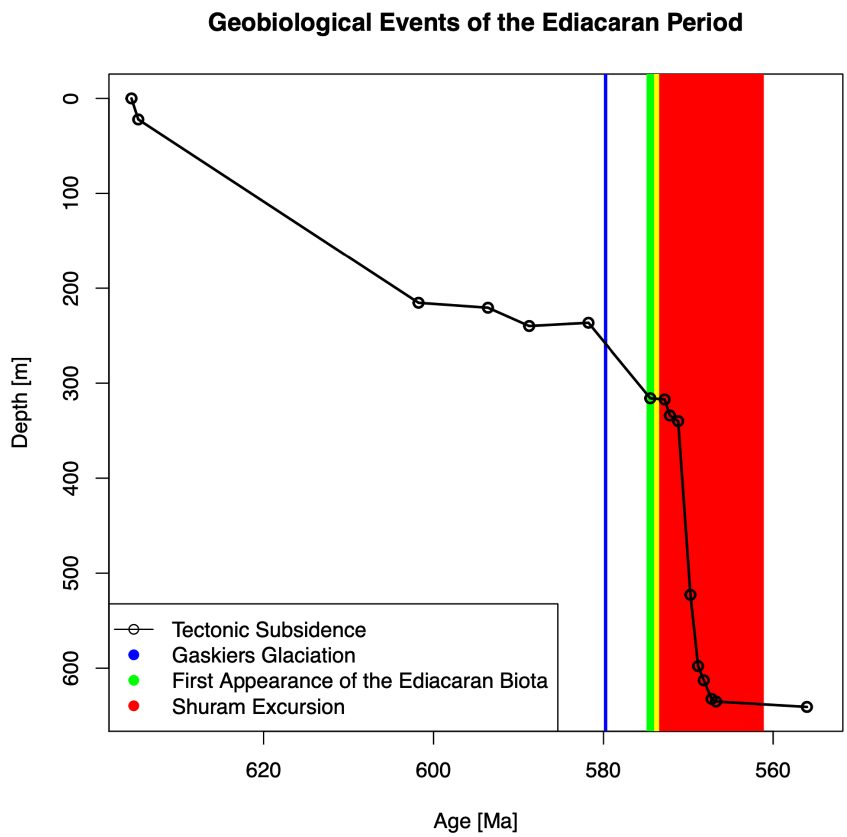

Figure 2.12 | Geobiological Events of the Ediacaran Period: The subsidence profile of the MIQRAT-1 well overlain by the time intervals of important geobiological events during the Ediacaran Period. The interval of the Gaskiers Glaciation (Pu et al., 2016) is shown in blue. The interval shaded in green represents the 2σ uncertainty range of the first appearance of the Ediacaran biota (Matthews et al., 2021), while the shaded red region represents the SE interval estimated from our Bayesian age model. The yellow region represents a potential temporal overlap between these two events. All of these events occur after the onset of flexural subsidence in the Oman basin.

Our model onset age of 571.45 +2.47/-2.98 Ma also has implications for Ediacaran chronology more broadly and the potential interconnection of different middle Ediacaran geobiological events (*Figure 2.12*). For example, Halverson et al. (2005) suggested the SE was mechanistically linked to the Gaskiers glacial event, now dated to ca. 579.78-579.44 Ma (Pu et al., 2016). However, our model results indicate that the SE occurred at least 5.5 Myrs after the terminal Gaskiers deglaciation, ruling out any direct linkage between the two events. Our age model also suggests that the onset of the SE occurred slightly after, or even concurrently with (taking into account uncertainty), the first appearance of the Ediacaran macrobiota at ca. 575 Ma (*Figure 2.12*; Matthews et al., 2021). This overlap between these two events hints that the SE may be a geochemical expression of the changing environmental or climatic conditions that allowed the early Avalon organisms to thrive and evolve.

While the exact causal mechanism of the SE remains unclear, our modelling results suggest a potential association between the amalgamation of Gondwana and geobiological events occurring in the mid-late Ediacaran. That is, assuming that the Oman basin's transition into a foreland basin heralds the closure of the Mozambique Ocean and subsequent collision between East and West Gondwana, it follows that the EAO may have influenced the Earth systems through enhanced nutrient delivery into the oceans and atmospheric oxygen production (Squire et al., 2006; Zhu et al., 2022). For example, it is estimated that the Trans-Gondwanan mountain chains extended over 8000 km and supplied over 100 km^3 of sediment through erosion (Squire et al., 2006). Such high sediment fluxes would have translated to proportionally high nutrient fluxes. It is therefore feasible that both the Gaskiers glaciation and proliferation of complex multicellular organisms were mediated by a surge in primary productivity and followed by high rates of organic carbon burial and oxygen accumulation in the atmosphere. In fact, the continued erosion of these supermountains may have provided the nutrients required to fuel the evolution of larger complex organisms (Squire et al., 2006; Zhu et al., 2022) and generate the excess oxidizing power driving the deep excursion of the SE. This hypothesis accounts for why the SE and emergence of the Ediacaran biota are so closely spaced in time. A potential redox barrier, likely in the form of a large reservoir of reduced carbon (Fike et al., 2006; Lee et al., 2015; Rothman et al., 2003), may have suppressed biological evolution in the mid-Ediacaran until this redox threshold was broken (Lee et al., 2015). By this reasoning, the SE marks this fundamental geochemical and redox transition. Therefore, if the interpretation that geobiological events in the Ediacaran are closely linked to the erosion of the Trans-Gondwanan supermountains is correct, it implies that the EAO may have been a major factor in shaping the Earth's surface environment during this dynamic interval in Earth history.

Conclusion:

Accurately constraining the age and duration of the SE is important for understanding its origin and potential association with broadly contemporaneous geobiological events during the Ediacaran Period. Through chemostratigraphic correlation and the use of Bayesian statistical techniques, we have developed an age model based on the Nafun Group stratigraphy in the MIQRAT-1 well of Oman. We estimate the onset, nadir, and termination of the SE to have occurred at 571.45 +2.47/-2.98 Ma, 570.44 +2.51/-2.91 Ma, and 564.25 +2.84/-3.07 Ma, respectively. The age model yields a posterior duration of 7.20 +0.37/-0.09 Myrs for the SE, which is similar to estimates obtained from the southern United States, South China, South Australia, and Oman based on different approaches, including astrochronology (Gong et al., 2017; Gong and Li, 2020; Minguez and Kodama, 2017; Minguez et al., 2015; Witkosky and

Wernicke, 2018). The consistency of these results suggests that the SE is primary in origin and records a globally synchronous event.

We have also developed a compaction-corrected tectonic subsidence model based on the same reference drill core in Oman. Here, modelling results indicate that accommodation space generation during the early Ediacaran was driven by thermal subsidence following limited lithospheric extension during the late-Cryogenian. Flexural subsidence then initiated between ca. 606.49 Ma and 584.10 Ma, which we interpret as recording the final suturing between Neoproterozoic India and the Arabian-Nubian Shield in the northernmost extent of the EAO. Given the close temporal proximity between supermountain chain development and major geobiological events during the Ediacaran, we suggest that the EAO may have played a major role in mediating these events through continued erosion and oxygenation of surface environments. The SE may thus be a geochemical marker of changing redox conditions that culminated with the evolution of the Ediacaran biota.

REFERENCES:

Al-Husseini, M. (2014). Proposed correlation of Oman's Abu Mahara Supergroup and Saudi Arabia's Jibalah Group. *Geoarabia*, *19*(2), 17-48. https://doi.org/10.2113/geoarabia190217

Al-Husseini, R. (2015). Spatio-temporal position of the Ediacaran Thalbah Basin in the Najd Fault System, Arabian Shield. *Geoarabia*, *20*(1), 17-44. https://doi.org/10.2113/geoarabia200117

Al-Siyabi, H. (2005). Exploration history of the Ara intrasalt carbonate stringers in the South Oman Salt Basin. *Geoarabia*, *10*(4), 39-72. https://doi.org/10.2113/geoarabia100439

Allan, J., & Matthews, R. (1982). Isotope signatures associated with early meteoric diagenesis. *Sedimentology*, *29*(6), 797-817. https://doi.org/10.1111/j.1365-3091.1982.tb00085.x

Allen, P. (2007). The Huqf Supergroup of Oman: Basin development and context for Neoproterozoic glaciation. *Earth-Science Reviews*, *84*(3-4), 139-185. https://doi.org/10.1016/j.earscirev.2007.06.005

Allen, P., & Allen, J. (2013). *Basin Analysis: Principles and Application to Petroleum Play Assessment, 3r*. John Wiley & Sons.

Allen, P., & Leather, J. (2006). Post-Marinoan marine siliciclastic sedimentation: The Masirah Bay Formation, Neoproterozoic Huqf Supergroup of Oman. *Precambrian Research*, *144*(3-4), 167-198. https://doi.org/10.1016/j.precamres.2005.10.006

Allen, P., Leather, J., & Brasier, M. (2004). The Neoproterozoic Fiq glaciation and its aftermath, Huqf supergroup of Oman. *Basin Research*, *16*(4), 507-534. https://doi.org/10.1111/j.1365-2117.2004.00249.x

Allen, P., Leather, J., Brasier, M., Rieu, R., McCarron, M., & Guerroué, E. et al. (2011). Chapter 20 The Abu Mahara Group (Ghubrah and Fiq formations), Jabal Akhdar, Oman. *Geological Society, London, Memoirs*, *36*(1), 251-262. https://doi.org/10.1144/m36.20

Amthor, J., Grotzinger, J., Schröder, S., Bowring, S., Ramezani, J., Martin, M., & Matter, A. (2003). Extinction of Cloudina and Namacalathus at the Precambrian-Cambrian boundary in Oman. *Geology*, *31*(5), 431. https://doi.org/10.1130/0091-7613(2003)031<0431:eocana>2.0.co;2

Amthor, J., Ramseyer, K., Faulkner, T., & Lucas, P. (2005). Stratigraphy and sedimentology of a chert reservoir at the Precambrian-Cambrian Boundary: the Al Shomou Silicilyte, South Oman Salt Basin. *Geoarabia*, *10*(2), 89-122. https://doi.org/10.2113/geoarabia100289

An, Z., Jiang, G., Tong, J., Tian, L., Ye, Q., Song, H., & Song, H. (2015). Stratigraphic position of the Ediacaran Miaohe biota and its constrains on the age of the upper Doushantuo δ 13 C anomaly in the Yangtze Gorges area, South China. *Precambrian Research*, *271*, 243-253. https://doi.org/10.1016/j.precamres.2015.10.007

Armitage, J., & Allen, P. (2010). Cratonic basins and the long-term subsidence history of continental interiors. *Journal Of The Geological Society*, *167*(1), 61-70. https://doi.org/10.1144/0016-76492009-108

Bergmann, Kristin Diane (2013) *Constraints on the Carbon Cycle and Climate During the Early Evolution of Animals.* Dissertation (Ph.D.), California Institute of Technology. doi:10.7907/KFJX-7S28.

Bjerrum, C., & Canfield, D. (2011). Towards a quantitative understanding of the late Neoproterozoic carbon cycle. *Proceedings Of The National Academy Of Sciences*, *108*(14), 5542-5547. https://doi.org/10.1073/pnas.1101755108

Blaauw, M., & Heegaard, E. (2012). Estimation of age-depth relationships. *Developments in Paleoenvironmental Research, 5*, 379-413. http://dx.doi.org/10.1007/978-94-007-2745-8_12

Bobrovskiy, I., Hope, J., Ivantsov, A., Nettersheim, B., Hallmann, C., & Brocks, J. (2018). Ancient steroids establish the Ediacaran fossil Dickinsonia as one of the earliest animals. *Science*, *361*(6408), 1246-1249. https://doi.org/10.1126/science.aat7228

Boggiani, P., Gaucher, C., Sial, A., Babinski, M., Simon, C., & Riccomini, C. et al. (2010). Chemostratigraphy of the Tamengo Formation (Corumbá Group, Brazil): A contribution to the calibration of the Ediacaran carbon-isotope curve. *Precambrian Research*, *182*(4), 382-401. https://doi.org/10.1016/j.precamres.2010.06.003

Bowring, S., Grotzinger, J., Condon, D., Ramezani, J., Newall, M., & Allen, P. (2007). Geochronologic constraints on the chronostratigraphic framework of the Neoproterozoic Huqf Supergroup, Sultanate of Oman. *American Journal Of Science*, *307*(10), 1097-1145. https://doi.org/10.2475/10.2007.01

Bristow, T., & Kennedy, M. (2008). Carbon isotope excursions and the oxidant budget of the Ediacaran atmosphere and ocean. *Geology*, *36*(11), 863. https://doi.org/10.1130/g24968a.1

Bronk Ramsey, C. (2008). Deposition models for chronological records. *Quaternary Science Reviews*, *27*(1-2), 42-60. https://doi.org/10.1016/j.quascirev.2007.01.019

Brooks, S., Gelman, A., Jones, G., & Meng, X. (2011). *Handbook of Markov Chain Monte Carlo* (1st ed., p. 619). Chapman and Hall/CRC. https://doi.org/10.1201/b10905

Burns, S. J., & Matter, A. (1993). Carbon isotopic record of the latest Proterozoic from Oman. *Eclogae Geologicae Helvetiae, 86*(2), 595-607.

Bykova, N., Gill, B., Grazhdankin, D., Rogov, V., & Xiao, S. (2017). A geochemical study of the Ediacaran discoidal fossil Aspidella preserved in limestones: Implications for its taphonomy and paleoecology. *Geobiology*, *15*(4), 572-587. https://doi.org/10.1111/gbi.12240

Calver, C. (2000). Isotope stratigraphy of the Ediacarian (Neoproterozoic III) of the Adelaide Rift Complex, Australia, and the overprint of water column stratification. *Precambrian Research*, *100*(1-3), 121-150. https://doi.org/10.1016/s0301-9268(99)00072-8

Calver, C., Crowley, J., Wingate, M., Evans, D., Raub, T., & Schmitz, M. (2013). Globally synchronous Marinoan deglaciation indicated by U-Pb geochronology of the Cottons Breccia, Tasmania, Australia. *Geology*, *41*(10), 1127-1130. https://doi.org/10.1130/g34568.1

Campbell, I., & Squire, R. (2010). The mountains that triggered the Late Neoproterozoic increase in oxygen: The Second Great Oxidation Event. *Geochimica Et Cosmochimica Acta*, *74*(15), 4187-4206. https://doi.org/10.1016/j.gca.2010.04.064

Canfield, D., Knoll, A., Poulton, S., Narbonne, G., & Dunning, G. (2020). Carbon isotopes in clastic rocks and the Neoproterozoic carbon cycle. *American Journal Of Science*, *320*(2), 97-124. https://doi.org/10.2475/02.2020.01

Cao, M., Daines, S., Lenton, T., Cui, H., Algeo, T., & Dahl, T. et al. (2020). Comparison of Ediacaran platform and slope δ238U records in South China: Implications for global-ocean oxygenation and the origin of the Shuram Excursion. *Geochimica Et Cosmochimica Acta*, *287*, 111-124. https://doi.org/10.1016/j.gca.2020.04.035

Chen, Z., Zhou, C., Meyer, M., Xiang, K., Schiffbauer, J., Yuan, X., & Xiao, S. (2013). Trace fossil evidence for Ediacaran bilaterian animals with complex behaviors. *Precambrian Research*, *224*, 690-701. https://doi.org/10.1016/j.precamres.2012.11.004

Chen, Z., Zhou, C., Xiao, S., Wang, W., Guan, C., Hua, H., & Yuan, X. (2014). New Ediacara fossils preserved in marine limestone and their ecological implications. *Scientific Reports*, *4*(1). https://doi.org/10.1038/srep04180

Collins, A., Clark, C., Sajeev, K., Santosh, M., Kelsey, D., & Hand, M. (2007). Passage through India: the Mozambique Ocean suture, high-pressure granulites and the Palghat-Cauvery shear zone system. *Terra Nova*, *19*(2), 141-147. https://doi.org/10.1111/j.1365-3121.2007.00729.x

Collins, A., & Pisarevsky, S. (2005). Amalgamating eastern Gondwana: The evolution of the Circum-Indian Orogens. *Earth-Science Reviews*, *71*(3-4), 229-270. https://doi.org/10.1016/j.earscirev.2005.02.004

Condon, D., Zhu, M., Bowring, S., Wang, W., Yang, A., & Jin, Y. (2005). U-Pb Ages from the Neoproterozoic Doushantuo Formation, China. *Science*, *308*(5718), 95-98. https://doi.org/10.1126/science.1107765

Corsetti, F., & J. Kaufman, A. (2003). Stratigraphic investigations of carbon isotope anomalies and Neoproterozoic ice ages in Death Valley, California. *Geological Society Of America Bulletin*, *115*(8), 916-932. https://doi.org/10.1130/b25066.1

Cox, G., Lewis, C., Collins, A., Halverson, G., Jourdan, F., & Foden, J. et al. (2012). Ediacaran terrane accretion within the Arabian–Nubian Shield. *Gondwana Research*, *21*(2-3), 341-352. https://doi.org/10.1016/j.gr.2011.02.011

Cozzi, A., & Al-Siyabi, H. (2004). Sedimentology and play potential of the late Neoproterozoic Buah Carbonates of Oman. *Geoarabia*, *9*(4), 11-36. https://doi.org/10.2113/geoarabia090411

Cozzi, A., Allen, P., & Grotzinger, J. (2004a). Understanding carbonate ramp dynamics using δ13C profiles: examples from the Neoproterozoic Buah Formation of Oman. *Terra Nova*, *16*(2), 62-67. https://doi.org/10.1111/j.1365-3121.2004.00528.x

Cozzi, A., Grotzinger, J., & Allen, P. (2004b). Evolution of a terminal Neoproterozoic carbonate ramp system (Buah Formation, Sultanate of Oman): Effects of basement paleotopography. *Geological Society Of America Bulletin*, *116*(11-12), 1367-1384. https://doi.org/10.1130/b25387.1

Crockford, P., Mehra, A., & Hoffman, P. (2021). An occurrence of radially-symmetric sedimentary structures in the basal Ediacaran cap dolostone (Keilberg Member) of the Otavi Group. https://doi.org/10.31223/x5kk76

Cui, H., Kaufman, A., Peng, Y., Liu, X., Plummer, R., & Lee, E. (2018). The Neoproterozoic Hüttenberg δ13C anomaly: Genesis and global implications. *Precambrian Research*, *313*, 242-262. https://doi.org/10.1016/j.precamres.2018.05.024

Cui, H., Kaufman, A., Xiao, S., Zhou, C., & Liu, X. (2017). Was the Ediacaran Shuram Excursion a globally synchronized early diagenetic event? Insights from methane-derived authigenic carbonates in the uppermost Doushantuo Formation, South China. *Chemical Geology*, *450*, 59-80. https://doi.org/10.1016/j.chemgeo.2016.12.010

Cui, H., Kitajima, K., Orland, I., Xiao, S., Baele, J., & Kaufman, A. et al. (2021). Deposition or diagenesis? Probing the Ediacaran Shuram excursion in South China by SIMS. *Global And Planetary Change*, *206*, 103591. https://doi.org/10.1016/j.gloplacha.2021.103591

Cui, H., Orland, I., Kitajima, K., Xiao, S., Kaufman, A., & Fournelle, J. et al. (2019). Probing an atypical Shuram Excursion by SIMS. *Geological Society Of America Abstracts With Programs*. https://doi.org/10.1130/abs/2019am-332454

Cui, H., Xiao, S., Zhou, C., Peng, Y., Kaufman, A., & Plummer, R. (2016). Phosphogenesis associated with the Shuram Excursion: Petrographic and geochemical observations from the Ediacaran Doushantuo Formation of South China. *Sedimentary Geology*, *341*, 134-146. https://doi.org/10.1016/j.sedgeo.2016.05.008

De Vleeschouwer, D., & Parnell, A. (2014). Reducing time-scale uncertainty for the Devonian by integrating astrochronology and Bayesian statistics. *Geology*, *42*(6), 491-494. https://doi.org/10.1130/g35618.1

Dececchi, T., Narbonne, G., Greentree, C., & Laflamme, M. (2018). Phylogenetic relationships among the Rangeomorpha: the importance of outgroup selection and implications for their diversification. *Canadian Journal Of Earth Sciences*, *55*(11), 1223-1239. https://doi.org/10.1139/cjes-2018-0022

Derry, L. (2010). A burial diagenesis origin for the Ediacaran Shuram–Wonoka carbon isotope anomaly. *Earth And Planetary Science Letters*, *294*(1-2), 152-162. https://doi.org/10.1016/j.epsl.2010.03.022

Droser, M., Tarhan, L., & Gehling, J. (2017). The Rise of Animals in a Changing Environment: Global Ecological Innovation in the Late Ediacaran. *Annual Review Of Earth And Planetary Sciences*, *45*(1), 593-617. https://doi.org/10.1146/annurev-earth-063016-015645

Eyles, N., & Eyles, C. (1989). Glacially-influenced deep-marine sedimentation of the Late Precambrian Gaskiers Formation, Newfoundland, Canada. *Sedimentology*, *36*(4), 601-620. https://doi.org/10.1111/j.1365-3091.1989.tb02088.x

Fan, H., Fu, X., Ward, J., Yin, R., Wen, H., & Feng, X. (2020). Mercury isotopes track the cause of carbon perturbations in the Ediacaran ocean. *Geology*, *49*(3), 248-252. https://doi.org/10.1130/g48266.1

Fan, H., Nielsen, S., Owens, J., Auro, M., Shu, Y., & Hardisty, D. et al. (2020). Constraining oceanic oxygenation during the Shuram excursion in South China using thallium isotopes. *Geobiology*, *18*(3), 348-365. https://doi.org/10.1111/gbi.12379

Fike, D., Grotzinger, J., Pratt, L., & Summons, R. (2006). Oxidation of the Ediacaran Ocean. *Nature*, *444*(7120), 744-747. https://doi.org/10.1038/nature05345

Forbes, G., Jansen, H., & Schreurs, J. (2010). *Lexicon of Oman subsurface stratigraphy*. Gulf PetroLink.

Gehling, J. G., & Radhakrishna, B. P. (1991). The case for ediacaran fossil roots to the metazoan tree. *Memoir - Geological Society of India, 20*, 181-224.

Gehling, J., Runnegar, B., & Droser, M. (2014). Scratch Traces of Large Ediacara Bilaterian Animals. *Journal Of Paleontology*, *88*(2), 284-298. https://doi.org/10.1666/13-054

Geyer, G., & Landing, E. (2016). The Precambrian–Phanerozoic and Ediacaran–Cambrian boundaries: a historical approach to a dilemma. *Geological Society, London, Special Publications*, *448*(1), 311-349. https://doi.org/10.1144/sp448.10

Glaessner, M. F. (1980). Parvancorina; an arthropod from the late precambrian (ediacarian) of south australia. *Annalen Des Naturhistorischen Museums in Wien, 83*, 83-90.

Gong, Z., Kodama, K., & Li, Y. (2017). Rock magnetic cyclostratigraphy of the Doushantuo Formation, South China and its implications for the duration of the Shuram carbon isotope excursion. *Precambrian Research*, *289*, 62-74. https://doi.org/10.1016/j.precamres.2016.12.002

Gong, Z., & Li, M. (2020). Astrochronology of the Ediacaran Shuram carbon isotope excursion, Oman. *Earth And Planetary Science Letters*, *547*, 116462. https://doi.org/10.1016/j.epsl.2020.116462

Gorin, G., Racz, L., & Walter, M. (1982). Late Precambrian-Cambrian Sediments of Huqf Group, Sultanate of Oman. *AAPG Bulletin*, *66*. https://doi.org/10.1306/03b5ac82-16d1-11d7-8645000102c1865d

Grazhdankin, D. (2014). Patterns of Evolution of the Ediacaran Soft-Bodied Biota. *Journal Of Paleontology*, *88*(2), 269-283. https://doi.org/10.1666/13-072

Grotzinger, J., & Al-Rawahi, Z. (2014). Depositional facies and platform architecture of microbialite-dominated carbonate reservoirs, Ediacaran–Cambrian Ara Group, Sultante of Om. *AAPG Bulletin*, *98*(8), 1453-1494. https://doi.org/10.1306/02271412063

Grotzinger, J. P., Al-Siyabi, H., Al-Hashimi, R., & Cozzi, A. (2002). New model for tectonic evolution of neoproterozoic-cambrian huqf supergroup basins, oman.*GeoArabia (Manama), 7*(2), 241

Grotzinger, J., Bowring, S., Saylor, B., & Kaufman, A. (1995). Biostratigraphic and Geochronologic Constraints on Early Animal Evolution. *Science*, *270*(5236), 598-604. https://doi.org/10.1126/science.270.5236.598

Grotzinger, J., Fike, D., & Fischer, W. (2011). Enigmatic origin of the largest-known carbon isotope excursion in Earth's history. *Nature Geoscience*, 4(5), 285-292. https://doi.org/10.1038/ngeo1138

Halverson, G., Hoffman, P., Schrag, D., Maloof, A., & Rice, A. (2005). Toward a Neoproterozoic composite carbon-isotope record. *Geological Society Of America Bulletin*, *117*(9), 1181. https://doi.org/10.1130/b25630.1

Halverson, G., Porter, S., & Gibson, T. (2018). Dating the late Proterozoic stratigraphic record. *Emerging Topics In Life Sciences*, *2*(2), 137-147. https://doi.org/10.1042/etls20170167

Halverson, G., Shen, C., Davies, J., & Wu, L. (2022). A Bayesian Approach to Inferring Depositional Ages Applied to a Late Tonian Reference Section in Svalbard. *Frontiers In Earth Science*, *10*. https://doi.org/10.3389/feart.2022.798739

Halverson, G., Wade, B., Hurtgen, M., & Barovich, K. (2010). Neoproterozoic chemostratigraphy. *Precambrian Research*, *182*(4), 337-350. https://doi.org/10.1016/j.precamres.2010.04.007

Hansell, D. (2013). Recalcitrant Dissolved Organic Carbon Fractions. *Annual Review Of Marine Science*, *5*(1), 421-445. https://doi.org/10.1146/annurev-marine-120710-100757

Haslett, J., & Parnell, A. (2008). A simple monotone process with application to radiocarbon-dated depth chronologies. *Journal Of The Royal Statistical Society: Series C (Applied Statistics)*, *57*(4), 399-418. https://doi.org/10.1111/j.1467-9876.2008.00623.x

Hinnov, L. (2013). Cyclostratigraphy and its revolutionizing applications in the earth and planetary sciences. *Geological Society Of America Bulletin*, *125*(11-12), 1703-1734. https://doi.org/10.1130/b30934.1

Hoffman, P. (1999). The break-up of Rodinia, birth of Gondwana, true polar wander and the snowball Earth. *Journal Of African Earth Sciences*, *28*(1), 17-33. https://doi.org/10.1016/s0899-5362(99)00018-4

Hoffman, P., Halverson, G., Domack, E., Husson, J., Higgins, J., & Schrag, D. (2007). Are basal Ediacaran (635 Ma) post-glacial "cap dolostones" diachronous?. *Earth And Planetary Science Letters*, *258*(1-2), 114-131. https://doi.org/10.1016/j.epsl.2007.03.032

Hoffman, P., Kaufman, A., Halverson, G., & Schrag, D. (1998). A Neoproterozoic Snowball Earth. *Science*, *281*(5381), 1342-1346. https://doi.org/10.1126/science.281.5381.1342

Hoffman, P., & Li, Z. (2009). A palaeogeographic context for Neoproterozoic glaciation. *Palaeogeography, Palaeoclimatology, Palaeoecology*, *277*(3-4), 158-172. https://doi.org/10.1016/j.palaeo.2009.03.013

Hoyal Cuthill, J., & Conway Morris, S. (2014). Fractal branching organizations of Ediacaran rangeomorph fronds reveal a lost Proterozoic body plan. *Proceedings Of The National Academy Of Sciences*, *111*(36), 13122-13126. https://doi.org/10.1073/pnas.1408542111

Husson, J., Higgins, J., Maloof, A., & Schoene, B. (2015). Ca and Mg isotope constraints on the origin of Earth's deepest δ13C excursion. *Geochimica Et Cosmochimica Acta*, *160*, 243-266. https://doi.org/10.1016/j.gca.2015.03.012

Husson, J., Linzmeier, B., Kitajima, K., Ishida, A., Maloof, A., & Schoene, B. et al. (2020). Large isotopic variability at the micron-scale in 'Shuram' excursion carbonates from South Australia. *Earth And Planetary Science Letters*, *538*, 116211. https://doi.org/10.1016/j.epsl.2020.116211

Husson, J., Maloof, A., & Schoene, B. (2012). A syn-depositional age for Earth's deepest δ13C excursion required by isotope conglomerate tests. *Terra Nova*, *24*(4), 318-325. https://doi.org/10.1111/j.1365-3121.2012.01067.x

Husson, J., Maloof, A., Schoene, B., Chen, C., & Higgins, J. (2015). Stratigraphic expression of Earth's deepest 13C excursion in the Wonoka Formation of South Australia. *American Journal Of Science*, *315*(1), 1-45. https://doi.org/10.2475/01.2015.01

Ivantsov, A. (2013). Trace fossils of precambrian metazoans "Vendobionta" and "Mollusks". *Stratigraphy And Geological Correlation*, *21*(3), 252-264. https://doi.org/10.1134/s0869593813030039

Jiang, L., Planavsky, N., Zhao, M., Liu, W., & Wang, X. (2019). Authigenic origin for a massive negative carbon isotope excursion. *Geology*, *47*(2), 115-118. https://doi.org/10.1130/g45709.1

Johnson, P., Andresen, A., Collins, A., Fowler, A., Fritz, H., & Ghebreab, W. et al. (2011). Late Cryogenian–Ediacaran history of the Arabian–Nubian Shield: A review of depositional, plutonic, structural, and tectonic events in the closing stages of the northern East African Orogen. *Journal Of African Earth Sciences*, *61*(3), 167-232. https://doi.org/10.1016/j.jafrearsci.2011.07.003

Johnson, P., Halverson, G., Kusky, T., Stern, R., & Pease, V. (2013). Volcanosedimentary Basins in the Arabian-Nubian Shield: Markers of Repeated Exhumation and Denudation in a Neoproterozoic Accretionary Orogen. *Geosciences*, *3*(3), 389-445. https://doi.org/10.3390/geosciences3030389

Johnstone, S., Schwartz, T., & Holm-Denoma, C. (2019). A Stratigraphic Approach to Inferring Depositional Ages From Detrital Geochronology Data. *Frontiers In Earth Science*, *7*. https://doi.org/10.3389/feart.2019.00057

Kaufman, A., Corsetti, F., & Varni, M. (2007). The effect of rising atmospheric oxygen on carbon and sulfur isotope anomalies in the Neoproterozoic Johnnie Formation, Death Valley, USA. *Chemical Geology*, *237*(1-2), 47-63. https://doi.org/10.1016/j.chemgeo.2006.06.023

Kaufman, A., & Knoll, A. (1995). Neoproterozoic variations in the C-isotopic composition of seawater: stratigraphic and biogeochemical implications. *Precambrian Research*, *73*(1-4), 27-49. https://doi.org/10.1016/0301-9268(94)00070-8

Kirschvink, J. L. (1992). *Late proterozoic low-latitude global glaciation; the snowball earth* Cambridge Univ. Press.

Knauth, L., & Kennedy, M. (2009). The late Precambrian greening of the Earth. *Nature*, *460*(7256), 728-732. https://doi.org/10.1038/nature08213

Knoll, A., Walter, M., Narbonne, G., & Christie-Blick, N. (2004). A New Period for the Geologic Time Scale. *Science*, *305*(5684), 621-622. https://doi.org/10.1126/science.1098803

Knoll, A., Walter, M., Narbonne, G., & Christie-Blick, N. (2006). The Ediacaran Period: a new addition to the geologic time scale. *Lethaia*, *39*(1), 13-30. https://doi.org/10.1080/00241160500409223

Kruschke, J. (2015). Bayes' Rule. *Doing Bayesian Data Analysis*, 99-120. https://doi.org/10.1016/b978-0-12-405888-0.00005-2

Kump, L., & Arthur, M. (1999). Interpreting carbon-isotope excursions: carbonates and organic matter. *Chemical Geology*, *161*(1-3), 181-198. https://doi.org/10.1016/s0009-2541(99)00086-8

Kusky, T., & Matsah, M. (2003). Neoproterozoic dextral faulting on the Najd Fault System, Saudi Arabia, preceded sinistral faulting and escape tectonics related to closure of the Mozambique Ocean. *Geological Society, London, Special Publications*, *206*(1), 327-361. https://doi.org/10.1144/gsl.sp.2003.206.01.16

Laflamme, M., Darroch, S., Tweedt, S., Peterson, K., & Erwin, D. (2013). The end of the Ediacara biota: Extinction, biotic replacement, or Cheshire Cat?. *Gondwana Research*, *23*(2), 558-573. https://doi.org/10.1016/j.gr.2012.11.004

Lang, X., Shen, B., Peng, Y., Huang, K., Lv, J., & Ma, H. (2016). Ocean oxidation during the deposition of basal Ediacaran Doushantuo cap carbonates in the Yangtze Platform, South China. *Precambrian Research*, *281*, 253-268. https://doi.org/10.1016/j.precamres.2016.06.006

Le Guerroué, E., Allen, P., & Cozzi, A. (2006a). Chemostratigraphic and sedimentological framework of the largest negative carbon isotopic excursion in Earth history: The Neoproterozoic Shuram Formation (Nafun Group, Oman). *Precambrian Research*, *146*(1-2), 68-92. https://doi.org/10.1016/j.precamres.2006.01.007

Le Guerroué, E., Allen, P., Cozzi, A., Etienne, J., & Fanning, M. (2006b). 50 Myr recovery from the largest negativeδ13C excursion in the Ediacaran ocean. *Terra Nova*, *18*(2), 147-153. https://doi.org/10.1111/j.1365-3121.2006.00674.x

Leather, J. (2001) Sedimentology, chemostratigraphy and geo- chronology of the lower Huqf Supergroup, Oman, Vols. 1 and 2. PhD Thesis, Trinity College Dublin.

Lee, C., Fike, D., Love, G., Sessions, A., Grotzinger, J., Summons, R., & Fischer, W. (2013). Carbon isotopes and lipid biomarkers from organic-rich facies of the Shuram Formation, Sultanate of Oman. *Geobiology*, *11*(5), 406-419. https://doi.org/10.1111/gbi.12045

Lee, C., Love, G., Fischer, W., Grotzinger, J., & Halverson, G. (2015). Marine organic matter cycling during the Ediacaran Shuram excursion. *Geology*, G37236.1. https://doi.org/10.1130/g37236.1

Lein, A. (2004). Authigenic Carbonate Formation in the Ocean. *Lithology And Mineral Resources*, *39*(1), 1-30. https://doi.org/10.1023/b:limi.0000010767.52720.8f

Li, Z., Cao, M., Loyd, S., Algeo, T., Zhao, H., & Wang, X. et al. (2020). Transient and stepwise ocean oxygenation during the late Ediacaran Shuram Excursion: Insights from carbonate δ238U of northwestern Mexico. *Precambrian Research*, *344*, 105741. https://doi.org/10.1016/j.precamres.2020.105741

Lin, J., Gon, S., Gehling, J., Babcock, L., Zhao, Y., & Zhang, X. et al. (2006). AParvancorina-like arthropod from the Cambrian of South China. *Historical Biology*, *18*(1), 33-45. https://doi.org/10.1080/08912960500508689

Linnemann, U., Ovtcharova, M., Schaltegger, U., Gärtner, A., Hautmann, M., & Geyer, G. et al. (2019). New high-resolution age data from the Ediacaran-Cambrian boundary indicate rapid, ecologically driven onset of the Cambrian explosion. *Terra Nova*, *31*(1), 49-58. https://doi.org/10.1111/ter.12368

Liu, Y., Chen, W., Foley, S., Shen, Y., Chen, C., & Li, J. et al. (2021). The largest negative carbon isotope excursions in Neoproterozoic carbonates caused by recycled carbonatite volcanic ash. *Science Bulletin*, *66*(18), 1925-1931. https://doi.org/10.1016/j.scib.2021.04.021

Loosveld, R., Bell, A., & Terken, J. (1996). The Tectonic Evolution of Interior Oman. *Geoarabia*, *1*(1), 28-51. https://doi.org/10.2113/geoarabia010128

Lyons, T., Reinhard, C., & Planavsky, N. (2014). The rise of oxygen in Earth's early ocean and atmosphere. *Nature*, *506*(7488), 307-315. https://doi.org/10.1038/nature13068

Macdonald, F., Strauss, J., Sperling, E., Halverson, G., Narbonne, G., & Johnston, D. et al. (2013). The stratigraphic relationship between the Shuram carbon isotope excursion, the oxygenation of Neoproterozoic oceans, and the first appearance of the Ediacara biota and bilaterian trace fossils in northwestern Canada. *Chemical Geology*, *362*, 250-272. https://doi.org/10.1016/j.chemgeo.2013.05.032

Matthews, J., Liu, A., Yang, C., McIlroy, D., Levell, B., & Condon, D. (2021). A Chronostratigraphic Framework for the Rise of the Ediacaran Macrobiota: New Constraints from Mistaken Point Ecological Reserve, Newfoundland. *GSA Bulletin*, *133*(3-4), 612-624. https://doi.org/10.1130/b35646.1

McFadden, K., Huang, J., Chu, X., Jiang, G., Kaufman, A., & Zhou, C. et al. (2008). Pulsed oxidation and biological evolution in the Ediacaran Doushantuo Formation. *Proceedings Of The National Academy Of Sciences*, *105*(9), 3197-3202. https://doi.org/10.1073/pnas.0708336105

McKenzie, D. (1978). Some remarks on the development of sedimentary basins. *Earth And Planetary Science Letters*, *40*(1), 25-32. https://doi.org/10.1016/0012-821x(78)90071-7

Meert, J., Levashova, N., Bazhenov, M., & Landing, E. (2016). Rapid changes of magnetic Field polarity in the late Ediacaran: Linking the Cambrian evolutionary radiation and increased UV-B radiation. *Gondwana Research*, *34*, 149-157. https://doi.org/10.1016/j.gr.2016.01.001

Meert, J., & Lieberman, B. (2008). The Neoproterozoic assembly of Gondwana and its relationship to the Ediacaran–Cambrian radiation. *Gondwana Research*, *14*(1-2), 5-21. https://doi.org/10.1016/j.gr.2007.06.007

Melezhik, V., Fallick, A., & Pokrovsky, B. (2005). Enigmatic nature of thick sedimentary carbonates depleted in C beyond the canonical mantle value: The challenges to our understanding of the terrestrial carbon cycle. *Precambrian Research*, *137*(3-4), 131-165. https://doi.org/10.1016/j.precamres.2005.03.010

Melezhik, V., Pokrovsky, B., Fallick, A., Kuznetsov, A., & Bujakaite, M. (2009). Constraints on 87Sr/86Sr of Late Ediacaran seawater: insight from Siberian high-Sr limestones. *Journal Of The Geological Society*, *166*(1), 183-191. https://doi.org/10.1144/0016-76492007-171

Minguez, D., & Kodama, K. (2017). Rock magnetic chronostratigraphy of the Shuram carbon isotope excursion: Wonoka Formation, Australia. *Geology*, *45*(6), 567-570. https://doi.org/10.1130/g38572.1

Minguez, D., Kodama, K., & Hillhouse, J. (2015). Paleomagnetic and cyclostratigraphic constraints on the synchroneity and duration of the Shuram carbon isotope excursion, Johnnie Formation, Death Valley Region, CA. *Precambrian Research*, *266*, 395-408. https://doi.org/10.1016/j.precamres.2015.05.033

Miyazaki, Y., Planavsky, N., Bolton, E., & Reinhard, C. (2018). Making Sense of Massive Carbon Isotope Excursions With an Inverse Carbon Cycle Model. *Journal Of Geophysical Research: Biogeosciences*, *123*(8), 2485-2496. https://doi.org/10.1029/2018jg004416

Myrow, P., & Kaufman, A. (1999). A newly discovered cap carbonate above Varanger-age glacial deposits in Newfoundland, Canada. *Journal Of Sedimentary Research*, *69*(3), 784-793. https://doi.org/10.2110/jsr.69.784

Narbonne, G. (2005). THE EDIACARA BIOTA: Neoproterozoic Origin of Animals and Their Ecosystems. *Annual Review Of Earth And Planetary Sciences*, *33*(1), 421-442. https://doi.org/10.1146/annurev.earth.33.092203.122519

Narbonne, G., Laflamme, M., Trusler, P., Dalrymple, R., & Greentree, C. (2014). Deep-Water Ediacaran Fossils from Northwestern Canada: Taphonomy, Ecology, and Evolution. *Journal Of Paleontology*, *88*(2), 207-223. https://doi.org/10.1666/13-053

Nettle, D., Halverson, G., Cox, G., Collins, A., Schmitz, M., & Gehling, J. et al. (2013). A middle-late Ediacaran volcano-sedimentary record from the eastern Arabian-Nubian shield. *Terra Nova*, *26*(2), 120-129. https://doi.org/10.1111/ter.12077

Normore, L. S. (2011). Preliminary findings on the geology of the trinity map area (NTS 2C/06), newfoundland. *Current Research (Newfoundland and Labrador.Geological Survey)*, 273-293.

Osburn, M., Grotzinger, J., & Bergmann, K. (2014). Facies, stratigraphy, and evolution of a middle Ediacaran carbonate ramp: Khufai Formation, Sultanate of Oman. *AAPG Bulletin*, *98*(8), 1631-1667. https://doi.org/10.1306/07291312140

Papineau, D. (2010). Global Biogeochemical Changes at Both Ends of the Proterozoic: Insights from Phosphorites. *Astrobiology*, *10*(2), 165-181. https://doi.org/10.1089/ast.2009.0360

Parnell, A., Buck, C., & Doan, T. (2011). A review of statistical chronology models for high-resolution, proxy-based Holocene palaeoenvironmental reconstruction. *Quaternary Science Reviews*, *30*(21-22), 2948-2960. https://doi.org/10.1016/j.quascirev.2011.07.024

Parnell, A., Haslett, J., Allen, J., Buck, C., & Huntley, B. (2008). A flexible approach to assessing synchroneity of past events using Bayesian reconstructions of sedimentation history. *Quaternary Science Reviews*, *27*(19-20), 1872-1885. https://doi.org/10.1016/j.quascirev.2008.07.009

Paulsen, T., Deering, C., Sliwinski, J., Bachmann, O., & Guillong, M. (2017). Evidence for a spike in mantle carbon outgassing during the Ediacaran period. *Nature Geoscience*, *10*(12), 930-934. https://doi.org/10.1038/s41561-017-0011-6

Planavsky, N., Reinhard, C., Wang, X., Thomson, D., McGoldrick, P., & Rainbird, R. et al. (2014). Low Mid-Proterozoic atmospheric oxygen levels and the delayed rise of animals. *Science*, *346*(6209), 635-638. https://doi.org/10.1126/science.1258410

Prave, A., Condon, D., Hoffmann, K., Tapster, S., & Fallick, A. (2016). Duration and nature of the end-Cryogenian (Marinoan) glaciation. *Geology*, *44*(8), 631-634. https://doi.org/10.1130/g38089.1

Pu, J., Bowring, S., Ramezani, J., Myrow, P., Raub, T., & Landing, E. et al. (2016). Dodging snowballs: Geochronology of the Gaskiers glaciation and the first appearance of the Ediacaran biota. *Geology*, *44*(11), 955-958. https://doi.org/10.1130/g38284.1

Rieu, R., Allen, P., Etienne, J., Cozzi, A., & Wiechert, U. (2006). A Neoproterozoic glacially influenced basin margin succession and 'atypical' cap carbonate associated with bedrock palaeovalleys, Mirbat area, southern Oman. *Basin Research*, *18*(4), 471-496. https://doi.org/10.1111/j.1365-2117.2006.00304.x

Rieu, R., Allen, P., Cozzi, A., Kosler, J., & Bussy, F. (2007). A composite stratigraphy for the Neoproterozoic Huqf Supergroup of Oman: integrating new litho-, chemo- and chronostratigraphic data of the Mirbat area, southern Oman. *Journal Of The Geological Society*, *164*(5), 997-1009. https://doi.org/10.1144/0016-76492006-114

Robinson, F., Bonin, B., Pease, V., & Anderson, J. (2017). A discussion on the tectonic implications of Ediacaran late- to post-orogenic A-type granite in the northeastern Arabian Shield, Saudi Arabia. *Tectonics*, *36*(3), 582-600. https://doi.org/10.1002/2016tc004320

Robinson, F., Foden, J., Collins, A., & Payne, J. (2014). Arabian Shield magmatic cycles and their relationship with Gondwana assembly: Insights from zircon U–Pb and Hf isotopes. *Earth And Planetary Science Letters*, *408*, 207-225. https://doi.org/10.1016/j.epsl.2014.10.010

Rooney, A., Cantine, M., Bergmann, K., Gómez-Pérez, I., Al Baloushi, B., & Boag, T. et al. (2020). Calibrating the coevolution of Ediacaran life and environment. *Proceedings Of The National Academy Of Sciences*, *117*(29), 16824-16830. https://doi.org/10.1073/pnas.2002918117

Rooney, A., Strauss, J., Brandon, A., & Macdonald, F. (2015). A Cryogenian chronology: Two long-lasting synchronous Neoproterozoic glaciations. *Geology*, *43*(5), 459-462. https://doi.org/10.1130/g36511.1

Rose, C., & Maloof, A. (2010). Testing models for post-glacial 'cap dolostone' deposition: Nuccaleena Formation, South Australia. *Earth And Planetary Science Letters*, *296*(3-4), 165-180. https://doi.org/10.1016/j.epsl.2010.03.031

Rothman, D., Hayes, J., & Summons, R. (2003). Dynamics of the Neoproterozoic carbon cycle. *Proceedings Of The National Academy Of Sciences*, *100*(14), 8124-8129. https://doi.org/10.1073/pnas.0832439100

Sato, H., Tahata, M., Sawaki, Y., Maruyama, S., Yoshida, N., & Shu, D. et al. (2016). A high-resolution chemostratigraphy of post-Marinoan Cap Carbonate using drill core samples in the Three Gorges area, South China. *Geoscience Frontiers*, *7*(4), 663-671. https://doi.org/10.1016/j.gsf.2015.07.008

Schoene, B., Eddy, M., Samperton, K., Keller, C., Keller, G., Adatte, T., & Khadri, S. (2019). U-Pb constraints on pulsed eruption of the Deccan Traps across the end-Cretaceous mass extinction. *Science*, *363*(6429), 862-866. https://doi.org/10.1126/science.aau2422

Schrag, D., Higgins, J., Macdonald, F., & Johnston, D. (2013). Authigenic Carbonate and the History of the Global Carbon Cycle. *Science*, *339*(6119), 540-543. https://doi.org/10.1126/science.1229578

Schröder, S., & Grotzinger, J. (2007). Evidence for anoxia at the Ediacaran–Cambrian boundary: the record of redox-sensitive trace elements and rare earth elements in Oman. *Journal Of The Geological Society*, *164*(1), 175-187. https://doi.org/10.1144/0016-76492005-022

Schröder, S., Schreiber, B., Amthor, J., & Matter, A. (2003). A depositional model for the terminal Neoproterozoic-Early Cambrian Ara Group evaporites in south Oman. *Sedimentology*, *50*(5), 879-898. https://doi.org/10.1046/j.1365-3091.2003.00587.x

Sclater, J., & Christie, P. (1980). Continental stretching: An explanation of the Post-Mid-Cretaceous subsidence of the central North Sea Basin. *Journal Of Geophysical Research: Solid Earth*, *85*(B7), 3711-3739. https://doi.org/10.1029/jb085ib07p03711

Seilacher, A. (1992). Vendobionta and Psammocorallia: lost constructions of Precambrian evolution. *Journal Of The Geological Society*, *149*(4), 607-613. https://doi.org/10.1144/gsjgs.149.4.0607

Shen, C., Schmitz, M., Johnson, P., Davies, J., & Halverson, G. (in press). U-Pb geochronology and cyclostratigraphy of the middle Ediacaran upper Jibalah Group, eastern Arabian Shield. *Precambrian Research*.

Shi, W., Li, C., & Algeo, T. (2017). Quantitative model evaluation of organic carbon oxidation hypotheses for the Ediacaran Shuram carbon isotopic excursion. *Science China Earth Sciences*, *60*(12), 2118-2127. https://doi.org/10.1007/s11430-017-9137-1

Shi, W., Li, C., Luo, G., Huang, J., Algeo, T., & Jin, C. et al. (2018). Sulfur isotope evidence for transient marine-shelf oxidation during the Ediacaran Shuram Excursion. *Geology*, *46*(3), 267-270. https://doi.org/10.1130/g39663.1

Sperling, E., Wolock, C., Morgan, A., Gill, B., Kunzmann, M., & Halverson, G. et al. (2015). Statistical analysis of iron geochemical data suggests limited late Proterozoic oxygenation. *Nature*, *523*(7561), 451-454. https://doi.org/10.1038/nature14589

Squire, R., Campbell, I., Allen, C., & Wilson, C. (2006). Did the Transgondwanan Supermountain trigger the explosive radiation of animals on Earth?. *Earth And Planetary Science Letters*, *250*(1-2), 116-133. https://doi.org/10.1016/j.epsl.2006.07.032

Stern, R. (1994). Arc assembly and continental collision in the Neoproterozoic east African orogen: Implications for the Consolidation of Gondwanaland. *Annual Review Of Earth*

And Planetary Sciences, *22*(1), 319-351. https://doi.org/10.1146/annurev.ea.22.050194.001535

Stern, R., & Johnson, P. (2010). Continental lithosphere of the Arabian Plate: A geologic, petrologic, and geophysical synthesis. *Earth-Science Reviews*, *101*(1-2), 29-67. https://doi.org/10.1016/j.earscirev.2010.01.002

Sun, X., & Turchyn, A. (2014). Significant contribution of authigenic carbonate to marine carbon burial. *Nature Geoscience*, *7*(3), 201-204. https://doi.org/10.1038/ngeo2070

Swanson-Hysell, N., Rose, C., Calmet, C., Halverson, G., Hurtgen, M., & Maloof, A. (2010). Cryogenian Glaciation and the Onset of Carbon-Isotope Decoupling. *Science*, *328*(5978), 608-611. https://doi.org/10.1126/science.1184508

Terken, J., Frewin, N., & Indrelid, S. (2001). Petroleum systems of Oman: Charge timing and risks. *AAPG Bulletin*, *85*. https://doi.org/10.1306/8626d081-173b-11d7-8645000102c1865d

Tohver, E., D'Agrella-Filho, M., & Trindade, R. (2006). Paleomagnetic record of Africa and South America for the 1200–500Ma interval, and evaluation of Rodinia and Gondwana assemblies. *Precambrian Research*, *147*(3-4), 193-222. https://doi.org/10.1016/j.precamres.2006.01.015

Trayler, R., Schmitz, M., Cuitiño, J., Kohn, M., Bargo, M., & Kay, R. et al. (2019). An improved approach to age-modeling in deep time: Implications for the Santa Cruz Formation, Argentina. *GSA Bulletin*, *132*(1-2), 233-244. https://doi.org/10.1130/b35203.1

Waggoner, B. (2003). The Ediacaran Biotas in Space and Time. *Integrative And Comparative Biology*, *43*(1), 104-113. https://doi.org/10.1093/icb/43.1.104

Witkosky, R., & Wernicke, B. (2018). Subsidence history of the Ediacaran Johnnie Formation and related strata of southwest Laurentia: Implications for the age and duration of the Shuram isotopic excursion and animal evolution. *Geosphere*, *14*(5), 2245-2276. https://doi.org/10.1130/ges01678.1

Xiao, S., Bao, H., Wang, H., Kaufman, A., Zhou, C., & Li, G. et al. (2004). The Neoproterozoic Quruqtagh Group in eastern Chinese Tianshan: evidence for a post-Marinoan glaciation. *Precambrian Research*, *130*(1-4), 1-26. https://doi.org/10.1016/j.precamres.2003.10.013

Xiao, S., & Laflamme, M. (2009). On the eve of animal radiation: phylogeny, ecology and evolution of the Ediacara biota. *Trends In Ecology & Evolution*, *24*(1), 31-40. https://doi.org/10.1016/j.tree.2008.07.015

Xiao, S., & Narbonne, G. (2020). The Ediacaran Period. *Geologic Time Scale 2020*, 521-561. https://doi.org/10.1016/b978-0-12-824360-2.00018-8

Xu, D., Wang, X., Shi, X., Peng, Y., & Stüeken, E. (2021). Feedback Between Carbon and Nitrogen Cycles During the Ediacaran Shuram Excursion. *Frontiers In Earth Science*, *9*. https://doi.org/10.3389/feart.2021.678149

Yang, C., Rooney, A., Condon, D., Li, X., Grazhdankin, D., & Bowyer, F. et al. (2021). The tempo of Ediacaran evolution. *Science Advances*, *7*(45). https://doi.org/10.1126/sciadv.abi9643

Zhou, C., Huyskens, M., Lang, X., Xiao, S., & Yin, Q. (2019). Calibrating the terminations of Cryogenian global glaciations. *Geology*, *47*(3), 251-254. https://doi.org/10.1130/g45719.1

Zhou, C., Xiao, S., Wang, W., Guan, C., Ouyang, Q., & Chen, Z. (2017). The stratigraphic complexity of the middle Ediacaran carbon isotopic record in the Yangtze Gorges area, South China, and its implications for the age and chemostratigraphic significance of the Shuram excursion. *Precambrian Research*, *288*, 23-38. https://doi.org/10.1016/j.precamres.2016.11.007

Zhou, M., Luo, T., Huff, W., Yang, Z., Zhou, G., & Gan, T. et al. (2018). Timing the termination of the Doushantuo negative carbon isotope excursion: evidence from U-Pb ages from the Dengying and Liuchapo formations, South China. *Science Bulletin*, *63*(21), 1431-1438. https://doi.org/10.1016/j.scib.2018.10.002

Zhu, M., Babcock, L., & Peng, S. (2006). Advances in Cambrian stratigraphy and paleontology: Integrating correlation techniques, paleobiology, taphonomy and paleoenvironmental reconstruction. *Palaeoworld*, *15*(3-4), 217-222. https://doi.org/10.1016/j.palwor.2006.10.016

Zhu, Z., Campbell, I., Allen, C., Brocks, J., & Chen, B. (2022). The temporal distribution of Earth's supermountains and their potential link to the rise of atmospheric oxygen and biological evolution. *Earth And Planetary Science Letters*, *580*, 117391. https://doi.org/10.1016/j.epsl.2022.117391

APPENDICES

R Code:

The programming code used for updating age-depths, generating a Bayesian age model, conducting a subsidence analysis, and generating a Bayesian thermal subsidence model can be found at https://github.com/WillWong328/oman_age_subsidence_model/

Correlated Ages:

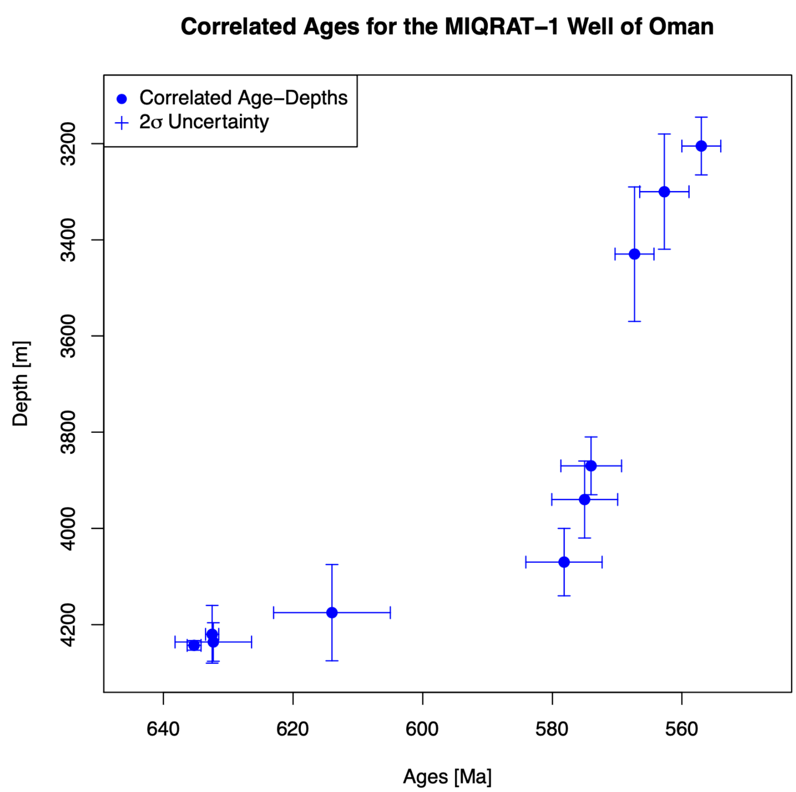

Appendix 1 | Correlated Ages for the MIQRAT-1 Well: The correlated ages of the Nafun Group stratigraphy of the MIQRAT-1 well prior to being updated based on the law of superposition.

Subsidence Analysis:

Stratigraphic Unit:	Surface Porosity:	Exponential Decay Coefficient (km^{-1}):	Sediment Grain Density ($kg\ m^{-3}$):
Buah Dolostones	0.20	0.60	2870
Buah Limestones	0.40	0.60	2710
Shuram Limestones	0.40	0.60	2710
Shuram Interbedded-Limestones	0.40	0.60	2715
Shuram Interbedded-Shales	0.63	0.51	2715
Shuram Shales	0.63	0.51	2720
Khufai Dolostones	0.20	0.60	2870
Khufai Shales	0.63	0.51	2720
Khufai Dolostones	0.20	0.60	2870
Khufai Limestones	0.40	0.60	2710
Khufai Dolostones	0.20	0.60	2870
Khufai Shales	0.63	0.51	2720
Khufai Dolostones	0.20	0.60	2870
Masirah Bay Shales	0.63	0.51	2720
Hadash Dolostones	0.20	0.60	2870

Appendix 2 | Subsidence Analysis Parameter Values: The parameter values used in the decompaction and backstripping procedures.

Age (Ma)	Backstripped Tectonic Subsidence (m)	Total Sediment Loaded Subsidence (m)
635.55	0	0
634.75	22.16	6.14
601.77	215.41	255.17
593.60	220.60	278.69
588.75	239.84	307.53
581.77	236.45	338.83
574.46	315.92	535.23
572.77	317.14	566.89
572.15	334.07	600.36
571.18	339.96	659.7
569.74	522.77	911.93
568.83	597.85	1057.16
568.17	612.77	1120.89
567.25	632.28	1181.19
566.71	635.14	1205.21
556.03	640.78	1394.79

Appendix 3 | Backstripped and Total Subsidence of the Oman Basin: The water-loaded and sediment-loaded subsidence based on the lithology and model boundary ages of the Nafun Group of the MIQRAT-1 well of Oman.